Modeling of Shell Forming by Line Heating

by

Guoxin Yu

B.S. in Naval Architecture (1990)
M.S. in Structural Mechanics (1993)
Shanghai Jiao Tong University, China

M.S. in Naval Architecture and Marine Engineering (1999)
M.S. in Electrical Engineering and Computer Science (1999)
Massachusetts Institute of Technology

Submitted to the Department of Ocean Engineering
in partial fulfillment of the requirements for the degree of

Doctor of Philosophy

at the

MASSACHUSETTS INSTITUTE OF TECHNOLOGY

June 2000

Author .....
Department of Ocean Engineering
April 5, 2000

Certified by .....
Nicholas M. Patrikalakis, Kawasaki Professor of Engineering
Department of Ocean Engineering
Thesis Supervisor

Accepted by .....
Nicholas M. Patrikalakis, Kawasaki Professor of Engineering
Chairman, Committee on Graduate Studies
Department of Ocean Engineering

Modeling of Shell Forming by Line Heating

by

Guoxin Yu

Submitted to the Department of Ocean Engineering
on April 5, 2000, in partial fulfillment of the
requirements for the degree of
Doctor of Philosophy

Abstract

Metal forming by a moving heat source is an efficient and economical method for forming flat metal plates into doubly curved shapes. This thesis proposes an FEM model for three dimensional thermo-mechanical simulation of the process of shell forming by line heating. Since the heat flux is focused on a small area under the heat source, a rezoning technique is developed to reduce computation time in three-dimensional numerical simulation. This involves dynamic remeshing of the metal plate so that the area directly under the heat source is densely meshed while other areas are sparsely meshed. A simplified model is also developed which is based on semi-analytical thermal analysis and idealization of plastic zone during line heating. This simplified model is useful in real-time control of the forming process since the computation time can be greatly reduced. The two thermo-mechanical models lead to a better understanding of the line heating mechanism and more accurate and efficient prediction of the deformation of metal plates. Based on these two models, parametric studies of the edge effects, heat input, heat source velocity, spot size, heat loss coefficients, etc. are performed, and nondimensional parameters which control the bending angle are derived. Finally, an algorithm for surface development for heating path planning is developed. This algorithm minimizes the strains from the doubly curved surface to its planar development. Compared with conventional surface development methods, this algorithm takes into account the characteristics of the process of forming by line heating. This surface development algorithm lays the basis for heating path determination. Based on the developed algorithms and models, we will be able to not only determine the heating paths, but also determine the heating conditions which are necessary to form an initial flat plate into a doubly curved plate. These are critical for automation of the metal forming process.

Thesis Supervisor: Nicholas M. Patrikalakis, Ph.D.
Title: Kawasaki Professor of Engineering

Acknowledgments

I would like to thank my thesis supervisor, Professor Nicholas M. Patrikalakis for his expert advice on my research work and instructive guidance on my academic study. Thank Professor Koichi Masubuchi for introducing me this research topic through the DARPA project "Laser Forming for Flexible Fabrication". I would like to thank Professors Thomas W. Eagar, Jaime Peraire, Tomasz Wierzbicki and Dr. Takashi Maekawa for serving as my thesis committee and their valuable comments.

Thanks also go to Mr. Fred Baker, for providing a stable hardware environment for my thesis work, former Design Laboratory fellow Roger J. Anderson for the experimental data from line heating using a torch, the research group lead by Dr. Richard Martukanitz at Pennsylvania State University Applied Research Laboratory for sharing the results of their experiments on laser line heating, and Design Laboratory fellows Dr. Todd R. Jackson, Dr. Guoling Shen for useful discussions.

Finally, I thank my family for their love, understanding, and support during my study at MIT.

Funding for this research was obtained in part from a DARPA grant in a subcontract from Rocketdyne Division of Boeing North American, Inc. (AF contract No. F33615-95-C-5542), the New Industry Research Organization (NIRO) and the Toshiba Corporation, Japan.

Contents

List of Figures

List of Tables

Chapter 1

Introduction

1.1 Overview of metal forming

Metal forming is a process routinely performed in mechanical engineering, naval architecture, aeronautical and astronautical engineering. Forming takes place in a metal whenever it is subjected to stresses greater than the yield stress so that the deformation moves from the elastic to the plastic range. All methods of metal forming are based on a combination of plastic and elastic deformation.

According to the temperature conditions under which they are carried on, forming processes are generally classified as cold or hot forming. Cold forming is usually performed at room temperature, while hot forming is performed at an elevated temperature. Since at increasing temperature, yield strength and rate of strain hardening will usually progressively decline and that ductility will increase, less energy input will be required to hot-form the plate. On the contrary, a cold-formed material will exhibit high strength and will require more energy input. Whichever method is used, any metal-forming process will impose residual stresses in the metal because of the nonuniform plastic deformation introduced during the forming process. In shipbuilding industry, these residual stresses cause the distortion problems in operations subsequent to the forming of the hull plates. A typical example is the distortion of a pre-formed hull plate when longitudinal and transverse stiffeners are welded to it. Like hot-forming, the heat input during welding process causes distortion in the hull

plate. In addition, during welding, some of the built-in residual stresses, which were created during the forming process, are released and the plate deforms.

According to the mechanisms used to bend the plates, methods for forming steel plates into curved shells are classified as mechanical forming and thermo-mechanical forming. In either of the two mechanisms, steel plates are formed into the desired shape by producing plastic deformations in appropriate amounts and distributions. In mechanical forming of a steel plate [27, 25], these plastic deformations are produced by mechanically pressing the plate to a die of proper shape, or by feeding the plate through a set of rollers (cold rolling) to produce the desired shape. Mechanical forming by using a die is best suited to high production quantities, allowing the development and tooling costs to be amortized over several hundreds or thousands of parts. A good example of such an application is the forming of automobile bodies from thin metal sheets. In the shipbuilding industry, small production lots are the standard, and plates are thicker compared with those found in the automobile industry. Therefore, mechanical forming with a die is not suited for forming ship hull plates. Instead, a set of wide rollers are frequently used to form singly curved plates, and a set of narrow rollers are used to form doubly curved plates [61]. One of the disadvantages of this cold-rolling is that significant residual stresses are embedded in the metal, which result in distortions during assembly by welding. The other disadvantage is that due to edge effects and the constraints of the locations of the rolls, it is impossible to form regions within about 5 cm of the plate edge.

When a plate is being thermo-mechanically formed, plastic deformation is produced by the thermal stresses generated during the heating and subsequent cooling of the plate. During this process, one side of the plate is heated while the other side is kept cooler. The temperature gradient in the material across the thickness causes the metal to bend in one direction. In the mean time, the expanded metal is constrained by the surrounding cooler metal, and compressive stresses result. When the heat is removed, the plate cools and the metal contracts. The plate will then deform and assume an equilibrium state in the direction reverse to that when it was heated. The curvature generated is a function of temperature gradient between the top and

bottom surfaces of the plate. An ideal thermomechanical forming system would be able to heat a steel plate with desired temperature gradient at any point. First, this system involves a very large heating pad and should be able to heat the whole plate at one time. Second, the heat flux distribution should be adjustable according to the desired temperature gradients. This system is presently prohibited by economic and processing constraints.

The line-heating process is currently being used in a large number of shipyards to form hull plates [15, 19]. Three types of heat sources can be used in the line heating process: an oxyacetylene torch or a set of torches, induction heating and laser. Compared with mechanical pressing, thermo-mechanical forming using an oxyacetylene torch, is more versatile and less expensive. Steel plates can also be formed with complex double curvatures, and the resulting residual stresses are minimal. However, line heating with an oxyacetylene torch has some inherent drawbacks. Forming by line heating is an art which requires many years of experience because complex mechanisms are involved. In order to form a plate into an exact desired shape, one must know how the plate should be heated. One must also have a means to control the heating and cooling processes. Many years of on-the-job training are often necessary for one to master this skill through experience. Compared with torch heating, induction heating is easier to control, and is used in some Japanese shipyards. However, the equipment is heavier and the heated area is larger, so induction heating is usually not performed manually. Instead, a robotic system is needed to control the heating process. Induction heating is intended for heating large plates.

Laser forming is a thermo-mechanical method which uses a laser instead of an oxyacetylene torch as the heat source [49]. The basic metal forming mechanisms for laser forming are essentially the same as the forming technique using an oxyacetylene torch. Compared with the heat source of an oxy-acetylene torch, a laser has the following advantages: (1) The power and its distribution are easier to control and reproduce. (2) The heated region is smaller so that material degradation (degradation of material properties due to line heating) is minimized. (3) A laser system can be integrated with a robotic system for automation of the line heating process.

1.2 Related research

Forming by flame or laser line heating has been an active research topic in manufacturing, especially in shipbuilding [15, 44, 43]. Professor Masubuchi was the principal investigator of the first serious effort on laser forming starting in 1980s during research programs at MIT sponsored by the Japan Welding Engineering Society [32] and the US Navy [34, 35, 31]. In these programs, systematic experimental research was carried out to study the relations between bending angles and the heat power, heat source speed, the size of the plate, and the number of heating passes. Both mild steel and high strength steel plates were used as specimens. Edge effects were discovered and an important parameter principally controlling angular distortion was identified. Theoretical research on the mechanism of the line heating process [38, 40, 51, 39, 22, 24, 26] aimed to predict the final shape of the metal plate when given the heating conditions and mechanical properties of the metal plate to be heated. Finite element method (FEM) or simplified beam or plate theory was usually applied. Research on design of the proper heating and/or cooling processes [58, 59, 60, 57, 21] was based on the experience of forming simple shape surfaces from rectangular plates. Strain or curvature analysis was employed to determine heating lines. No general process planning scheme for general curved shapes nor automatic control of the forming process is available. Therefore, current state-of-the-art heat forming procedures are far from automatic.

1.2.1 Line heating mechanism

The problem of laser or flame forming of metal plates can be divided into two subproblems: the heat transfer problem and the elasto-plastic deformation problem, where the solution of the first problem is a prerequisite of the second problem. The heat transfer problem of a moving heat source has been widely studied in the welding community. Rosenthal [47] first derived the analytic solution of temperature field for point and line heat sources utilizing the heat conduction equation for the quasi-stationary state. Since then, to reduce the errors, a number of modifications have

been introduced such as a distributed heat source [55] and a change of phase [29]. Eagar and Tsai [14] derived a transient model of the temperature field in a semi-infinite body bounded by a plane subjected to a traveling Gaussian distributed heat source on this bounding plane. Boo and Cho [6] derived an analytical model of the arc welding process that describes the three-dimensional temperature field more accurately in a finite thickness plate subjected to a Gaussian distributed traveling heat source. More recently, Jeong and Cho [23] transformed the solution of the temperature field in a finite thickness plate to that for a fillet-welded joint using the conformal mapping technique. Nguyen et al. [41] studied the analytical solution for transient temperature of a semi-infinite body subjected to a 3D moving heat source instead of a surface flux. The heat source has a double-ellipsoidal power density, i.e., elliptical distribution on top surface, as well as elliptical distribution across a small portion of the thickness. This formulation of the heat source distribution allows to model the penetration during the welding process. For the process of metal forming by line heating, more papers on numerical simulation are available than those on analytical prediction. Moshaiov and Latorre [38] investigated the time-varying temperature field in the plate during flame bending process. They solved the problem by using the ADINA-T finite-element program in the transient analysis mode. Their results show that the temperature field has a transient behavior near plate edges while far away from edges, the temperature field is quasi-steady. That is, the temperature field is almost static when viewed from a coordinate system moving with the flame. Based on ideal material properties and temperature field assumptions which capture the characteristics of the temperature distribution obtained by Moshaiov and Latorre [38], Shin and Moshaiov [51] [39] developed a simplified strip model for line heating analysis. Moshaiov and Vorus [40] used boundary element method to analyze the plate bending process, but their numerical results did not compare well with experiments. More recently, Jang et al. [22] have proposed another simplified model which uses springs to represent the interaction between the central plastic area and the surrounding elastic areas. Its effectiveness in predicting the distortion of metal plates of various materials needs to be further verified. Kyrsanidi et al.[26] performed FEM

simulation of the laser forming process using a static mesh, and the numerical results compare well with experimental results, but the computation time is very long.

From 1996 to 1998, Defense Advanced Research Project Agency (DARPA) funded a 3-year project on "Laser Forming for Flexible Fabrication" [62, 33]. The research team consisted of Boeing Company, Massachusetts Institute of Technology, Native American Technologies Company, Newport News Shipbuilding Company and the Pennsylvania State University. One of the activities the MIT research team was involved in was the development of a finite element model to predict the metal displacement during heating process and the resulting out-of-plane distortion. MIT Ocean Engineering Fabrication Laboratory researchers have performed time domain 3D thermo-elastic-plastic finite element analysis of laser line forming [18]. Since a smaller sized plate was used in numerical simulation to cut the computation time, when compared with experimental results, the numerical results for temperature typically involve a faster cool-down, and the final angular displacement in numerical simulation was smaller than experimental results.

The inaccuracy and inefficiency of the available numerical solution procedures motivate us to develop an efficient and accurate simulation method, which can be used for full scale simulation of laser or flame forming with better characterization of the thermo-mechanical process.

1.2.2 Heating process design

In a series of papers, Ueda et al. [58] [59] [60] [57] addressed a wide range of issues in the development of computer-aided process planning system for plate bending by line heating. They assumed that the target surface is given by a height function of the form $z = h(x, y)$. In the first report [58] they computed the strains caused by deformation from the initial configuration to the final one using a large displacement elastic FEM model. Second, they decomposed the computed strain components in x-y plane into in-plane (average strains of upper and lower surfaces, see Figure 1-1 (a)) and bending components (half of the difference of strains of upper and lower plate, see Figure 1-1 (a)) and displayed the distribution of their principal values on a graphic

display. Third, they chose the heating zone where the magnitude of principal in-plane strain was large and select the heating direction normal to the principal strain. Finally, from the distribution of bending strain, the region where the absolute value of bending strain was large was selected as the additional heating zone. The heating direction was taken normal to the direction of the principal strain with the maximal absolute value. In the second report, Ueda et al. [59] analyzed some practices for plate bending in shipyards from the point of view of inherent strain. Based on inherent strain analysis, the forming procedures of three simple models of curved plates (pillow shape, saddle shape, and twisted shape) were examined. The theoretical prediction was found to be in good agreement with the real practice of skilled workers. In the third report, Ueda et al. [60] investigated the relation between heating condition and deformation. By analyzing the governing equations, they obtained the significant factors and secondary factors affecting the deformation of the plate. They developed the similarity rule which holds for the line heating process under the assumption of ideal material properties which do not depend on temperature. In the fourth report, Ueda et al. [57] investigated the influence of some of the secondary factors in line heating via numerical simulation. The results showed that their separation of significant factors and secondary factors was reasonable.

These four reports are valuable for laser heating process design. However, their method has the following drawbacks. The computation of the strains necessary to form the plate using the large displacement elastic FEM model, usually yields both positive and negative principal in-plane strains, which cannot be realized by the line heating method. This leads to either a larger or a smaller doubly curved surface after line heating and causes a serious problem in the assembly stage. Another shortcoming of their method is that principal directions of in-plane strains (average strains of upper and lower faces of the plate, see Figure 1-1 (a)) and bending strains (half of the difference of strains of upper and lower faces of the plate, see Figure 1-1 (a)) to form the plate are different and makes the planning of heating path and conditions very complex and difficult. The state-of-the-art IHI system [19] is based on this methodology and hence it inherits the above deficiencies.

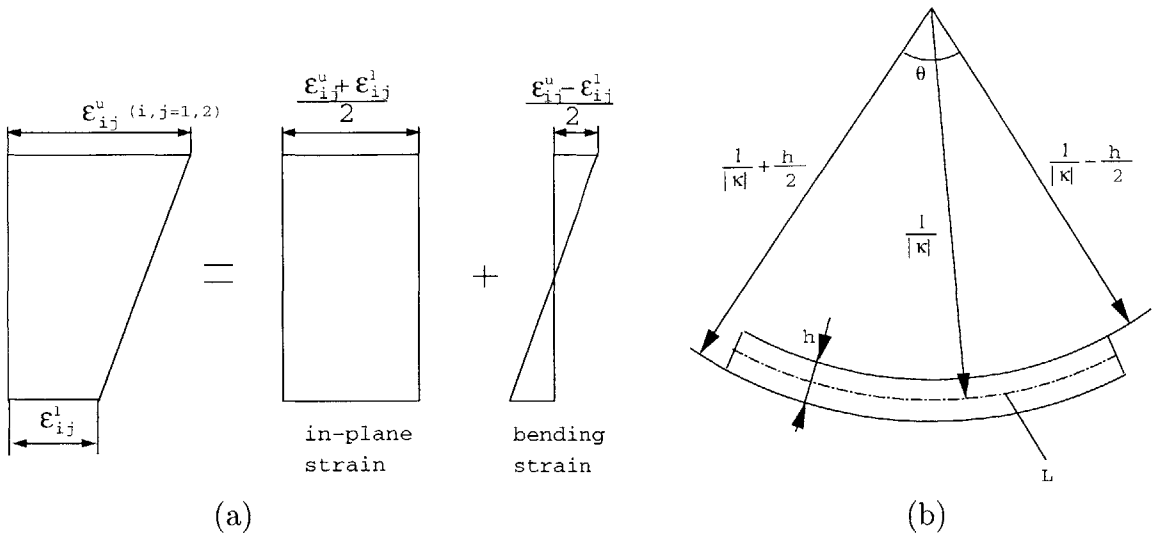

Figure 1-1: (a) The strain components in x-y plane (directions 1, 2 correspond to x, y directions) of top and bottom sides of the plate can be decomposed into in-plane and bending strains. (b) The bending strains are determined by elementary geometry.

Masubuchi and Shimizu [36] have developed a process determination method for laser forming and final shape analysis. In their report, a heating line by a laser beam onto a plate was represented with bending moments arranged in a pair of lines. These moments were further applied on nodes. The total bending moment was a function of the length of a heating line on a plate. The total bending moment, per unit length of the heating line, was considered as a constant and was determined by either experiments or simulation by thermo-elastic-plastic FEM analysis. The strain or displacement fields for pre-determined heating lines were calculated. Given a final shape, a linear elastic FEM program based on thin plate theory was used to calculate the strain distribution. The authors then used a genetic algorithm to obtain a set of heating parameters by a best fit approach.

Jang and Moon [21] compute the lines of curvature of a design surface and evaluate the extrema of principal curvature along them. Then they group them based on the principal curvature directions and distance between them. Once groups are formed, a linear regression is applied to obtain the heating lines. This method is rudimentary and may only work for simple surfaces such as cylinders. The reasons are (1) The initial shape is not taken into consideration and trimming of excess material at the

assembly stage is needed. (2) The grouping of extrema of principal curvatures is very rough. (3) The group of extrema of principal curvature may form a curve and approximation by a straight line may not be appropriate. (4) The heating conditions such as power and speed of the heat source are not provided.

1.2.3 Development of doubly curved surface

In engineering applications, there exist two kinds of surfaces, developable surfaces and non-developable surfaces, which are also called singly and doubly curved surfaces, respectively. A developable surface has zero Gaussian curvature at all points, while a non-developable surface has non-zero Gaussian curvature at least in some region. A developable surface is highly favorable in metal forming since it can be formed only by bending without tearing or stretching. For this reason, developable surfaces are widely used in manufacturing parts whose materials are not easily amenable to stretching. However, surfaces of many engineering structures are commonly fabricated as doubly curved shapes to fulfill functional requirements such as hydrodynamic, aesthetic, or structural. For example, a large portion of the shell plates of ship hulls or airplane fuselages are doubly curved surfaces.

Given a three-dimensional doubly curved design surface, which represents a face of a curved plate or shell, the first step of the fabrication process is flattening or planar development of this surface into a planar shape so that the manufacturer can not only determine the initial shape of the flat plate but also estimate the strain distribution required to form the shape. Then the planar shape is formed into an approximation of the design surface by various approaches such as forming by matching dies, by continuous hammering, or by line heating using an oxyacetylene torch, laser, or heat by induction. For plates in shipbuilding industry, this is usually achieved by roller bending followed by line heating, or by line heating only. This planar shape is usually not unique since, theoretically, a large variety of initial planar shape can be deformed into the curved surface if adequate stretching or shrinkage is allowed. However, in real practice, a planar development corresponding to minimum stretching or shrinkage is highly desirable for the following reasons: (1) it saves material; (2) it reduces the

work needed to form the planar shape to the doubly curved design surface.

Early surface development procedures were implemented in shipyards based on geodesic development [37], mainly for ship hull plates whose Gaussian curvature is very small. More recently, Letcher [28] presents a basic geometric theory for flattening and fabrication of doubly curved plates. The mapping from the curved surface to its planar development is modeled by adding in-plane strains to the curved surface. The strain field is obtained by solving a generalized Poisson's equation with the source term equal to the Gaussian curvature. However, since the problem is formulated as a boundary value problem, a good solution relies on a well specified boundary condition which is hard to know beforehand. Also, the differential equation is formulated in an orthogonal coordinate system and it is not trivial to formulate in a non-orthogonal coordinate system. Ueda et al. [58] investigate the relation between the final shape of a plate and the inherent strain. They compute the strain caused by deformation from the initial configuration to the final one using large deformation elastic FEM analysis. Since the initial configuration is usually the projection of the doubly curved surface on x-y plane, their approach can only be applied to the cases when the doubly curved surface is relatively flat, i.e. the curvature is small. More recently, Ishiyama et al. [19] develop doubly curved surfaces by using elastic FEM analysis. The disadvantage is that the principal directions of the bending strains and those of the inplane strains are usually not the same, which results in more heating lines.

Manning [30] developed a procedure for surface development based on an isometric tree. A tree of lines with a spine and branches is first drawn on the curved surface. Then the spine and the branch curves are developed isometrically onto planar curves, using the geodesic curvature of the spine and branches on the surface as the curvature of the planar curves. The envelope of the developed pattern forms the planar developed shape. Obviously, the shape of the planar development depends on the choice of the spine and branch curves, since in this development scheme, the stretching along both the spine and branch curves is zero. This procedure is applied in the shoemaking industry. If it is applied to metal forming, it causes larger initial shape as needed, resulting in waste of material. Another disadvantage of this procedure is that it does

not provide the field of strain (deformation). Hinds et al. [16] develop doubly curved surfaces by first approximating them by quadrilateral facets, then flattening these platelets allowing some gaps in the developed patterns. This method is applied in the clothing industry. The disadvantage of this method is that the developed shape depends on the starting edge chosen and again if used in metal forming, it is not guaranteed that the forming process is realizable from the planar shape to the curved surface. Azariadis and Aspragathos [2] extend the work by Hinds et al. [16] to reduce the gaps by minimizing the Euclidean distances of pairs of corresponding points between two successive strips. The quality of the development approaches in [16] [2] largely depends on the choice of guide-strip or starting edge.

1.3 Problem statement

In summary, the available numerical solutions in line heating mechanisms predict deformations either inaccurately, or inefficiently, or both. Full sized FEM simulation of the line heating process is usually too time consuming, while other simplified models are inaccurate or empirical. The available methodologies for heating process design do not take into account either the differential geometrical properties of the design surface, or the characteristics of the line heating process. The current methods for computation of the strains necessary to form the plate by FEM usually yield negative strain values. The negative strains in the flattening process correspond to positive strains in the forming process, which cannot be realized by the line heating method. These methods also make the orientations of the principal in-plane strains and bending strains different and the resulting planning of heating path and conditions is very complex.

This thesis research aims to develop the algorithms for accurate and efficient simulation of the line heating process, and for heating line design based on surface development. In other words, the thesis intends to solve the following problems:

(1) Modeling of the thermo-mechanical process by using a more efficient three-dimensional finite element method.

(2) Developing a simplified thermo-mechanical model which further reduces simulation time so that the model can be used in real time process planning.

(3) Developing a surface development algorithm which can be used for heating path planning.

1.4 Thesis outline

The remainder of the thesis is arranged as follows:

Chapter 2 presents a three-dimensional finite element model for metal forming by line heating using adaptive mesh rezoning.

Chapter 3 presents a simplified thermo-mechanical model for the prediction of temperature field and the resulting angular deformations of metal plates due to line heating.

Chapter 4 studies the effects of variations of some important parameters on line heating such as heating line location, heat input, heat source velocity, spot size, etc.

Chapter 5 presents an algorithm for optimal development of doubly curved surfaces. The development produces the planar initial shape, as well as the strains need to produce by line heating in order to fabricate the planar shape into the doubly curved design surface.

Finally, Chapter 6 concludes the thesis, summarizes its contributions, and presents suggestions for future research.

Chapter 2

FEM model for metal forming by line heating

2.1 Introduction

The process of shell forming by line heating is a coupled nonlinear thermo-mechanical process, which makes the complete simulation difficult. Numerical simulations of line heating process such as FEM analysis have achieved some success in predicting the final state of distortion, but the computation time is typically very long (in the order of days) which makes FEM not suitable for real-time analysis. In this chapter, a finite element model is developed for thermo-mechanical analysis of the process of metal plate forming by line heating. Rezoning technique is adopted to greatly reduce the simulation time. The effects of the refinement of mesh size on temperature distribution and final distortion are studied. Comparison between numerical and experimental results shows a good agreement in final distortion of the formed plate.

2.2 Rezoning technique for line heating process

During the process of shell forming by line heating, the heat source moves and only the area which is very near the heat source undergoes large amount of heat transfer and plastic strains. The remaining areas have small changes of temperature and

small amount of stresses and strains, which implies that a sparse mesh in these areas is sufficient. The ordinary FEM analysis, which uses a uniform fine mesh along the entire heating line greatly increases the number of degrees of freedoms, making the analysis slow. In order to obtain convergent and accurate results in a reasonable time, we use a 3D rezoning technique in the FEM simulations of laser forming process. This involves remeshing of the metal plate so that the area directly under the laser beam has a denser mesh while other areas have sparser meshes (see Figure 2-1 for an illustration). Rezoning technique has been used in 2D simulation of welding process by Brown and Song [8], and a similar idea, adaptive FEM for transient thermal analysis has been employed by Probert et al. [46].

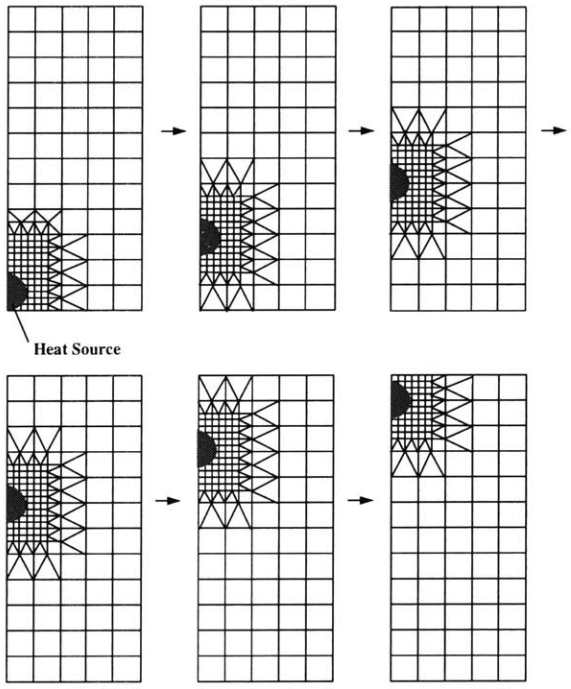

Figure 2-1: Different meshes for incremental analysis

The plates formed by line heating are usually treated as thick plates, since it is the gradient of the temperature across the thickness that provides the mechanism to bend these plates. Therefore, 3D FEM analysis is necessary and a 3D mesh needs to be generated. For our research, 8-node brick elements and 6-node triangular prism

elements are the two types of elements used in analysis. Mesh generation is carried out first on the upper or lower surface of the plate, which generates quadrilateral elements and triangular elements (see Figure 2-1), then 3D mesh can be generated by taking offsets across the plate thickness. In order to accurately capture the characteristics of the laser forming process, we choose a mesh size which increases exponentially across the thickness of the plate, being finer near the heated side of the plate.

2.2.1 Generation of rezoning meshes

An algorithm has been developed to generate rezoning meshes for rectangular plates. It reads the necessary information for the mesh to be generated from an input file, and the output file from the thermal and mechanical analysis in the previous step (if any), then generates the input file for analysis in the next step. The basic procedures of this mesh generation code are:

(1) Generate dense grid for the planar area of one side of the plate surface. The size of this dense grid is the same as that of the finest mesh at the region under laser beam. The rezoning meshes are generated by picking up the corresponding grid points.

(2) Generate previous mesh, i.e., get the correspondence between the grid points and the node points of the previous mesh.

(3) Read the node temperatures (from the output file of the thermal analysis of the previous step) or the displacements and elemental stresses at each node (from the output file of the mechanical analysis of the previous step) and interpolate this data at the grid points.

(4) Pick up the corresponding grid points and generate new mesh in 2D according to the input file.

(5) Take the offset of planar mesh in the direction of the plate thickness and generate 3D mesh. The thickness of layers increases across the thickness of the plate, being finer near the heated side.

(6) Write the node coordinates, element formation, and the information of convection/radiation faces (the corresponding elements are in the layers at the surface).

(7) According to the node and grid point correspondence, obtain the initial temperature at each node (for thermal analysis) or the initial stresses in each element (for mechanical analysis) for the new mesh.

(8) Generate input files for thermal and mechanical analysis for the new mesh.

2.3 Finite element model for laser line heating

According to the mechanism of laser forming process, we have developed a finite element model for thermal and mechanical analysis of this process. The ABAQUS software is used for FEM analysis.

2.3.1 Thermal boundary condition

Boundary heat transfer is modeled by natural heat convection and radiation. Convection follows Newton's law, the rate of the loss of heat per unit area in Wm^{-2} due to convection is

$$q = h_c(T_s - T_a) \tag{2.1}$$

where the coefficient of convective heat transfer is a function of the difference between the wall temperature T_s and the environment temperature T_a and of the orientation of the boundary [54] given by:

$$h_c = \frac{k_s N_u}{L}. \tag{2.2}$$

where k_s is the thermal conductivity of the metal plate; N_u is the Nusselt number, and L is the characteristic length of the plate (or surface). For horizontal plane surfaces with surface area A_s and perimeter p, $L = A_s/p$, and for vertical surfaces, L is the

height. If we denote the Rayleigh number by Ra_L, the Nusselt number is defined by:

$$N_u = b(Ra_L)^m, \tag{2.3}$$

where for horizontal surfaces facing upward,

$$\begin{aligned} b = 0.54, \quad m = \frac{1}{4}, \quad when \;\; 10^4 < Ra_L \leq 10^7 \\ b = 0.15, \quad m = \frac{1}{3}, \quad when \;\; 10^7 < Ra_L < 10^{11} \end{aligned} \tag{2.4}$$

for horizontal surfaces facing downward,

$$b = 0.27, \quad m = \frac{1}{4}, \quad when \;\; 10^5 < Ra_L < 10^{11} \tag{2.5}$$

for vertical surfaces

$$\begin{aligned} b = (\frac{Pr}{2.5 + 5.0\sqrt{Pr} + 5.0Pr})^{\frac{1}{4}}, \quad m = \frac{1}{4} \\ when \;\; 10^4 < Ra_L < 10^9 \end{aligned} \tag{2.6}$$

The Rayleigh number is given by $Ra_L = Gr_L \cdot Pr$, where Gr_L is the Grashof number, and Pr is the Prandtl number. Both the Grashof number and the Prandtl number are functions of ambient air properties and temperature differences between the wall and the environment. The Grashof number is defined as

$$Gr_L = \frac{g\beta(T_s - T_a)L^3}{\nu^2}, \tag{2.7}$$

where g is the gravitational acceleration; β is the coefficient of thermal expansion of air; T_s and T_a are the temperatures (in degrees ^oC or K) of the metal plate and air, respectively; L is the characteristic length of the plate; ν is the kinematic viscosity of air. The Prandtl number Pr is defined as

$$Pr = \frac{\rho C_p}{k_a}\nu = \frac{\nu}{\alpha} \tag{2.8}$$

where C_p is the specific heat of air, ρ the air density, k_a the thermal conductivity of air, and $\alpha = \frac{k_a}{C_p \rho}$ is the thermal diffusivity of air.

The rate of the loss of heat per unit area in Wm^{-2} due to radiation [54] is

$$q = 5.67 \times 10^{-8} \varepsilon (T_s^4 - T_a^4), \tag{2.9}$$

where ε is the surface emissivity (nondimensional), whose value depends on the surface condition and the temperature of the metal plate. T_s and T_a are measured in degrees K.

2.3.2 Spatial distribution of heat flux

Heat flux from an oxyacetylene torch or a laser beam is usually modeled as Gaussian distribution [56]. In this project, the accurate measurements of energy distribution of the Nd:YAG laser system with fiber optic beam delivery and focus optics were performed using a charged coupled device (CCD) by researchers at the Applied Research Laboratory of Pennsylvania State University [62]. The Nd:YAG beam displays a Gaussian distribution with an annular lobe, the amplitude of which is approximately 12% of the amplitude of the inner lobe. The outer lobe is believed to be a higher-order transverse mode caused by interaction of the beam and fiber. About 30% of the beam power is distributed in the outer lobe. The outer lobe has the shape of the sine (cosine) function. For the heating condition used for processing the Inconel plates, the inner lobe is 27.5 mm in diameter and the center of the outer lobe is 59.4 mm. Based on these data, the composite beam profile can be expressed as:

$$q''(r) = \begin{cases} q_{max} e^{cr^2} & r \leq r_2 \\ q_{max} \left[c_1 + c_2 \sin\left(\frac{r - r_2}{r_1 - r_2} \frac{\pi}{2} \right) \right] & r > r_2 \end{cases} \tag{2.10}$$

where q_{max}, r_2, c, c_1, c_2 are unknown variables, and $r_1 = \frac{59.4}{2} = 29.7$ mm. Denote Q the power of the laser, and p the absorption rate. The unknown variables satisfy the following conditions:

(1) at $r = r_0 = \frac{27.5}{2} = 13.75$ mm:

$$q_{max} e^{cr_0^2} = 0.12 q_{max} \tag{2.11}$$

(2) at $r = r_1 = 29.7$ mm:

$$q_{max} \left[c_1 + c_2 \sin\left(\frac{r - r_2}{r_1 - r_2} \frac{\pi}{2} \right) \right] = 0.12 q_{max} \tag{2.12}$$

(3) at $r = r_2$, compatibility between inner and outer regions:

$$q_{max} e^{cr_2^2} = q_{max} c_1 \tag{2.13}$$

(4) The inner region has heat flux $0.7Q \cdot p$:

$$2\pi \int_0^{r_2} q_{max} e^{cr^2} r dr = 0.7Q \cdot p \tag{2.14}$$

(5) The outer lober has heat flux $0.3Q \cdot p$:

$$2\pi \int_{r_2}^{2r_1 - r_2} \left[c_1 + c_2 \sin\left(\frac{r - r_2}{r_1 - r_2} \frac{\pi}{2} \right) \right] r dr = 0.3Q \cdot p \tag{2.15}$$

After solving the above 5 equations (2.11-2.15), we obtain

$$\begin{aligned} q_{max} &= p6.4815 \times 10^6 \ W/m^2 \\ c &= 1.1215 \times 10^4 / m^2 \\ c_1 &= 6.80757 \times 10^{-4} \\ c_2 &= 0.11932 \\ r_2 &= 25.5mm \end{aligned}$$

The composite laser beam profile is shown in Figure 2-2.

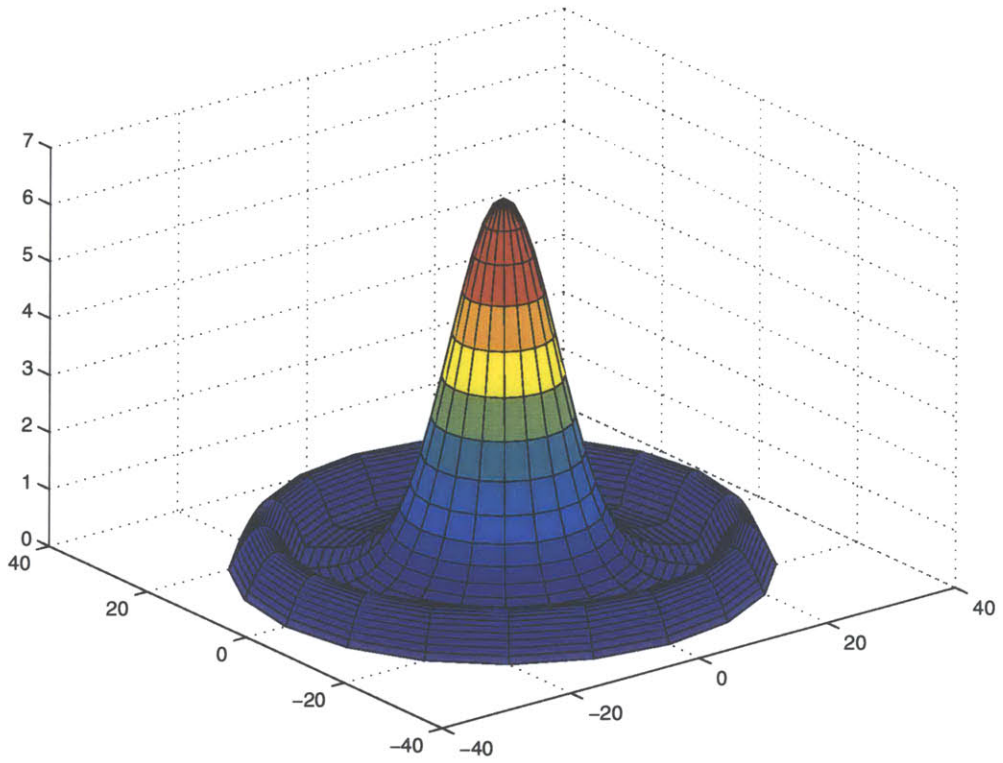

Figure 2-2: The composite laser profile (spatial heat distribution)

Energy distribution of the laser is also characterized by the approximate beam diameter (spot size) as a function of distance from the focus optics to the work-piece (stand-off distance). Spot size was measured from burn patterns obtained from Cotronix board, which is a fiber based low temperature refractory material, after a short period (2 seconds) of irradiation using various stand-off distances. The measured spot size for the above heat distribution is 22 mm, which corresponds to a stand-off distance of 18.5 cm. Researchers at the Applied Research Laboratory of Pennsylvania State University [62] suggest to use a Gaussian distribution within an equivalent diameter to simplify the heat flux distribution. In chapter 3 this idea is used.

When the spot size is enlarged by increasing the stand-off distance, the size of the inner region increases. Here we assume the size of the inner region increases proportionally to the spot size. For a spot size of 25.4 mm, the inner region has a diameter of 31.75 mm. To make the FEM simulation easier, the heat flux region is

modeled as a truncated Gaussian distribution, along with a uniform distribution:

$$q''(r) = \begin{cases} q_{max}e^{cr^2} & \text{if } r < 15.875 \text{ mm} \\ q_0 & \text{if } 15.875 \text{ mm} < r < 33.9 \text{ mm} \end{cases} \tag{2.16}$$

where $q_{max} = p \cdot 4.8740 \times 10^6 W/m^2$, $c = 8.4132 \times 10^3/m^2$, $q_0 = p \cdot 3.5422 \times 10^5 W/m^2$

2.3.3 Material properties of mild steel plates

Material properties of the mild steel plates used during the experiments are shown in the following [10] [7]:

1. Density: $7800 kg/m^3$.

2. Thermal properties: The thermal conductivity k, specific heat C_p and convective heat transfer coefficients are shown in Table 2.1. In the table, "–" means either the data are not available (for thermal conductivity and specific heat) or are not calculated (for convective heat transfer coefficients).

3. Mechanical properties are shown in Table 2.2. Young's modulus and yield stress are given small, finite values at high temperatures to avoid difficulties with numerical convergence [7].

2.3.4 Mechanical boundary conditions

In mechanical analysis, necessary constraints are added to eliminate rigid body movement according to the fixtures used in real experiments. In case of heating along the centerline of the plate, symmetric condition is used to reduce the number of degrees of freedom.

Table 2.1: Thermal properties of the mild steel plate

Temperature T (^oC)	Thermal conductivity k $Wm^{-1}K^{-1}$	Specific heat C_p $Jkg^{-1}K^{-1}$	Convective heat transfer coefficient ($Wm^{-2}K^{-1}$)		
			h_{up}	h_{down}	$h_{vertical}$
0	51.9	450	–	–	–
75	–	486	–	–	–
100	51.1	–	7.64577	3.82242	9.54112
175	–	519	–	–	–
200	49.0	–	9.04495	4.52248	11.27280
225	–	532	–	–	–
275	–	557	–	–	–
300	46.1	–	10.0863	5.04315	12.55616
325	–	574	–	–	–
375	–	599	–	–	–
400	42.7	–	10.33564	5.16782	12.85799
475	–	662	–	–	–
500	39.4	–	10.52563	5.26282	13.09222
575	–	749	–	–	–
600	35.6	–	10.73691	5.36845	13.35495
675	–	846	–	–	–
700	31.8	–	10.89470	5.44735	13.5535
725	–	1432	–	–	–
775	–	950	–	–	–
800	26.0	–	11.0002	5.50010	13.6893
900	–	–	11.0997	5.54986	13.8178
1000	27.2	–	11.1744	5.58722	13.9176
1100	–	–	11.2140	5.60701	13.9738
1200	–	–	11.2592	5.62959	14.0393
1500	29.7	400	–	–	–

Table 2.2: Mechanical properties for mild steel

Temperature T (^oC)	Yield stress σ_y (MPa)	Young's modulus E (GPa)	σ_y at strain of 1.0 (MPa)	Thermal expansion coefficient α ($10^{-6}1/^oC$)
0	290	200	314	10
100	260	200	349	11
300	200	200	440	12
450	150	150	460	13
550	120	110	410	14
600	110	88	330	14
720	9.8	20	58.8	14
800	9.8	20	58.8	14
1200	–	2	–	15

2.4 Examples

2.4.1 Effectiveness of rezoning and mesh size

Results with coarse mesh

In order to verify the finite element model and the effect of rezoning, we performed numerical simulations of the $30.48cm \times 30.48cm \times 2.54cm$ mild steel plate under laser heating along its center line. The plate was assumed to deform freely, so we only did simulation on half of the plate due to symmetry condition. Both the simulations with and without rezoning were carried out on a SGI Onyx, 150 MHz R4400 with 128 MB RAM. The heat source moving velocity was 8 cm/min. An absorption rate of 68% was used. A constant surface emissivity of $\varepsilon = 0.5$ in Equation (2.9) was used in computation of heat loss due to radiation.

The FEM mesh without rezoning, and the temperature distribution during analysis are shown in Figure 2-3. When rezoning was applied, seven steps of analysis were carried out. The meshes and temperature distributions for the seven steps are shown in Figures 2-4 to 2-10.

The comparison of the temperature change at the backside center of the specimen, and the angular deflection of the plate computed at the edge of the middle cross section of the plate normal to the heating line are shown in Figure 2-11 and Figure 2-12 respectively. We see almost no difference between the results in temperature with and without rezoning. The difference between the angular deflections in the two cases is within 5%.

Table 2.3 summarizes the total simulation time with and without rezoning. We see here a reduction of computation time by a factor of about 3 if rezoning is used.

In general, rezoning becomes more efficient when the heating line is longer. If we denote the length of the heating line L, then for the static mesh shown in Figure 2-3, the total number of nodes is proportional to L, and the total simulation time is a function $f(L)$ of L. On the other hand, for FEM with rezoning, the number of nodes in each step can be kept almost constant, while the number of steps is proportional to

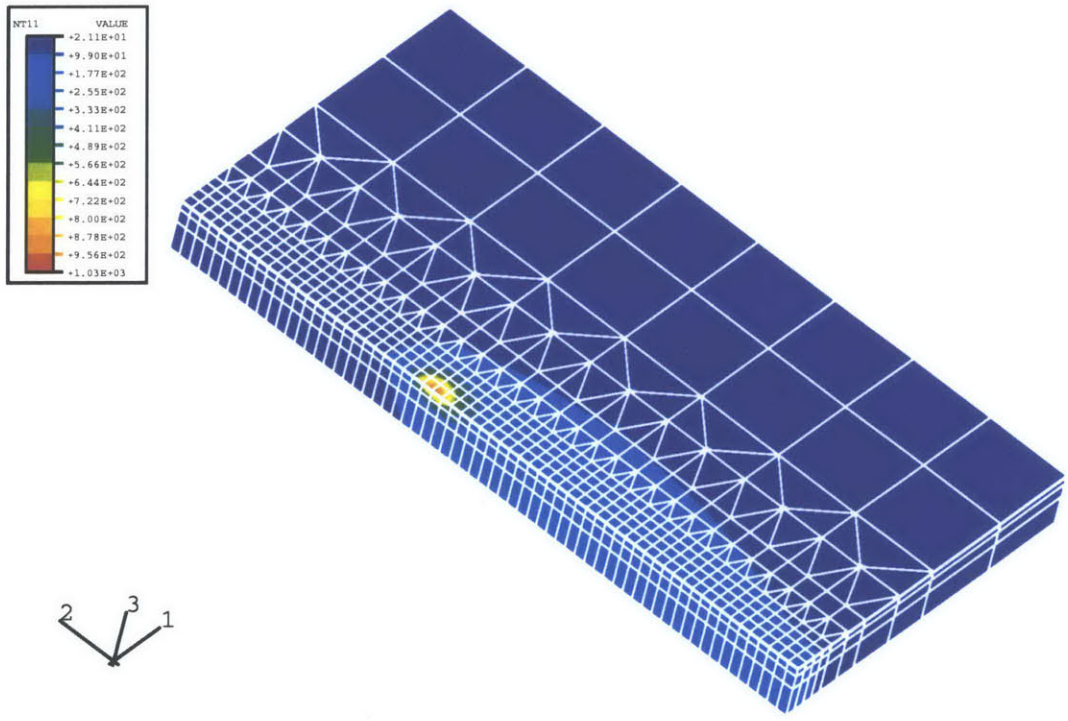

Figure 2-3: Mesh and temperature distribution during thermal analysis - coarse mesh without rezoning

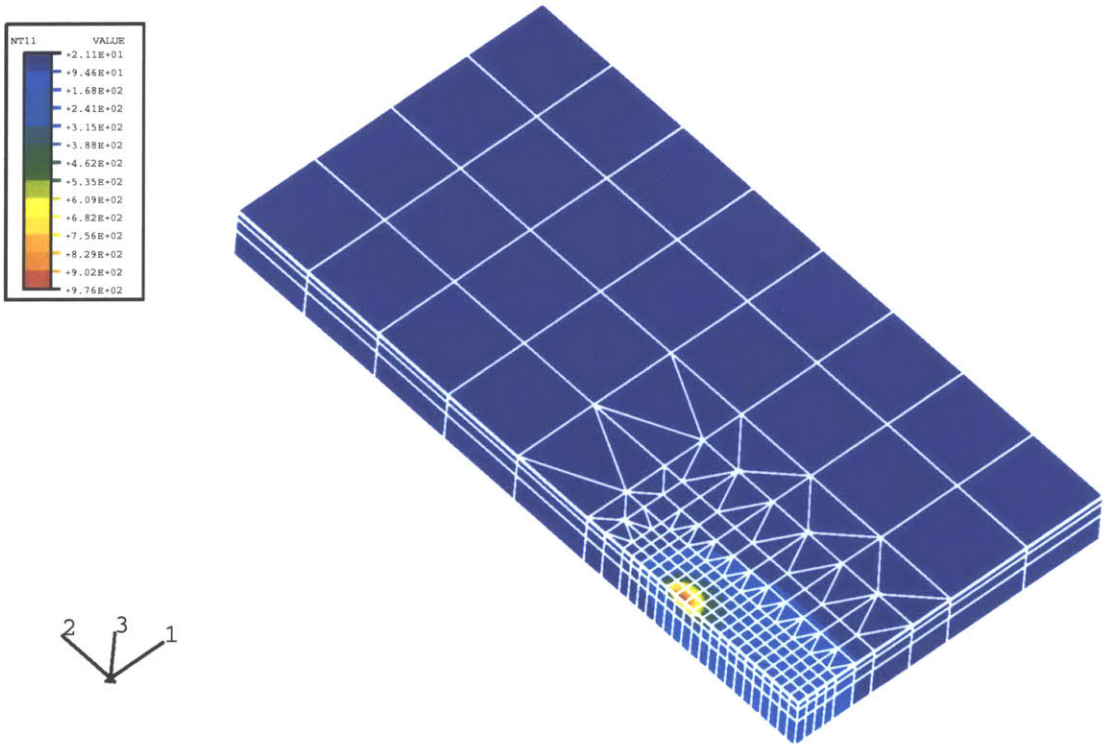

Figure 2-4: Mesh and temperature distribution at rezoning step 1 - coarse mesh

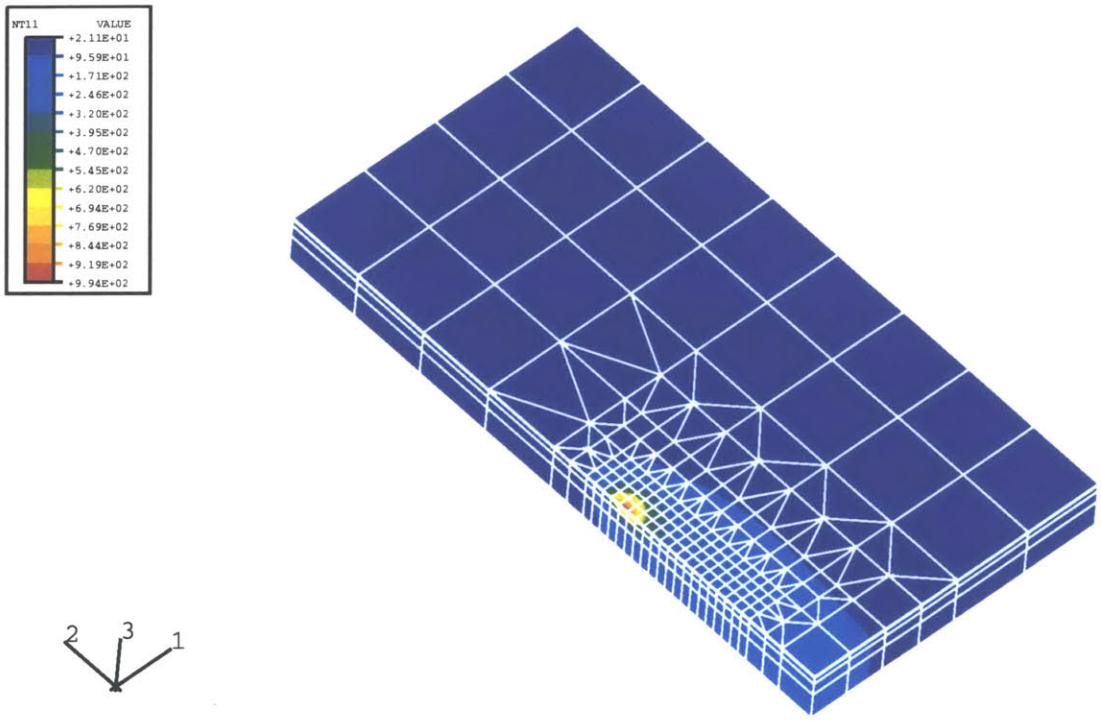

Figure 2-5: Mesh and temperature distribution at rezoning step 2 - coarse mesh

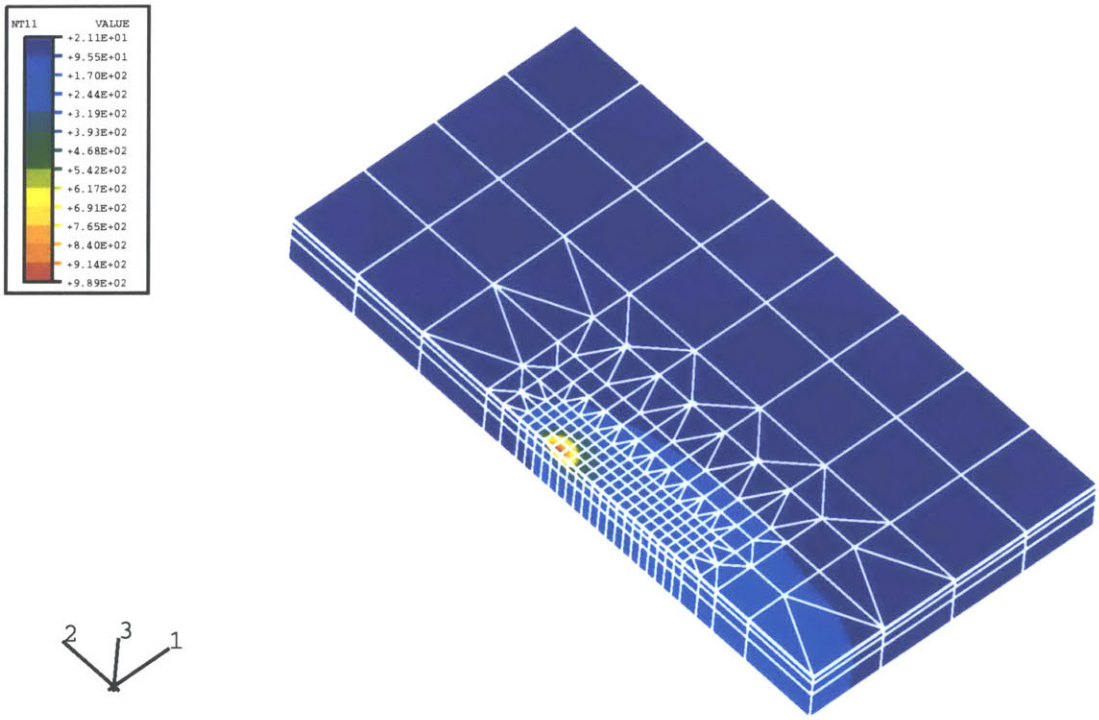

Figure 2-6: Mesh and temperature distribution at rezoning step 3 - coarse mesh

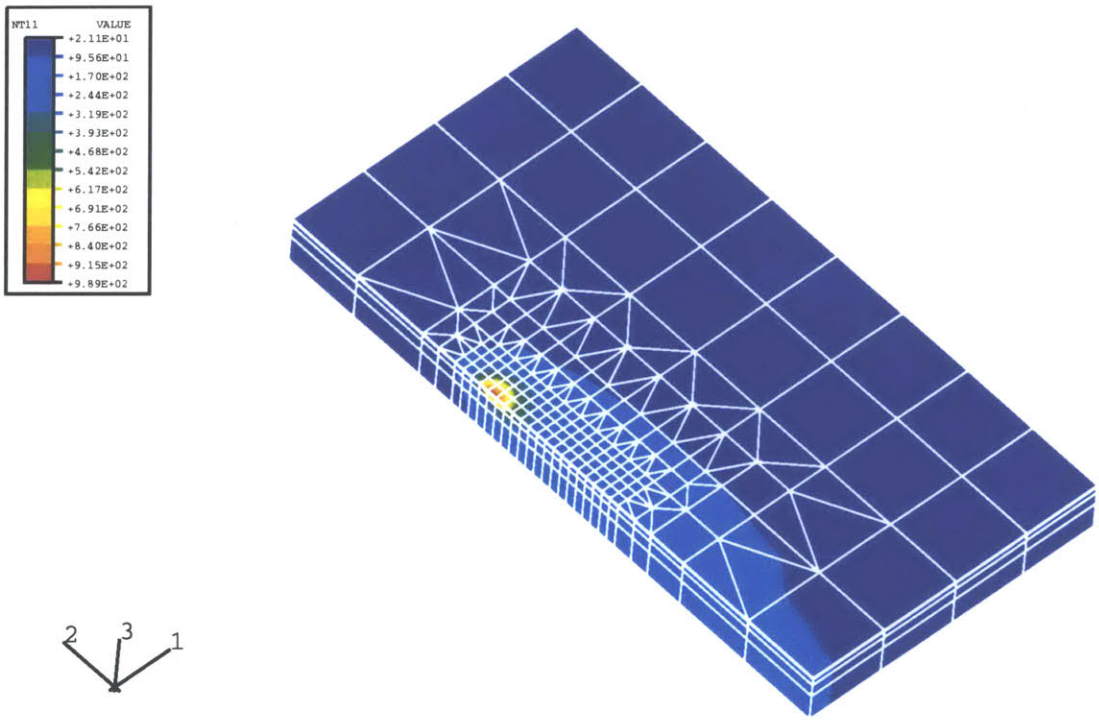

Figure 2-7: Mesh and temperature distribution at rezoning step 4 - coarse mesh

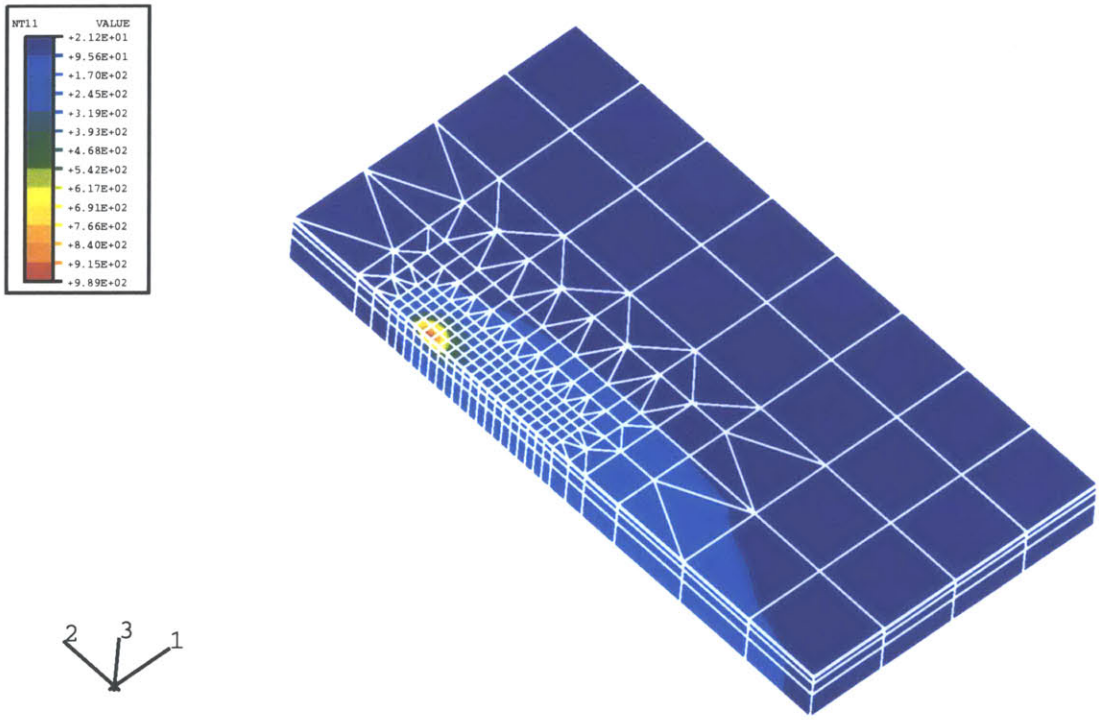

Figure 2-8: Mesh and temperature distribution at rezoning step 5 - coarse mesh

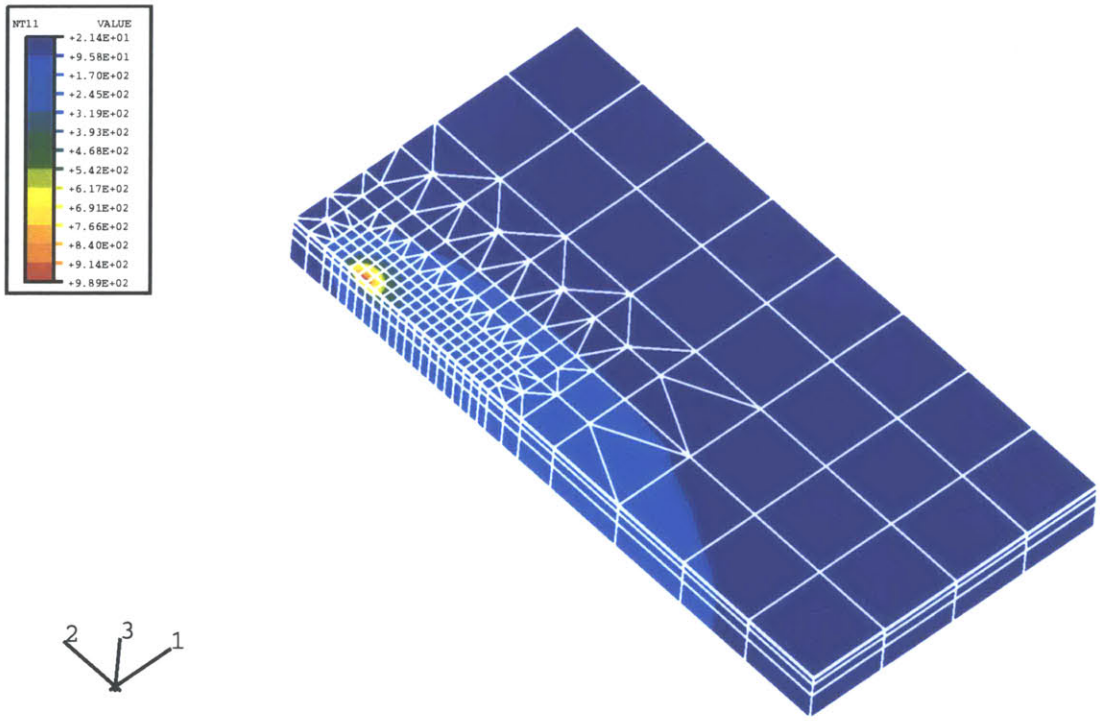

Figure 2-9: Mesh and temperature distribution at rezoning step 6 - coarse mesh

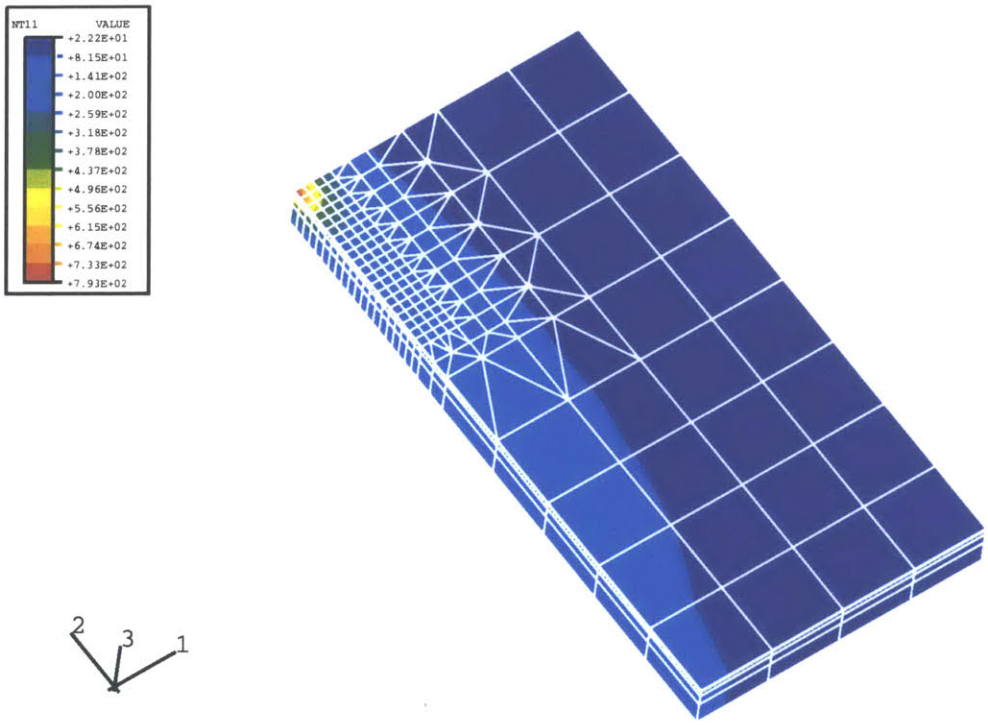

Figure 2-10: Mesh and temperature distribution at rezoning step 7 - coarse mesh

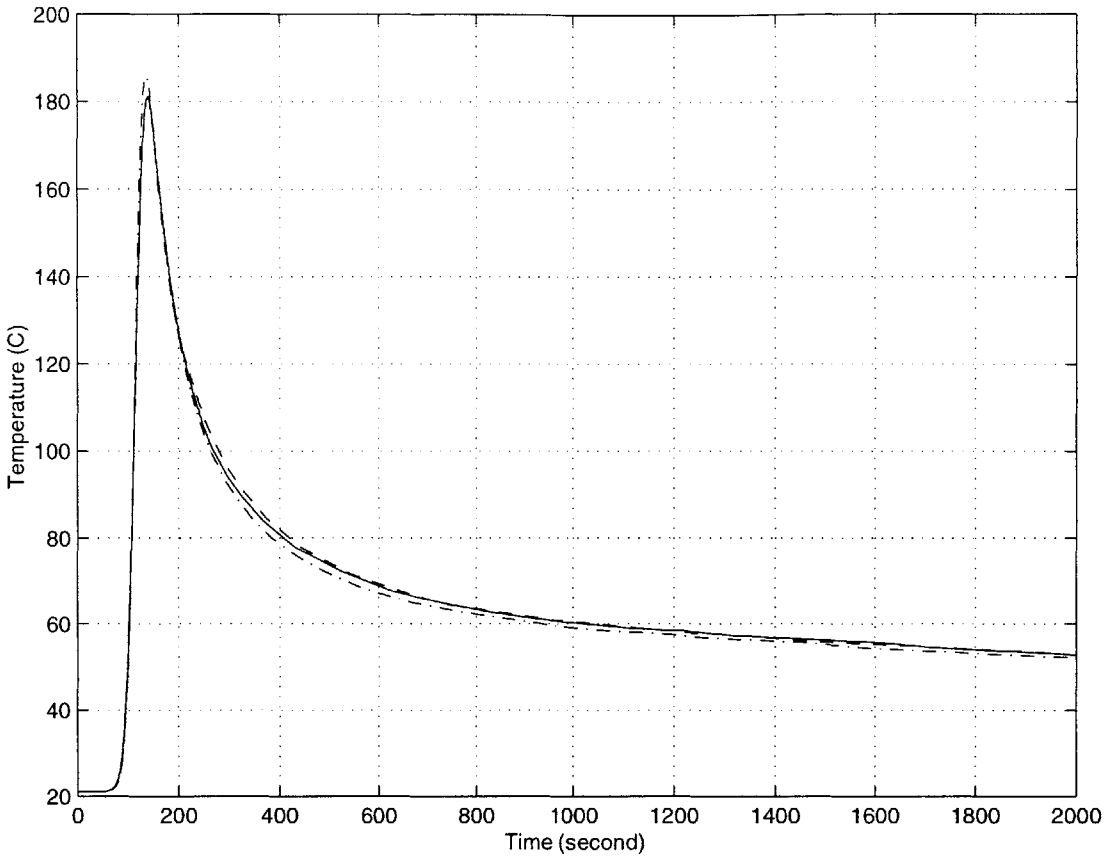

Figure 2-11: Calculated temperature vs. time at the backside center of the plate (solid line for coarse mesh without rezoning, dashed line for coarse mesh with rezoning, and dashdotted line for dense mesh with rezoning)

L, therefore the total simulation time with rezoning is proportional to L. If a direct solution method such as LDL^T decomposition is employed as the solver of linear equations in the FEM software, the order of $f(L)$ is usually L^2 [3]. If an iterative scheme such as conjugate gradient method is employed, $f(L)$ is usually of lower order such as $L^{\frac{3}{2}}$. For the ABAQUS FEM system we are using, numerical experiments show that the order of $f(L)$ is between $L^{\frac{3}{2}}$ and L^2, so as $L \to \infty$, $\frac{f(L)}{L} \to \infty$. Thus the ratio between the simulation time without and with rezoning increases as L increases, i.e., rezoning saves more time for larger problems in relation to smaller problems.

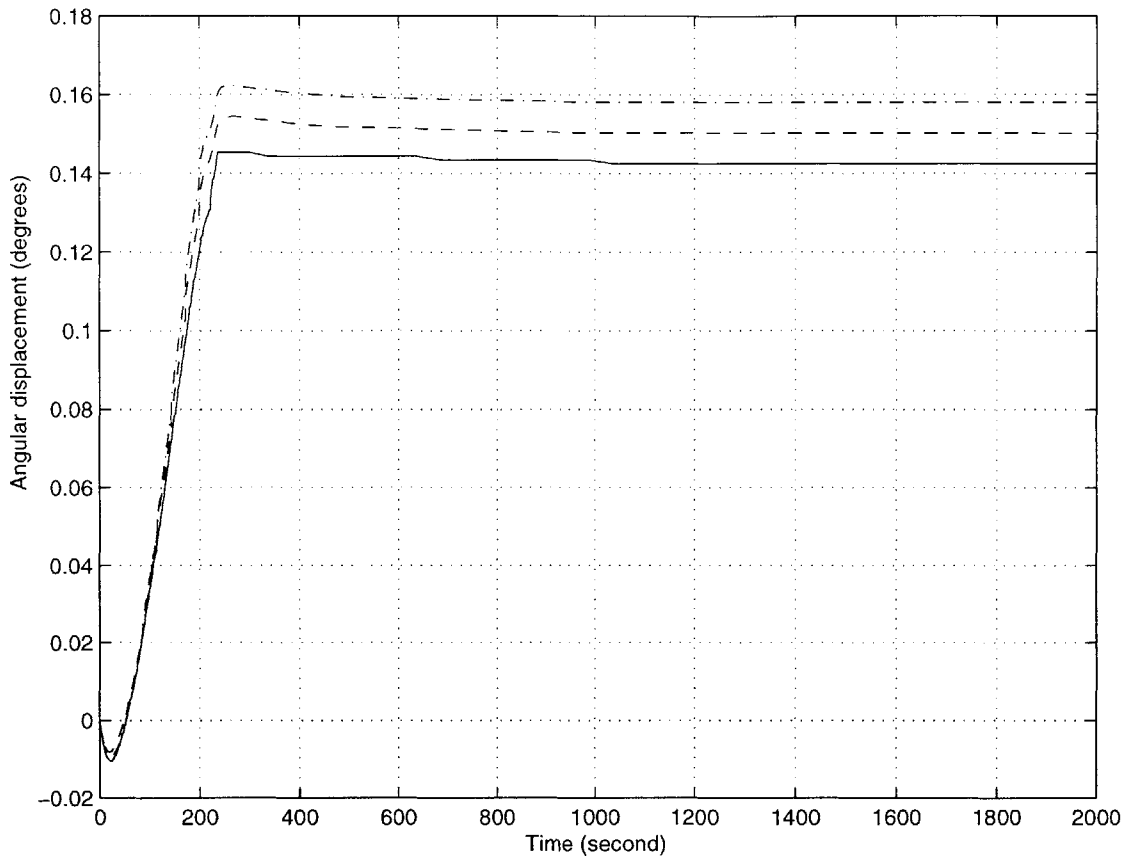

Figure 2-12: Calculated angular displacement vs. time at middle cross section of the plate (solid line for coarse mesh without rezoning, dashed line for coarse mesh with rezoning, and dashdotted line for dense mesh with rezoning)

Results with dense rezoning mesh

We then performed numerical simulation of the $30.48cm \times 30.48cm \times 2.54cm$ mild steel plate under laser heating along its center line by using a denser mesh. Again, seven steps of rezoning thermal-mechanical analysis were performed. The FEM mesh and temperature distribution during steps 1, 2, and 7 of the analysis are shown in Figures 2-13 to 2-15.

The temperature variations of the plate at the backside center of the plate are shown in Figure 2-11, and the angular displacement of the plate computed at the edge of the middle cross section of the plate normal to the heating line are shown in Figure 2-12.

The numerical results show a slight temperature change at the backside center of

Table 2.3: Simulation time with or without rezoning

	Analysis type	CPU time (sec)	wall clock time (sec)
with rezoning	thermal	8238	14711
	mechanical	7192	12537
	total	15430	27248
without rezoning	thermal	22416	35014
	mechanical	19955	28809
	total	42371	63823

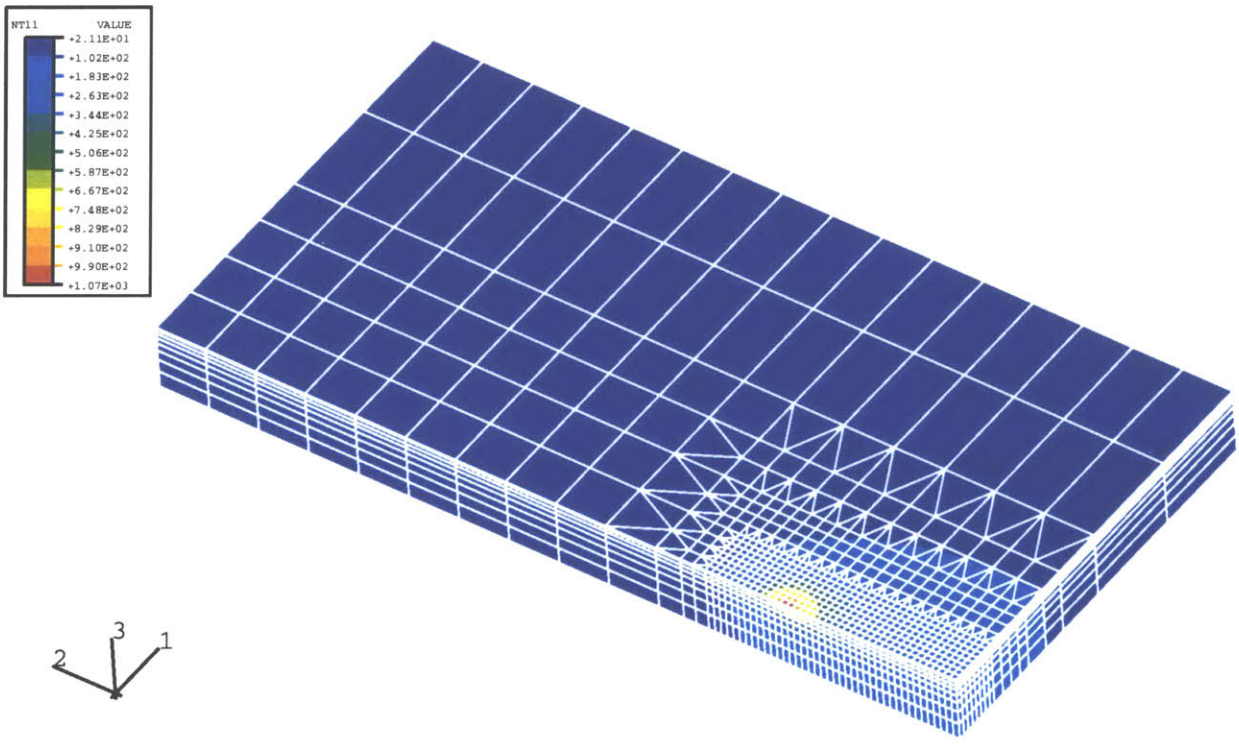

Figure 2-13: Mesh and temperature distribution at rezoning step 1 - dense mesh

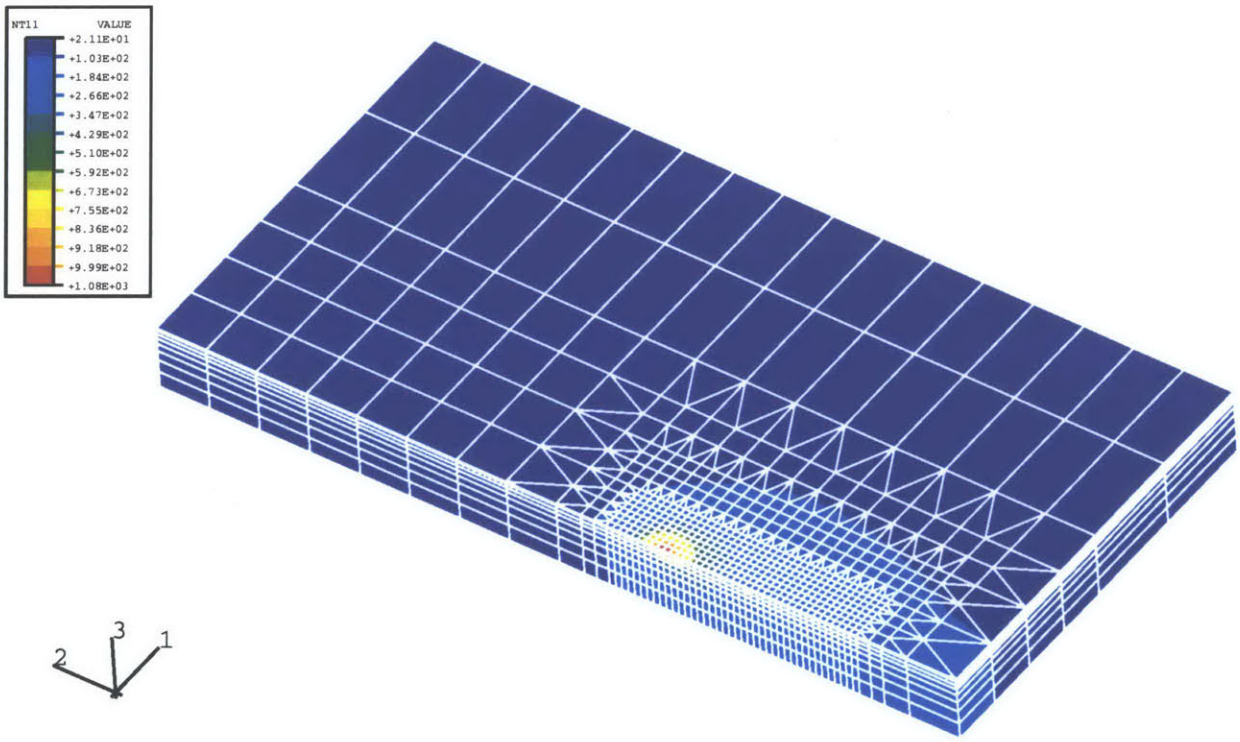

Figure 2-14: Mesh and temperature distribution at rezoning step 2 - dense mesh

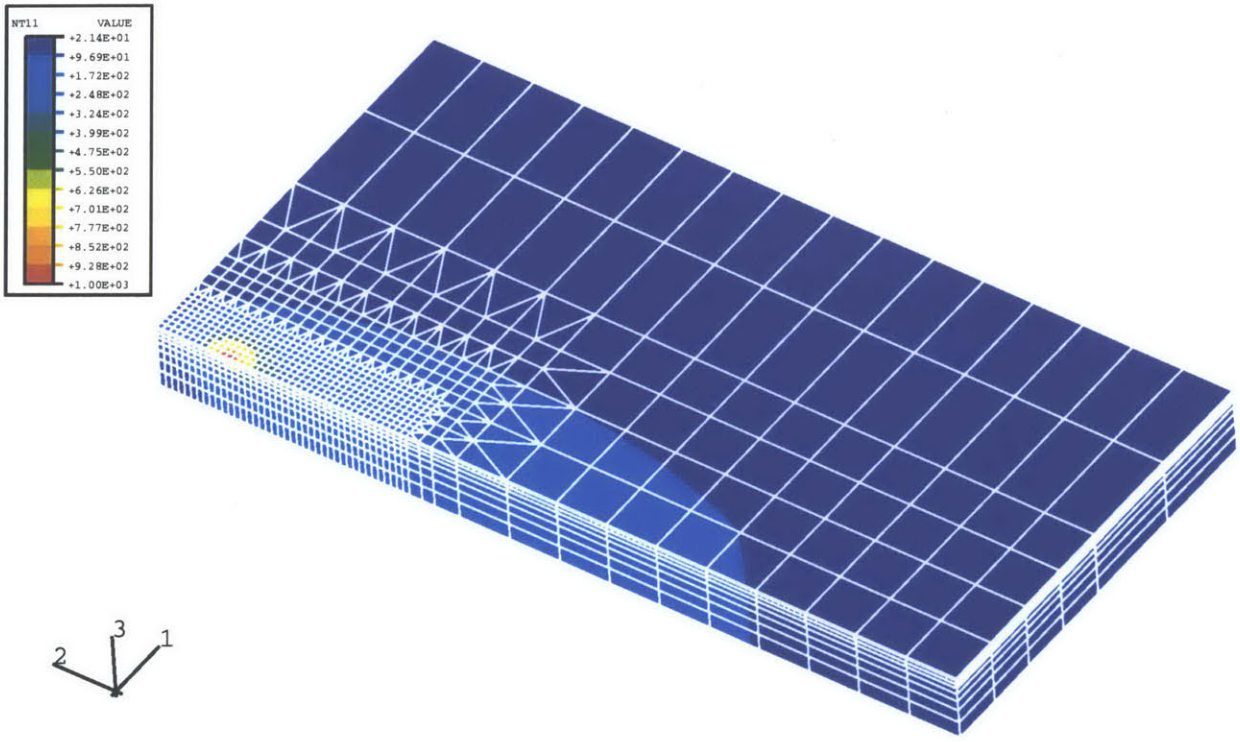

Figure 2-15: Mesh and temperature distribution at rezoning step 7 - dense mesh

the plate, and a slight increase in the final angular displacement are obtained when the denser rezoning mesh is used. This implies that relatively coarse mesh can be used for FEM analysis of the laser forming process on mild steel plates.

2.4.2 Comparison of FEM and experimental results

We verified our model by comparing the numerical results we obtained from our simulation with experimental results. The experiments were performed on $30.48cm \times 30.48cm \times 2.54cm$ mild steel plates with heating lines at various distances from the edge. The power of the laser is 2.6 kW, and the spot size is 25.4 cm, which corresponds to a stand-off distance of 20.6 cm. The heat flux is modeled by equation (2.16). We used the results from the experiments when the heating line was $11.43cm$ from the edge. The plates were clamped at two points during experiments (see Figure 2-16). The vertical displacements at 5 points were measured. The experimental setup is shown in Figure 2-16, where $d_1 = 2.54cm, d_2 = 6.35cm, d_3 = 3.81cm, d_4 = 11.43cm$. We performed detailed thermo-mechanical analysis for two cases: (1) Heat source moving velocity 7.62 cm/min; and, (2) heat source moving velocity 9.652 cm/min.

Experimental results for these two cases were obtained from the research team at Pennsylvania State University [62]. An absorption rate of 81.75% was used during numerical simulation based on parameter identification (see Chapter 3). The rezoning meshes for the first two steps are shown in Figure 2-17 and Figure 2-18. By using rezoning technique, computation time was reduced significantly. After the numerical simulation was complete, the displacements at the measuring points in Figure 2-16 were interpolated from those at the FEM nodes. The comparisons between the numerical and experimental results are shown in Table 2.4 and Table 2.5, where z_N is the numerical displacement in z direction; z_E is the experimental displacement in z direction; and Error is the relative error with respect to experimental results. We see that almost all the numerical results are within 15% of the experimental results. This shows the effectiveness of our FEM model.

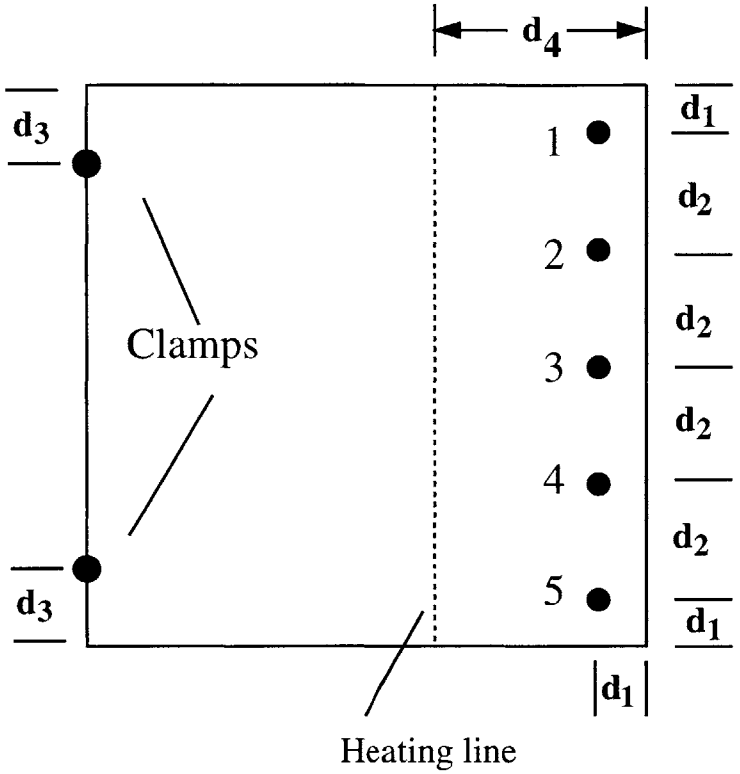

Figure 2-16: Heating pattern and measuring points in mild steel experiments

Table 2.4: Comparison of numerical and experimental displacements for case 1

Point	1	2	3	4	5
z_N (cm)	0.03792	0.03349	0.03162	0.03305	0.03678
z_E (cm)	0.03556	0.03175	0.02921	0.0381	0.03429
Error (%)	6.6	5.5	8.3	13.3	7.3

Table 2.5: Comparison of numerical and experimental displacements for case 2

Point	1	2	3	4	5
z_N (cm)	0.02719	0.02365	0.02219	0.02340	0.02648
z_E (cm)	0.03226	0.02667	0.02286	0.02413	0.03175
Error (%)	15.7	11.3	2.9	3.0	16.6

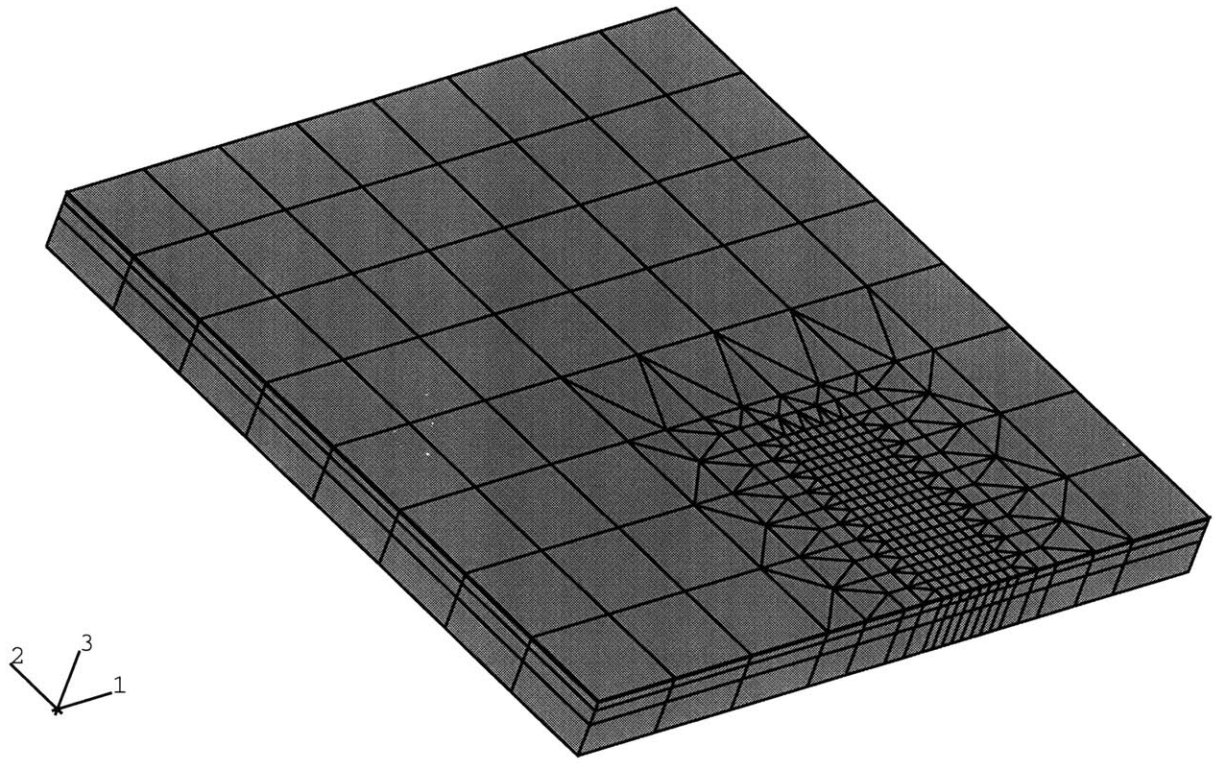

Figure 2-17: Mesh at rezoning step 1 for heating away from central line

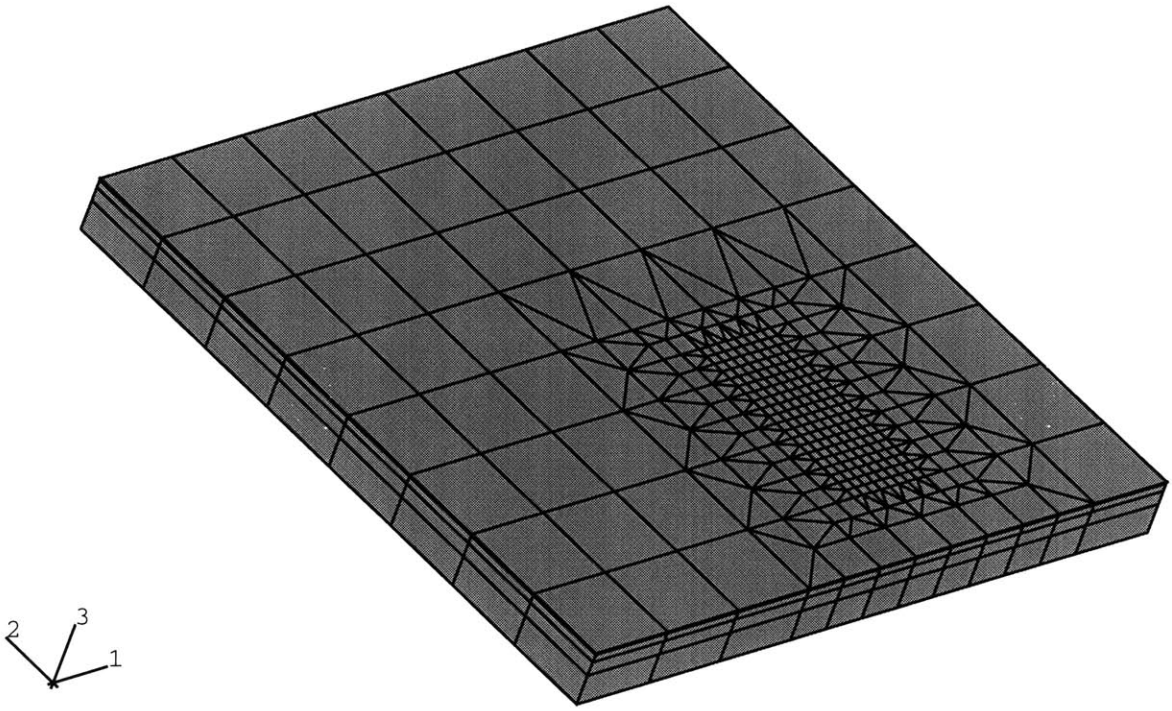

Figure 2-18: Mesh at rezoning step 2 for heating away from central line

Chapter 3

A semi-analytical model for metal forming by line heating

3.1 Introduction

As mentioned in Chapter 2, the process of shell forming by line heating is a coupled, non-linear, thermo-mechanical process, and is often simulated by a full three-dimensional FEM analysis. However, even when the rezoning technique is used, the computation time required is typically very long, from hours to days, and is not suitable for real-time analysis, see Yu et al. [63].

The objective of this chapter is to establish a simplified thermo-mechanical model for the line heating process, which is capable of approximately predicting the amount of angular deformation in a plate based on the plate material and the heating conditions.

3.2 Thermal model with heat loss and a distributed heat source

In the process of metal forming by line heating, residual plastic strains generated by the heating and subsequent cooling of the plate deforms the plate. Therefore, deter-

mination of temperature field is the prerequisite for predicting the final deformation of the plate. A method which can be applied to this problem is Rosenthal's solution of temperature distribution in a plate with a moving heat source [47].

Rosenthal makes three major assumptions which affect the solution of the temperature distribution. Rosenthal first assumes that the physical characteristics of the heated material, such as heat conductivity and specific heat, are independent of temperature. The second major assumption is that the speed of the moving heat source and the rate of heat input to the material are constant. When the heat source speed and the heat flux are considered constant, the third assumption of a quasi-stationary heat flow can be made. In a quasi-stationary heat flow state, while the temperature distribution is not constant with respect to a fixed coordinate system on the heated solid, it does remain constant with respect to a position on the moving heat source. This assumption is valid when the solid is long enough for a given heating condition for the quasi-stationary state to exist.

Rosenthal discusses the solutions of the heat equation for one-dimensional, two-dimensional, as well as three-dimensional cases. The solution of the temperature distribution of a moving point heat source with two-dimensional heat flow, as given by Rosenthal is presented in three ways [47]. The first solution is the most fundamental, where the linear source of constant strength through the thickness is applied without any surface heat losses. The second solution accounts for the effects of surface heat losses, but only for a thin plate where the temperature gradient across the thickness can be neglected. The third solution applies to a linear source of variable strength through the thickness but does not account for the surface heat losses. With the addition of a variable strength heat source, the temperature distribution varies through the thickness of the plate, effectively turning the two-dimensional heat flow solution into a three-dimensional solution. However, none of the solutions is suitable for the line heating process, which involves a distributed heat source and heat loss, and also temperature gradient across plate thickness.

Further improvements are made in this chapter to the third solution which make the solution suitable for the line heating process. The first modification is the incor-

poration of the effects of surface heat losses to the solution with a source of variable strength across thickness. The second adaptation is the replacement of the single point source with a distributed source of an equivalent total heat flux. This reflects the heat distribution during line heating to avoid melting the metal plate.

The rectangular coordinate system fixed on the solid is shown in Figure 3-1a. The heat source moves with speed v along the x-axis and the thickness is along the z-axis. For a coordinate system moving with the heat source, a quasi-stationary heat flow is observed. The distance from the point source along the x-axis is defined as $\xi = x - vt$ where t equals the time the source has been moving on the plate. The heat source-fixed coordinate system is shown in Figure 3-1b.

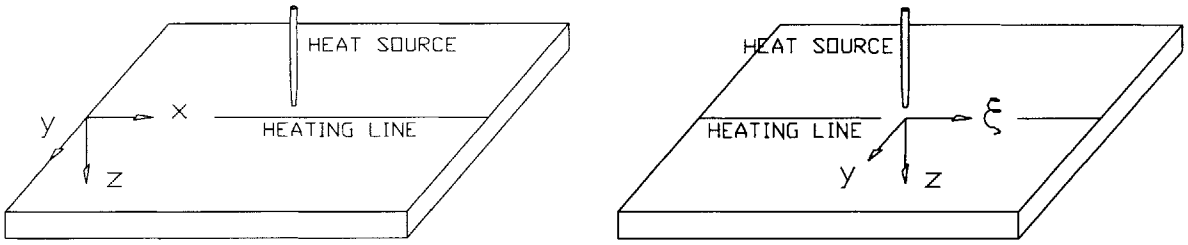

(a) (b)

Figure 3-1: (a) Plate-fixed coordinate system (b) Heat source-fixed coordinate system.

3.2.1 General solution of a quasi-stationary heat source

Following on Rosenthal [47], the partial differential equation of heat flow in a solid can be expressed in the rectangular coordinates (x, y, z) as

$$\frac{\partial^2 T}{\partial x^2} + \frac{\partial^2 T}{\partial y^2} + \frac{\partial^2 T}{\partial z^2} = 2\lambda \frac{\partial T}{\partial t} \tag{3.1}$$

where $\frac{1}{2\lambda}$ is the thermal diffusivity of the metal ($\frac{m^2}{s}$ in SI units) and

$$2\lambda = \frac{c_p \rho}{k} \tag{3.2}$$

where k is the heat conductivity of the metal ($\frac{W}{mK}$ in SI units), c_p is the specific heat ($\frac{J}{kg-K}$ in SI units), and ρ is the density ($\frac{kg}{m^3}$ in SI units).

The coordinate transformation of $\xi = x - vt$ introduced into the heat flow partial differential equation (3.1) results in

$$\frac{\partial^2 T}{\partial \xi^2} + \frac{\partial^2 T}{\partial y^2} + \frac{\partial^2 T}{\partial z^2} = -2\lambda v \frac{\partial T}{\partial \xi} + 2\lambda \frac{\partial T}{\partial t} \tag{3.3}$$

In the moving coordinate system, the quasi-stationary heat flow condition implies that the temperature remains constant with time, $\frac{\partial T}{\partial t} = 0$, yielding

$$\frac{\partial^2 T}{\partial \xi^2} + \frac{\partial^2 T}{\partial y^2} + \frac{\partial^2 T}{\partial z^2} = -2\lambda v \frac{\partial T}{\partial \xi} \tag{3.4}$$

Equation (3.4) can be simplified by putting

$$T = T_0 + e^{-\lambda v \xi} \varphi(\xi, y, z) \tag{3.5}$$

where T_0 equals the initial temperature of the plate before heating and φ is a function to be determined. When equation (3.5) is substituted into equation (3.4), the result is

$$\frac{\partial^2 \varphi}{\partial \xi^2} + \frac{\partial^2 \varphi}{\partial y^2} + \frac{\partial^2 \varphi}{\partial z^2} - (\lambda v)^2 \varphi = 0 \tag{3.6}$$

3.2.2 Variable strength source with surface heat losses

Solution methodology

The solution of a moving source with a constant strength through the thickness with surface losses can not be applied directly to the line heating problem since it is the temperature gradient through the plate thickness that causes angular deformations. The effect of temperature gradient can be accounted for by allowing for a variable

strength heat source.

If the method of separation of variables is applied to equation (3.6), the function φ can be expressed as a function of the depth and the radial distance from the source in the x-y plane, or

$$\varphi = Z(z)\,R(r) \tag{3.7}$$

Substituting equation (3.7) into equation (3.6) results in

$$R\frac{d^2Z}{dz^2} + Z\left(\frac{d^2R}{dr^2} + \frac{1}{r}\frac{dR}{dr} - (\lambda v)^2 R\right) = 0 \tag{3.8}$$

which can be rearranged to become

$$-\frac{1}{Z}\frac{d^2Z}{dz^2} = \frac{1}{R}\left(\frac{d^2R}{dr^2} + \frac{1}{r}\frac{dR}{dr} - (\lambda v)^2 R\right) = c^2 \tag{3.9}$$

where c^2 is a constant to be determined by using the boundary conditions. The two ordinary differential equations which result from equation (3.9) are

$$\frac{d^2Z}{dz^2} + c^2 Z = 0 \tag{3.10}$$

$$\frac{d^2R}{dr^2} + \frac{1}{r}\frac{dR}{dr} - \left((\lambda v)^2 + c^2\right) R = 0 \tag{3.11}$$

The solution of equation (3.11) has the form of the modified Bessel function of the second kind and zero order, where the value of c still must be determined. The value of c is found through the solution of equation (3.10). The general solution of equation (3.10) has the form

$$Z = A'\cos(cz) + B\sin(cz) \tag{3.12}$$

Taking the derivative with respect to z yields

$$\frac{dZ}{dz} = -A'c\sin(cz) + Bc\cos(cz) \tag{3.13}$$

Let us assume that the value of the heat convection coefficient for the upper surface of the plate is h_U, and the value of the heat convection coefficient for the lower surface

of the plate is h_L. When the heat loss due to radiation is also considered, the heat loss coefficients h_U and h_L are the equivalent convective heat loss coefficients. The boundary conditions at the surfaces of the plate with different heat loss coefficients are given below

$$k\frac{dT}{dz} = h_U\left(T - T_0\right) \qquad \text{at } z = 0 \tag{3.14}$$

$$k\frac{dT}{dz} = -h_L\left(T - T_0\right) \qquad \text{at } z = g \tag{3.15}$$

where k is the thermal conductivity, and g is the plate thickness. After substituting Equation (3.7) into equation (3.5), and substituting equation (3.5) into equations (3.14) and (3.15), we obtain

$$ke^{-\lambda v\xi}R\left(r\right)\frac{dZ}{dz} = h_U e^{-\lambda v\xi}Z\left(z\right)R\left(r\right) \qquad \text{at } z = 0 \tag{3.16}$$

and

$$ke^{-\lambda v\xi}R\left(r\right)\frac{dZ}{dz} = -h_L e^{-\lambda v\xi}Z\left(z\right)R\left(r\right) \qquad \text{at } z = g \tag{3.17}$$

which simplify to

$$\frac{dZ\left(0\right)}{dz} = \frac{h_U}{k}Z\left(0\right) \qquad \text{at } z = 0 \tag{3.18}$$

$$\frac{dZ(g)}{dz} = -\frac{h_L}{k}Z\left(g\right) \qquad \text{at } z = g \tag{3.19}$$

Equation (3.12) and its derivative in Equation (3.13) are evaluated at points on the upper and lower surfaces of the plate, and substituted into relations (3.18) and (3.19), respectively. On the upper surface of the plate, $z = 0$, we have

$$Bc = \frac{h_U}{k}A' \tag{3.20}$$

On the lower surface of the plate, $z = g$, we have

$$-A'c\sin\left(cg\right) + Bc\cos\left(cg\right) = -\frac{h_L}{k}\left(A'\cos\left(cg\right) + B\sin\left(cg\right)\right) \tag{3.21}$$

When the result in relation (3.20) is substituted into (3.21) and simplified, the result is

$$\tan(cg) = \frac{-(h_U + h_L)\,kc}{h_U h_L - k^2 c^2} \tag{3.22}$$

In the above equation, the $\tan(cg)$ is a periodic function, so multiple roots exist and these roots can be determined numerically. Because of the rapid decay of the right hand term in equation (3.22), the solution of the roots rapidly approaches the value of $c_n = \frac{n\pi}{g}$, which is the solution for the case when there is no surface heat loss, i.e., $\tan(cg) = 0$. It should be noted that, while $c = 0$ satisfies Equation (3.22), the root is a trivial solution and the root corresponding to A_0 term in the Fourier series representation of the heat flux distribution is the first non-zero root of c.

With the values of c_n solved for numerically, the solutions of equations (3.10) and (3.11) expressed in terms of A'_n become

$$Z_n = A'_n \left[\cos(c_n z) + \frac{h_U}{c_n k}\sin(c_n z)\right] \tag{3.23}$$

$$R_n = K_0\left[\sqrt{(\lambda v)^2 + c_n^2}\, r\right] \tag{3.24}$$

where K_0 is the modified Bessel function of the second kind and zero order. For convenience, a portion of the argument of the Bessel function in equation (3.24) is represented by Λ_n so that

$$\Lambda_n = \sqrt{(\lambda v)^2 + c_n^2} \tag{3.25}$$

When the expression for Λ_n in equation (3.25) and the solution of R_n in equation (3.24) are substituted into equation (3.7), the result is

$$\varphi_n = A'_n \left[\cos(c_n z) + \frac{h_U}{c_n k}\sin(c_n z)\right] K_0[\Lambda_n r] \tag{3.26}$$

The substitution of the result for φ into the assumed form of the temperature at a point given by Equation (3.5) yields

$$T - T_0 = e^{-\lambda v \xi} \sum_{n=0}^{N} A'_n \left[\cos(c_n z) + \frac{h_U}{c_n k}\sin(c_n z)\right] K_0[\Lambda_n r] \tag{3.27}$$

Now we are left with the determination of A'_n from the following boundary condition:

$$-\frac{\partial T}{\partial r} 2\pi r k \longrightarrow q'(z) \qquad \text{as } r \longrightarrow 0 \tag{3.28}$$

where $q'(z)$ is the heat flux per unit thickness at z ($\frac{W}{m}$ in the SI units). We assume the heat flux distribution across thickness follows a triangular distribution which decreases linearly from a maximum magnitude $q'(0)$ at the top surface to $q'(\epsilon) = 0$ at a depth of ϵ, where ϵ is a fraction of the thickness. The area of the heat distribution

$$q = \frac{1}{2} q'(0) \epsilon \tag{3.29}$$

is the total heat input per unit time (W in the SI units), which is kept as a constant. Therefore, $q'(0)$ increases when ϵ decreases. For very small ϵ compared with thickness g, the heat flux becomes close to the case of surface flux [1]. This triangular heat flux distribution can be represented by a Fourier series of the assumed form

$$q'(z) = q'(0) \sum_{n=0}^{N} A_n \left[\cos(c_n z) + \frac{h_U}{c_n k} \sin(c_n z) \right] \tag{3.30}$$

where a trigonometric series involving c_n is used for expedience of the analytical solution.

After substituting equation (3.27) and equation (3.30) into the boundary condition (3.28), We obtain the relation between the values of the A'_n and A_n:

$$A'_n = \frac{q'(0)}{2\pi k} A_n \tag{3.31}$$

The relation between the coefficients is substituted into equation (3.27) to get an expression for the temperature increase at a point in terms of the A_n coefficients of the heat flux distribution. The solution for the temperature change at a point in a plate heated with a variable strength source with different values of convective surface

heat transfer coefficients for each surface is therefore

$$T - T_0 = \frac{q'(0)}{2\pi k} e^{-\lambda v \xi} \sum_{n=0}^{N} A_n \left[\cos(c_n z) + \frac{h_U}{c_n k} \sin(c_n z) \right] K_0 [\Lambda_n r] \tag{3.32}$$

Determination of A_n coefficients

When heat losses are accounted for, the solution for c_n results in a non-orthogonal behavior of the cosine and sine terms in the summations. The integration method used for solving the values of the coefficients can therefore not be applied and the coefficients must be determined with direct use of the heat flux distribution.

The values of the A_n coefficients in the summations in the expressions for the heat flux distribution and the temperature change are found by solving a linear system of equations created by substitution of values of z into the Fourier series representation of the heat flux distribution given by

$$q'(z) = q'(0) \sum_{n=0}^{N} A_n \left[\cos(c_n z) + \frac{h_U}{c_n k} \sin(c_n z) \right] \tag{3.33}$$

When the total heat flux to the plate is kept constant, and triangular heat flux distribution is used for the method of direct substitution to solve for coefficients, the value of ϵ determines not only the value of $q'(0)$, but also the minimum number of terms required to accurately represent the heat flux distribution, and therefore the minimum number of equations required in the linear system [1]. At least two points of the heat flux distribution between $z = 0$ and $z = \epsilon$ must be represented. When ϵ is chosen so that (g/ϵ) is an integer N_0, this requirement is satisfied when $N + 1$ points are used to define the distribution, where N is a multiple of N_0. Since $N + 1$ points are used to represent the heat flux distribution accurately, $N + 1$ unknown A_n coefficients are in each equation in the linear system and, therefore, $N + 1$ equations are required for a determinate system. In our application, we chose $\epsilon = 0.01$, and $N = 200$.

Each of the $N + 1$ equations of the system is evaluated at a discrete value of z,

which when evenly distributed across the thickness is given by

$$z_n = \left(\frac{g}{N}\right) n \qquad \text{for } n = 0, 1, ...N \tag{3.34}$$

and each equation will therefore have the form

$$A_0\gamma_{m,0} + A_1\gamma_{m,1} + \cdots + A_i\gamma_{m,i} + \cdots + A_N\gamma_{m,N} = q'(z_m) \;\; m = 0, ..., N \tag{3.35}$$

where the value of $\gamma_{i,m}$ is given by

$$\gamma_{m,i} = \cos(c_i z_m) + \frac{h_U}{c_i k}\sin(c_i z_m) \tag{3.36}$$

With the values of A_n in the linear system (3.35) solved, they can be applied with their corresponding values of c_n to the summations required to evaluate the heat flux distribution and the temperature distribution within the plate.

3.2.3 Continuous heat source

In the previous sections, a point source is used in deriving the temperature field. The use of point source has the following disadvantages: (1) it does not reflect the actual practice of line heating when the heat source is diffused; (2) the temperature field has a singular point under the point source where temperature goes to infinity. A continuous heat source representation eliminates these disadvantages.

The continuous heat source is defined by the assumed truncated Gaussian distribution of the total heat flux [63], which is given by

$$q'''(r) = q'''_0 e^{-cr^2} \tag{3.37}$$

where q''' (W/m^3 in SI units) is the value of the heat flux per unit thickness and unit area on top surface at a radial distance r in the ξ-y plane from the maximum value of the heat flux q'''_0 (W/m^3 in SI units). The value of the constant c is determined by the radius r_0 of the heat flux region, where the value of the heat flux is assumed to

be five percent of the maximum value. The value of c is given as

$$c = -\frac{\ln(0.05)}{r_0^2} \tag{3.38}$$

and the maximum heat flux is therefore given as

$$q_0''' = \frac{q'(0)c}{0.95\pi} \tag{3.39}$$

where $q'(0)$ is the total heat flux per unit thickness at top surface. Equation (3.39) is obtained by equalizing the total flux per unit thickness inside the circle of radius r_0 to be $q'(0)$.

A differential element on the plate within the heat flux region at a distance r from the maximum value of the heat flux has an area $dA = rdrd\theta$. The integral of the products of the differential areas and the corresponding value of the heat flux at the radial distance r over the heat flux region is the total value of the heat flux per unit thickness. On the heated surface of the plate, a differential amount of heat flux is given as

$$dq' = q'''(r)rdrd\theta \tag{3.40}$$

With reference to equation (3.32), the expression of the temperature change at a point, with the application of equation (3.40), yields

$$T - T_0 = \int_0^{r_0}\int_0^{2\pi} \frac{q'''(r)}{2\pi k} e^{-\lambda v(\xi - r\cos\theta)} \sum_{n=0}^{N} A_n \left[\cos(c_n z) + \frac{h_U}{c_n k}\sin(c_n z)\right] K_0\left[\Lambda_n \sqrt{(\xi - r\cos\theta)^2 + (y - r\sin\theta)^2}\right] rdrd\theta \tag{3.41}$$

which can be computed numerically using Gaussian quadrature [11].

Elimination of singularities

When we evaluate equation (3.41) numerically using Gaussian quadrature, for all points outside the heat flux region, the modified Bessel function has no singularity. However, for points inside the heat flux region and are close to the Gaussian integra-

tion points, singularity in modified Bessel function results in very high temperature there.

The singularities in temperature computation can be removed by using a coordinate transformation. We perform numerical integration using the polar coordinate system (R, γ) centering at the point of interest instead of the polar coordinate system (r, θ) whose origin is at the center of the heat flux region, see Figure 3-2.

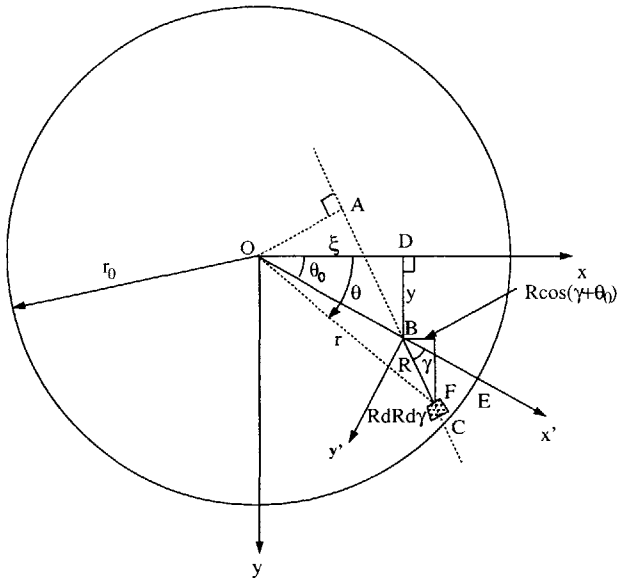

Figure 3-2: Coordinate transformation

Let O be the center of the heat flux region, and B be the point whose temperature is to be computed. Then we have

$$|OD| = |\xi|, \quad |BD| = |y| \tag{3.42}$$

$$|OB| = \sqrt{|OD|^2 + |BD|^2} = \sqrt{\xi^2 + y^2} \tag{3.43}$$

and

$$\theta_0 = \begin{cases} \tan^{-1}\frac{y}{\xi} & \text{if } \xi > 0 \\ \pi + \tan^{-1}\frac{y}{\xi} & \text{if } \xi < 0 \\ \frac{\pi}{2} & \text{if } \xi = 0 \text{ and } y > 0 \\ -\frac{\pi}{2} & \text{if } \xi = 0 \text{ and } y < 0 \end{cases} \tag{3.44}$$

We assume the radius of the heat flux region is r_0, and consider the intersection of a

ray of an angle $\gamma \in (0, \frac{\pi}{2})$ with the boundary of the heat flux region. We have

$$|AB| = |OB||\cos\gamma| = \sqrt{\xi^2 + y^2}|\cos\gamma| \tag{3.45}$$

$$|OA| = |OB||\sin\gamma| = \sqrt{\xi^2 + y^2}|\sin\gamma| \tag{3.46}$$

$$|AC| = \sqrt{r_0^2 - |OA|^2} = \sqrt{r_0^2 - (\xi^2 + y^2)\sin^2\gamma} \tag{3.47}$$

Therefore,

$$R_0(\gamma) = |BC| = |AC| - |AB| = \sqrt{r_0^2 - (\xi^2 + y^2)\sin^2\gamma} - \sqrt{\xi^2 + y^2}\cos\gamma \tag{3.48}$$

It can be verified that equation (3.48) also apply when $\gamma \notin (0, \frac{\pi}{2})$.

The temperature change at point B due to the differential heat input at the differential area $dA = RdRd\gamma$ located at point F is

$$dT = \frac{q'''(r)}{2\pi k} e^{-\lambda v R\cos(\gamma+\theta_0)} \sum_{n=0}^{N} A_n \left[\cos(c_n z) + \frac{h_U}{c_n k}\sin(c_n z)\right] K_0\left[\Lambda_n R\right] RdRd\gamma \tag{3.49}$$

where R is the distance between points F and B, and

$$r = |OF| = \sqrt{|OB|^2 + |BF|^2 + 2|OB||BF|\cos\gamma}$$

$$= \sqrt{\xi^2 + y^2 + R^2 + 2R\sqrt{\xi^2 + y^2}\cos\gamma} \tag{3.50}$$

$$q'''(r) = q_0 e^{-cr^2} = q_0 e^{-c(\xi^2+y^2+R^2+2R\sqrt{\xi^2+y^2}\cos\gamma)} \tag{3.51}$$

Therefore, after integrating the temperature change due to all the differential heat flux within the circle in Figure 3-2, we obtain the temperature increase at point B located inside the heat flux region as

$$T - T_0 = \int_0^{2\pi}\int_0^{\sqrt{r_0^2-(\xi^2+y^2)\sin^2\gamma}-\sqrt{\xi^2+y^2}\cos\gamma} \frac{q_0 e^{-c(\xi^2+y^2+R^2+2R\sqrt{\xi^2+y^2}\cos\gamma)}}{2\pi k} e^{-\lambda v R\cos(\gamma+\theta_0)} \sum_{n=0}^{N} A_n \left[\cos(c_n z) + \frac{h_U}{c_n k}\sin(c_n z)\right] K_0[\Lambda_n R] RdRd\gamma \tag{3.52}$$

Since $K_0[\Lambda_n R]R$ is finite when $R \to 0$, equation (3.52) can be evaluated numerically by using Gaussian quadrature with no singularity.

Therefore, when equation (3.41) is used for computation of the temperature at points located outside the heat flux region, and equation (3.52) is used for computation of the temperature at points located inside the heat flux region, the temperature field can be evaluated without any singularity.

3.2.4 Discussions of the thermal model

From the derivation of the thermal model, we can see that the effects of heat loss on temperature field expressed in equation (3.27) lie in (1) difference between the solution c of equation (3.22) and $\frac{n\pi}{g}$, which is the solution for the case of no surface heat loss, and (2) the term with h_U in equation (3.27). Equation (3.22) can be rewritten as

$$\tan(cg) = \frac{\frac{h_U+h_L}{kc}}{1-\frac{h_U h_L}{k^2c^2}} \tag{3.53}$$

Therefore, as a first approximation, the difference between c_n and $\frac{n\pi}{g}$ depends on

$$\frac{h_U+h_L}{kc} \approx \frac{(h_U+h_L)g}{n\pi k} \tag{3.54}$$

$$\frac{h_U h_L}{k^2c^2} \approx \frac{h_U h_L g^2}{n^2\pi^2 k^2} \tag{3.55}$$

The term with h_U in equation (3.27) has the same order of magnitude as the right hand side of equation (3.54).

It should be noted that when heat loss due to radiation is taken into account, h_U, h_L become the equivalent heat loss coefficients. For the forming process of a mild steel plate of the size 30.48 cm $\times$ 30.48 cm $\times$ 2.54 cm, under an average temperature of 500^oC, the equivalent heat loss coefficient due to radiation $h = 5.67 \times 10^{-8}\varepsilon(T_s^3 - T_a^3) = 24.73 W m^{-2} K^{-1}$ is of the same order of magnitude as the convective heat loss coefficients. Since

$$\frac{(h_U+h_L)g}{\pi k} = 3.078 \times 10^{-3} \tag{3.56}$$

$$\frac{h_U h_L g^2}{\pi^2 k^2} = 2.105 \times 10^{-6}, \tag{3.57}$$

these terms are negligible, and the temperature field with heat loss does not differ much from that without heat loss.

At high temperature, the equivalent heat loss coefficient due to radiation increases rapidly. For example, $h = 115.5 W m^{-2} K^{-1}$ at $T_s = 1000^o C$. Therefore, the effects of heat loss on temperature field become more important at high temperatures. Tungsten typically has a service temperature around $2000^o C$. If a tungsten plate is bent at high temperature, then heat loss will be significant.

3.3 Simplified mechanical model

3.3.1 Assumptions

A simplified mechanical model was first proposed by Jang et al. [22] with the following assumptions:

(1) The elasto-plastic process is concentrated on a circular disk under the heat source and that the plate is infinite in two dimensions. Also, the diameter of the disk changes through the thickness of the plate, resulting in elliptical isothermal boundaries in the cross-section of the plate perpendicular to the direction of the heating line.

(2) The thermal elasto-plastic process occurs within the small, circular region axisymmetrically and the remaining elastic region resists the expansion and contraction of the circular plastic region. The resistance of the elastic region on the plastic zone is modeled as a set of surrounding springs which is illustrated in Figure 3-3(a). The spring constant K is evaluated by deriving the radial displacement of a circular hole of an infinite plate subjected to an inner uniform pressure p, as shown in Figure 3-3(b).

(3) The temperature increasing process, which results in thermal expansion, can be thought of as a mechanical plastic loading in the plastic region and the tem-

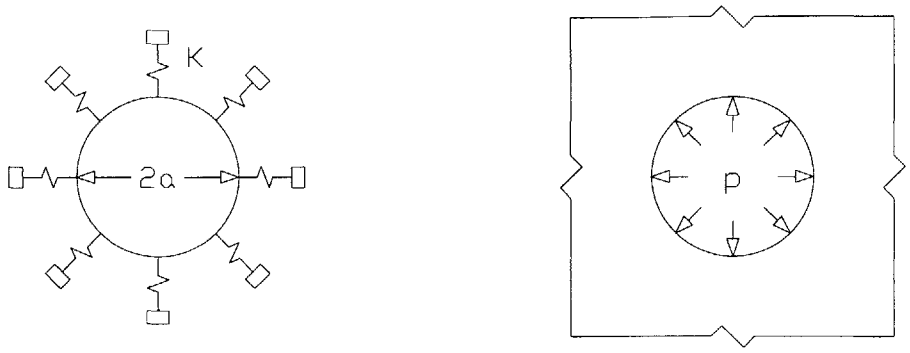

(a) (b)

Figure 3-3: (a) Model of plastic region (b) Model of elastic region.

perature decreasing process is a mechanical plastic unloading. This plastic unloading process is the cause of the residual strains which ultimately result in the plate angular deformation.

(4) The final angular deformation results from the integration of deformation due to the residual strain in each disk. The bounds of integration are defined by the region of inherent strain produced during heating, which is assumed to have an elliptical distribution in the plane of the plate perpendicular to the heating path. The assumed elliptical distribution is based on experimental results and Rosenthal's solution [48][47].

3.3.2 Plastic strain

Under the previous assumptions, during the temperature increasing process, the central circular area goes to plastic. After the plate cools down, the residual plastic strain in the radial direction of the circular plastic region is [22]

$$\epsilon_{rr}^{*} = -\alpha T_c + \sigma_{yD}\left(\frac{1}{aK} + \frac{1-\nu_D}{E_D}\right) \tag{3.58}$$

where α is the thermal coefficient of the disk; T_c is the critical temperature of the plate material; σ_{yD} is the yield stress of the disk; a is the radius of the disk; ν_D is the

Poisson's ratio of the disk; E_D is the Young's modulus of the disk, and

$$K = \frac{p}{u_p} = \frac{E}{a\,(1+\nu)} \tag{3.59}$$

is the spring constant of the surrounding area. In equation (3.59), u_p is the increment of the radius of the circle in Figure 3-3(b) due to pressure p; E and ν are the Young's modulus and Poisson's ratio of the elastic region respectively. It can be seen from equation (3.58) that Jang et al. [22] treats the temperatures inside the plastic region to be all T_c, which tends to underpredict the plastic strain. We make a reasonable modification. We use the average of the critical temperature and the maximum temperature inside the plastic region to compute the residual strain, i.e.,

$$\epsilon^*_{rr} = -\alpha T_a + \sigma_{yD}\left(\frac{1}{aK} + \frac{1-\nu_D}{E_D}\right) \tag{3.60}$$

where $T_a = (T_c + T_{max})/2$, and T_{max} is the maximum temperature inside the plastic region. T_a is an approximation of the average temperature inside the plastic region.

3.3.3 Inherent strain zone dimensions

The inherent strain zone is defined as the maximum region where peak temperature is equal to or greater than the critical temperature where material strength becomes minimal and is dependent on the heating conditions.

On the plane perpendicular to the direction of the heat source, Jang's model assumes a half-elliptical isothermal, and therefore, a plastic region, as illustrated in Figure 3-4 [22]. This idealization is based on temperature distributions determined analytically by Rosenthal's solution for an infinite plate with finite thickness and a point heat source moving with constant speed without any heat loss [47].

The isothermal region relevant to the calculation of the deformation due to heating is the region which is bounded by the critical temperature and therefore bounds the plastic region. The dimensions of the inherent strain zone are set by the maximum breadth b, and depth d, of the region as illustrated in Figure 3-4. The assumed

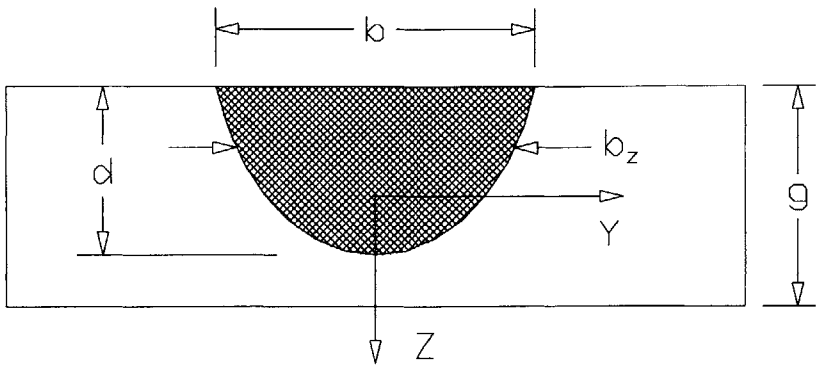

Figure 3-4: Assumed elliptical distribution of critical isothermal region and corresponding dimensions. Adapted from [22]

elliptical distribution is given by

$$\frac{Y^2}{\left(\frac{b}{2}\right)^2} + \frac{\left(Z+\frac{g}{2}\right)^2}{d^2} = 1 \tag{3.61}$$

where the X-Y plane is defined as the mid-plane of the plate with the Z-axis directed downward at the middle of the breadth of the inherent strain zone. The thickness of the plate is denoted by the variable g.

The width of the inherent strain zone at any depth is required in the solution of the angular deformation due to heating and is found by rearranging equation (3.61) to yield

$$b_Z = b\sqrt{1 - \frac{1}{d^2}\left(Z+\frac{g}{2}\right)^2} \tag{3.62}$$

where b_Z is the width of inherent strain zone at any location through the thickness.

As mentioned previously, the dimensions and shape of the inherent strain zone are functions of the heating conditions, such as heat flux and heating source speed. The relations between inherent strain zone size and heating parameters used by Jang et al. is through an assumed linear relationship by constants determined in welding experiments [22] which is hard to verify. A more reasonable method for determining the size of the inherent strain is to use the information of isothermal lines computed from the thermal model presented in Section 3.2.

The maximum breadth and depth of the inherent strain zone are determined nu-

merically by successively integrating the initial value problem for a system of coupled non-linear differential equations using a fourth-order Runge-Kutta method. Since the inherent strain zone is defined as the region which had reached a critical temperature, solving for the maximum dimensions of an isothermal region of the critical temperature is equivalent to solving for the maximum dimensions of the inherent strain zone.

3.3.4 Maximum breadth

Isothermal contour lines on the ξ-y plane satisfy the relation

$$T(\xi, y) = constant \tag{3.63}$$

where $T(\xi, y)$ is the temperature given by equation (3.41) or equation (3.52) at a fixed value of z. The maximum breadth of the inherent strain zone occurs on the upper surface of the plate, where $z = 0$. The isotherm in the ξ-y plane on the plate can be expressed as a parametric curve defined by

$$\mathbf{r}(s) = \mathbf{r}(\xi(s), y(s)) \tag{3.64}$$

Differentiating the expression for temperature along an isotherm given by expression (3.63) with respect to arc length s along the contour line yields

$$\frac{\partial T}{\partial \xi}\frac{d\xi}{ds} + \frac{\partial T}{\partial y}\frac{dy}{ds} = 0 \tag{3.65}$$

where the derivatives of the positions with respect to the arc length of the isotherm together give the direction of the contour line. The solutions of equation (3.65) are

$$\frac{d\xi}{ds} = \alpha\frac{\partial T}{\partial y} \tag{3.66}$$

$$\frac{dy}{ds} = -\alpha\frac{\partial T}{\partial \xi} \tag{3.67}$$

α is an arbitrary, non-zero constant which is selected to satisfy the arc length parametrization given by

$$ds^2 = d\xi^2 + dy^2 = \alpha^2 \left[\left(\frac{\partial T}{\partial \xi} \right)^2 + \left(\frac{\partial T}{\partial y} \right)^2 \right] ds^2 \tag{3.68}$$

which results in

$$\alpha = \pm \frac{1}{\sqrt{\left(\frac{\partial T}{\partial \xi} \right)^2 + \left(\frac{\partial T}{\partial y} \right)^2}} \tag{3.69}$$

The substitution of the solution for the value of α, using the positive solution, into equations (3.66) and (3.67) yields

$$\frac{d\xi}{ds} = \frac{1}{\sqrt{\left(\frac{\partial T}{\partial \xi} \right)^2 + \left(\frac{\partial T}{\partial y} \right)^2}} \frac{\partial T}{\partial y} \tag{3.70}$$

$$\frac{dy}{ds} = \frac{-1}{\sqrt{\left(\frac{\partial T}{\partial \xi} \right)^2 + \left(\frac{\partial T}{\partial y} \right)^2}} \frac{\partial T}{\partial \xi} \tag{3.71}$$

where $\frac{\partial T}{\partial \xi}$ and $\frac{\partial T}{\partial y}$ on the upper surface of the plate where $z = 0$ can be obtained by taking derivatives of equation (3.41) or equation (3.52).

Points on an isothermal contour line are computed successively by integrating equations (3.70) and (3.71) using the Runge-Kutta method [11]. The initial value required for the integration process is taken to be the point on the isotherm of the critical temperature which lies along the ξ-axis, or $y = 0$. This point is found by the method of bisection. Using the initial point on the isotherm, the Runge-Kutta method computes the position of another point along the isotherm, where the distance of the iterated point from the initial point is controlled by the value of an incremental step size, h.

3.3.5 Maximum depth

The maximum depth of the inherent strain zone is found using the same method as that used to find the maximum breadth, except the isothermal contour line lies in

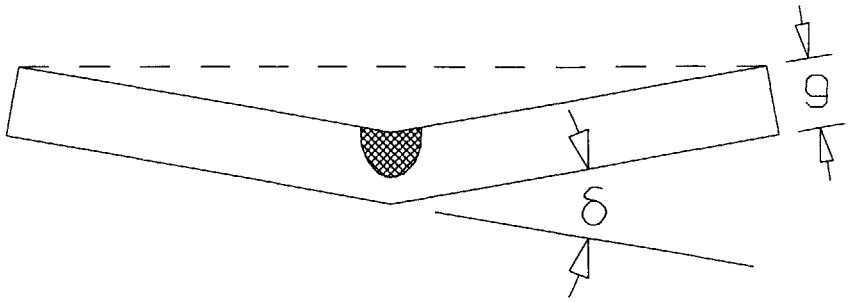

Figure 3-5: Angular deformation δ in the y-z plane. Adapted from [22]

the ξ-z plane and all expressions are in terms of ξ and z, i.e. we solve the equation

$$T(\xi, z) = constant \tag{3.72}$$

by using the fourth order Runge-Kutta method [11].

3.3.6 Maximum depth in an overheated condition

The depth of the critical isotherm will be the thickness of the plate if the heat input is high enough. For this case, in order to characterize the elliptical isotherm of the critical temperature in Figure 3-4 and given by equation (3.62) for the estimation of plate deflection, the breadth of the critical isotherm on the bottom surface needs to be evaluated. The breadth at $z = g$ can be solved using the same expressions for the Runge-Kutta method used to determine the breadth on the upper surface of the plate, except with $z = g$ instead of $z = 0$ in the equation of temperature field.

3.3.7 Angular deformation

The assumption made in the simplified mechanical model presented by Jang et al. [22] that a unit strip of plate behaves like a beam is still applicable when values of the maximum breadth and depth of the inherent strain zone are used directly in the estimation of plate deformation.

It can be shown that the angular deformation in Figure (3-5) can be expressed as

[22]

$$\delta = \frac{-12\left(1-\nu^2\right)\epsilon_{rr}^*}{g^3}\int_\alpha^\beta b_Z Z dZ \tag{3.73}$$

After substituting Equation (3.62) into Equation (3.73), the actual value of the angular deformation is obtained by simply evaluating the integral in equation (3.73). Depending on the heating conditions however, the solution of the integral can be one of two forms.

With a low heat input, the depth of the inherent strain zone is less than the thickness of the plate and the bounds of integration are set by the maximum depth of the inherent strain zone. The limits of integration are from $\alpha = -\frac{g}{2}$ to $\beta = d - \frac{g}{2}$, using a coordinate system shown in Figure 3-4. With these bounds on the integral, the solution becomes

$$\delta = \frac{-2\left(1-\nu^2\right)}{g^3}\epsilon_{rr}^* bd\left[2d - \frac{3\pi}{4}g\right] \tag{3.74}$$

At a certain value of heat input, the depth of the inherent strain zone equals the thickness of the plate. For this condition, and all conditions with higher values of heat input where the depth of the assumed elliptical inherent strain zone projects beyond the plate thickness, the limits of integration for Equation (3.74) become $\alpha = -\frac{g}{2}$ to $\beta = \frac{g}{2}$, or across the entire thickness of the plate and the solution becomes

$$\delta = \frac{-2\left(1-\nu^2\right)}{g^3}\epsilon_{rr}^* bd\left[-2d\left(\left(1-\left(\frac{g}{d}\right)^2\right)^{\frac{3}{2}}-1\right) - \frac{3g}{2}\left(\frac{g}{d}\sqrt{1-\left(\frac{g}{d}\right)^2}+\sin^{-1}\frac{g}{d}\right)\right] \tag{3.75}$$

3.3.8 Shrinkage forces

The strains which result in the angular deformation of a plate from line heating can also be expressed by shrinkage forces and bending moments shown in Figure 3-6 [22]. These forces and moments are due to shrinkage of the inherent strain zone upon cooling and can be determined from integration of inherent strains. Since the inherent strain zone is assumed to have an elliptical distribution, the effects of the strains are represented by both a transverse moment and shrinkage force, which act

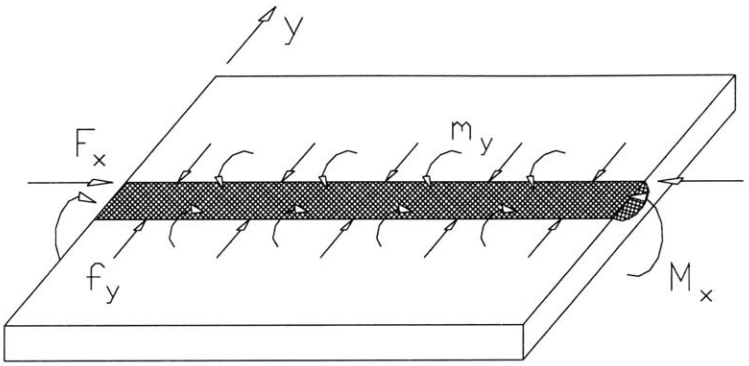

Figure 3-6: Shrinkage forces and moments due to line heating. Adapted from [22].

perpendicular to the heating line. Similarly, the strains also create an longitudinal bending moment and shrinkage force which act parallel to the direction of the heating line, with much smaller magnitude that the transverse moment and shrinkage force.

Transverse shrinkage forces

Transverse bending moments and shrinkage forces along the heating line result from integration of inherent strains with respect to a unit longitudinal section [22]. The transverse bending moment per unit length m_y ($\frac{Nm}{m}$ in SI units) is given by

$$m_y = \int_{-\frac{g}{2}}^{d-\frac{g}{2}} E\epsilon^*_{rr} \frac{b_z}{b|_{z=0}} z dz = E\epsilon^*_{rr} d \left[\frac{d}{3} - \frac{g\pi}{8}\right] \tag{3.76}$$

where the expression for b_z from equation 3.62 is used. The transverse shrinkage force per unit length f_y ($\frac{N}{m}$ in SI units) is given by

$$f_y = \int_{-\frac{g}{2}}^{d-\frac{g}{2}} E\epsilon^*_{rr} \frac{b_z}{b|_{z=0}} dz = E\epsilon^*_{rr} \frac{\pi}{4} d \tag{3.77}$$

when the depth of the inherent strain zone is less than the thickness of the plate. Like the solution for the angular deformation however, two solutions of both the transverse bending moment and shrinkage force exist. Therefore, when the depth of the inherent strain zone exceeds the thickness, the bounds of integration change to include the entire plate thickness and the solution of the transverse bending moment

per unit length becomes

$$m_y = E\epsilon_{rr}^* d\left[-\frac{d}{3}\left(\left(1-\left(\frac{g}{d}\right)^2\right)^{\frac{3}{2}}-1\right)-\frac{g}{4}\left(\frac{g}{d}\sqrt{1-\left(\frac{g}{d}\right)^2}+\sin^{-1}\frac{g}{d}\right)\right] \tag{3.78}$$

and the transverse shrinkage force becomes

$$f_y = \int_{-\frac{g}{2}}^{\frac{g}{2}} E\epsilon_{rr}^* \frac{b_z}{b|_{z=0}} dz = E\epsilon_{rr}^* d\left[\frac{g}{2d}\sqrt{1-\left(\frac{g}{d}\right)^2}+\frac{1}{2}\sin^{-1}\frac{g}{d}\right] \tag{3.79}$$

Because the transverse bending moment and shrinkage forces are a result of the inherent strains, they are assumed to act along the edge of the inherent strain zone.

Longitudinal shrinkage forces

The longitudinal bending moments and shrinkage forces which act along the heating line result from the integration of inherent strains with respect to a unit transverse section perpendicular to the heating line [22].

When the depth of the inherent strain zone is less than the plate thickness, the longitudinal bending moment (Nm in SI units) is expressed as

$$M_x = \int_{-\frac{g}{2}}^{d-\frac{g}{2}} E\left(1-\nu\right)\epsilon_{rr}^* b_z z dz = E\left(1-\nu\right)\epsilon_{rr}^* bd\left(\frac{d}{3}-\frac{g\pi}{8}\right) \tag{3.80}$$

and the longitudinal shrinkage force (N in SI units) is given by

$$F_x = \int_{-\frac{g}{2}}^{d-\frac{g}{2}} E\left(1-\nu\right)\epsilon_{rr}^* b_z dz = E\left(1-\nu\right)\epsilon_{rr}^* \frac{\pi}{4} bd \tag{3.81}$$

When the depth of the inherent strain zone is greater than the plate thickness, the longitudinal bending moment becomes

$$M_x = \int_{-\frac{g}{2}}^{d-\frac{g}{2}} E\left(1-\nu\right)\epsilon_{rr}^* b_z z dz = E\left(1-\nu\right)\epsilon_{rr}^* bd\left[-\frac{d}{3}\left(\left(1-\left(\frac{g}{d}\right)^2\right)^{\frac{3}{2}}-1\right)\right.$$
$$\left.-\frac{g}{4}\left(\frac{g}{d}\sqrt{1-\left(\frac{g}{d}\right)^2}+\sin^{-1}\frac{g}{d}\right)\right] \tag{3.82}$$

and the longitudinal shrinkage force becomes

$$F_x = \int_{-\frac{g}{2}}^{\frac{g}{2}} E\left(1-\nu\right)\epsilon_{rr}^{*} b_z dz = E\left(1-\nu\right)\epsilon_{rr}^{*}\frac{bd}{2}\left[\frac{g}{d}\sqrt{1-\left(\frac{g}{d}\right)^2}+\sin^{-1}\frac{g}{d}\right] \tag{3.83}$$

Within the inherent strain zone, the longitudinal bending moments and shrinkage forces cancel. Therefore, the moments and forces only act at the ends of the plate and are the total reaction. Because the longitudinal shrinkage forces cancel within the inherent strain zone and because they act perpendicularly to the heating path and are therefore affected by Poisson's ratio, the total relative longitudinal forces are much lower than the transverse forces. Therefore, while angular deformation occurs in both the transverse and longitudinal directions, the transverse deformation is dominant.

3.4 Results and analysis

Line heating experiments were conducted to verify the thermal model and the simplified mechanical model. All the laser experiments were performed at the Applied Research Laboratory of Pennsylvania State University. A 3.0 kW Nd:YAG laser operating in the continuous-wave mode was used as the heat source [62]. Experiments with an oxy-acetylene heating torch were conducted at the MIT Department of Ocean Engineering Fabrication Laboratory.

3.4.1 Results of laser line heating on Inconel plates

The first experiment on Inconel plates can be used to verify the thermal model. The laser output power is 2.6 kW; its spot size (diameter) is 22 mm, and the traverse velocity is 20 cm/min. The square plates are 304.8 mm by 304.8 mm with thickness of 6.35 mm. Plates are heated along the centerline of the top surface, and temperature is measured at points on the bottom surface which are 0 mm, 12.7 mm, 25.4 mm. 50.8 mm, 76.2 mm from the centerline, respectively, see Figure 3-7.

According to measurements by researchers at the Applied Research Laboratory of Pennsylvania State University [62], the YAG laser beam displays a Gaussian dis-

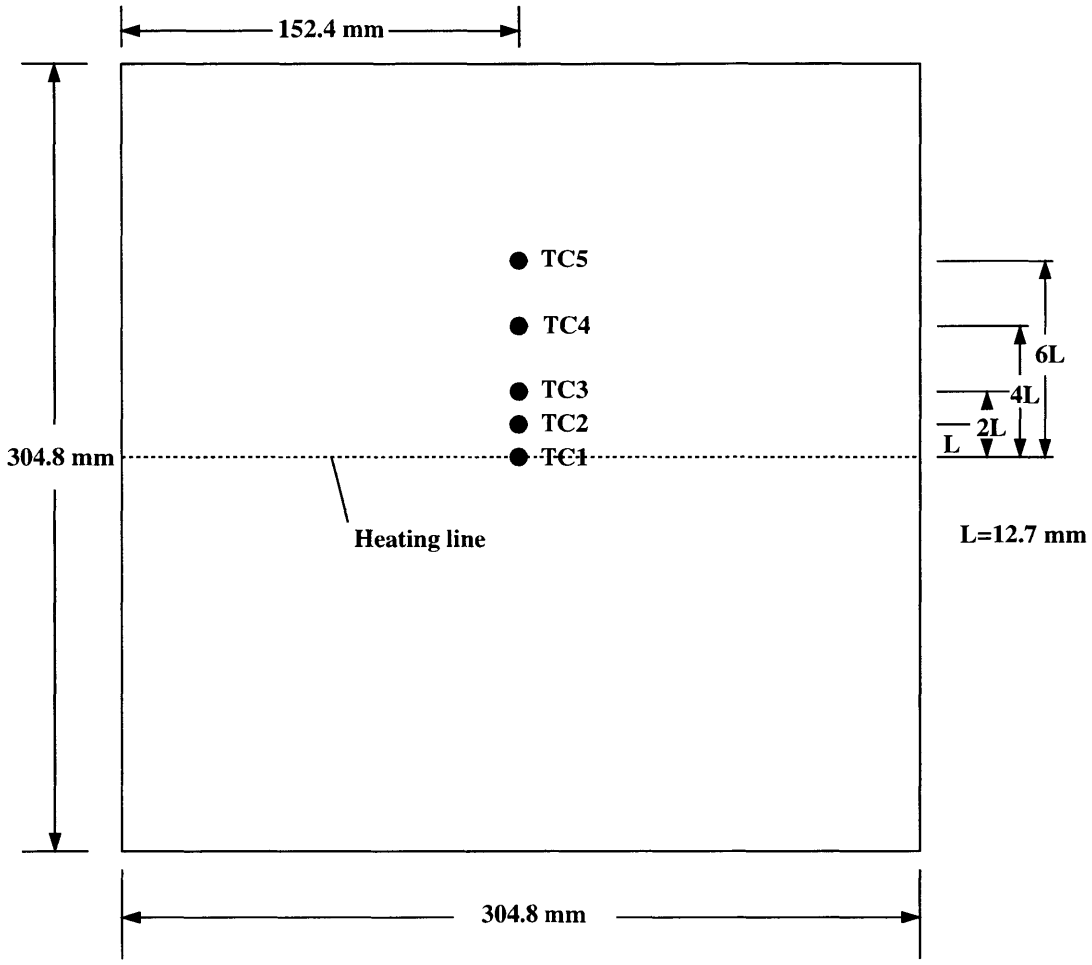

Figure 3-7: Locations of thermocouples in experiment

tribution with an annular lobe. Detail description of the laser profile is presented in Chapter 2. Here we model the heat input of the whole laser beam as a truncated Gaussian distribution. The heat absorption rate is computed by minimizing the sum of the squares of the difference between measured and computed peak temperatures at the thermocouple locations 1, 2, 3. The temperature data from the thermocouples 4 and 5 are not used since their peak temperature appears after the heating process, when the assumption of quasi-stationary state of the temperature field no longer holds. If the specimen is long enough, the peak temperatures at thermocouple locations 4 and 5 will appear during the heating process. Both the heat conductivity and specific heat of the Inconel plates increase with temperature.

At 21^oC, $k = 9.8Wm^{-1}K^{-1}$, $c_p = 410J(kg)^{-1}K^{-1}$.

At 538^oC, $k = 17.5Wm^{-1}K^{-1}$, $c_p = 535J(kg)^{-1}K^{-1}$.

At 871^oC, $k = 22.8Wm^{-1}K^{-1}$, $c_p = 620J(kg)^{-1}K^{-1}$ [10].

The change of thermal diffusivity is within 50% from 21^oC to 871^oC. Here the data at 538^oC is used. In numerical integration by using Gaussian quadrature, 25 integration points are used in both r and θ directions for equation (3.41), and in both R and γ directions for equation (3.52). We need 25 integration points to achieve convergence because of the complexity of the integration function in both equation (3.41) and equation (3.52). The computed heat absorption rate is 0.81751. The temperatures from experiment, from Rothenthal's 3D model, from 3D FEM model, and those from the semi-analytical thermal model at thermocouple locations 1, 2, 3 are shown in Figures 3-8 to 3-10. For 3D FEM simulation, temperature-dependent material properties, and the heat flux given by equation 2.10 is used.

It can be seen from Figures 3-8 to 3-10 that Rothenthal's 3D model tends to overpredict the temperature near the heating line, since a concentrated heat source is used. The semi-analytical thermal model predicts temperature well, especially for the points near the heating line. For points far away from the heating line, the error will increase because of the effect of finite width of the plate. Since the plastic deformation is confined in a narrow region near the heating line, the error in temperature far away from the heating line is not expected to have a large effect on prediction of the bending

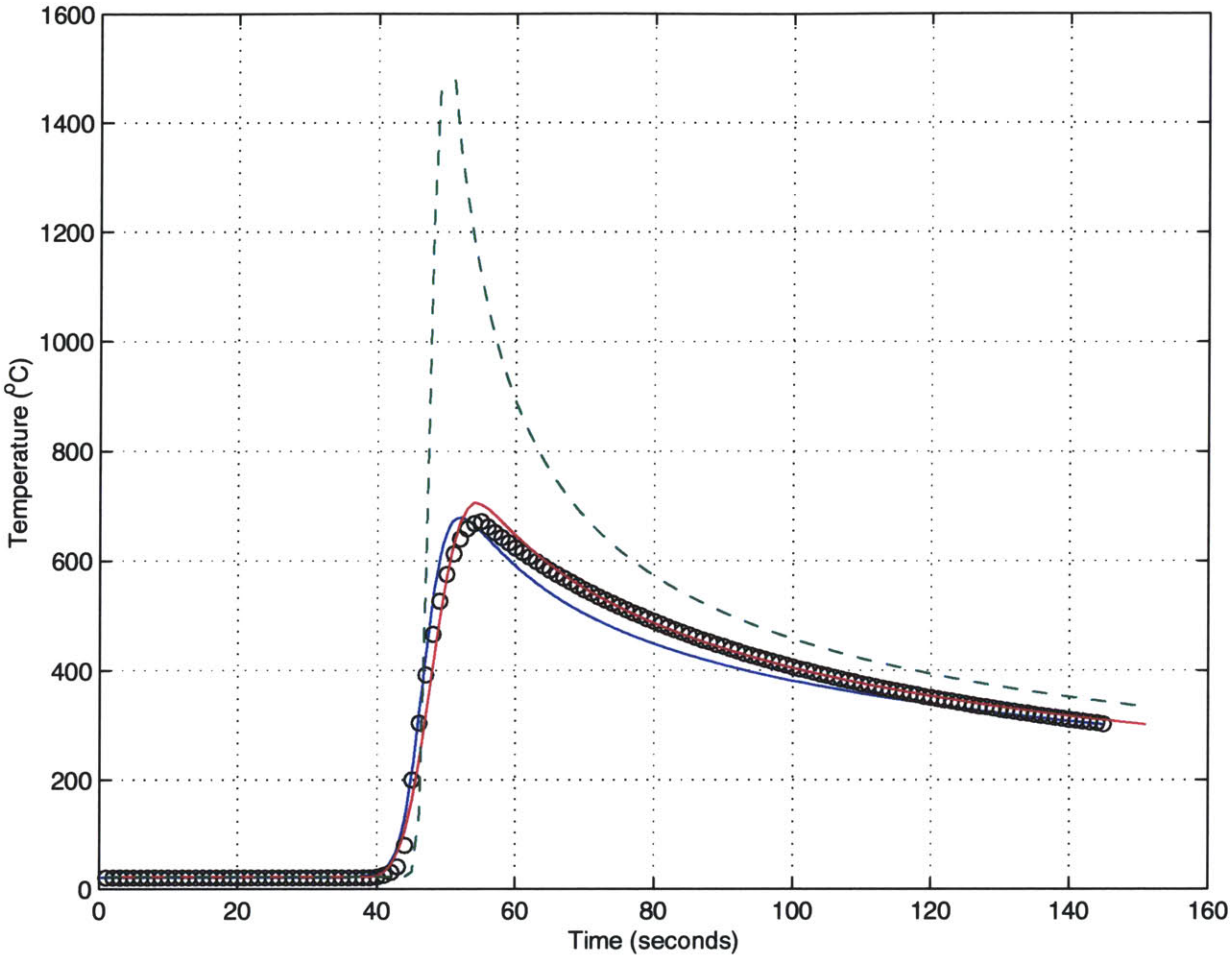

Figure 3-8: Temperature variations at thermo-couple location 1 (solid red line for the temperatures from the thermal model, dashed green line for the temperatures from Rothenthal's 3D model, circles for the temperature from measurement, and solid blue line for the temperatures from the FEM model)

angle. It can also be seen that the complex heat flux model given by equation (2.10) is not better than the simple truncated Gaussian distribution used for the simplified model. The error of the FEM results may also show that the mesh used is not dense enough.

Figures 3-11 and 3-12 show the isothermal lines on the top surface ($z = 0$) and on the cross section ($y = 0$) respectively. Figure 3-13 shows the isothermal lines on the front cross section ($\xi = -0.008$).

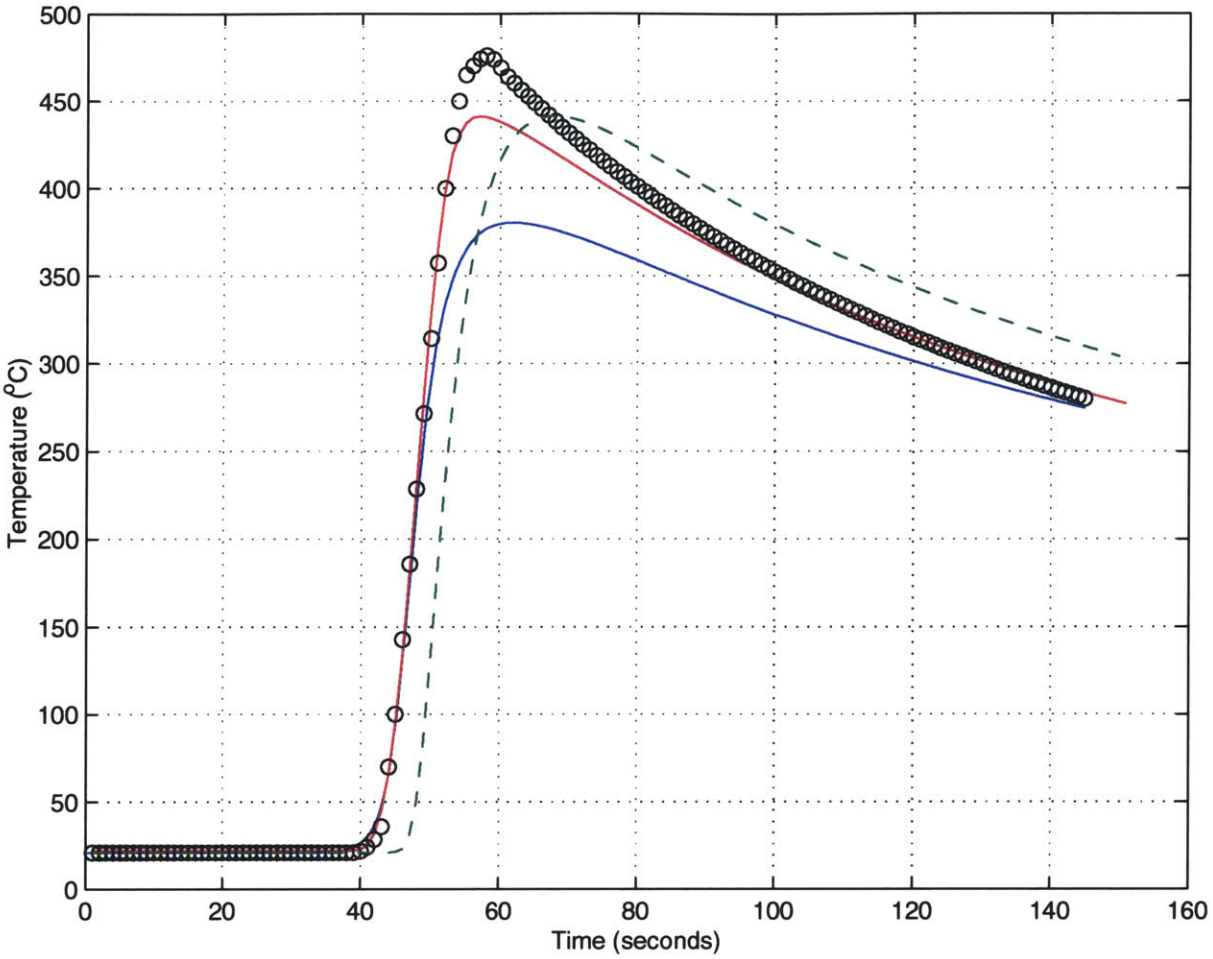

Figure 3-9: Temperature variations at thermo-couple location 2 (solid red line for the temperatures from the thermal model, dashed green line for the temperatures from Rothenthal's 3D model, circles for the temperature from measurement, and solid blue line for the temperatures from the FEM model)

3.4.2 Results of laser line heating on mild steel plates

A series of experiments were performed on $30.48cm \times 30.48cm \times 2.54cm$ mild steel plates with various spot size and heat source moving velocity. The laser has the same output power. Repeated heating was performed, but here we only use the results from the first heating to verify our mechanical model. The heat input of the whole laser beam is modeled as a truncated Gaussian distribution, with diameter twice the spot size. The temperature distribution is computed by our thermal model, then the breadth and depth of the plastic region are computed by the method presented in Section 3.3. Critical temperature is chosen to be 500^oC. For mild steel, Young's

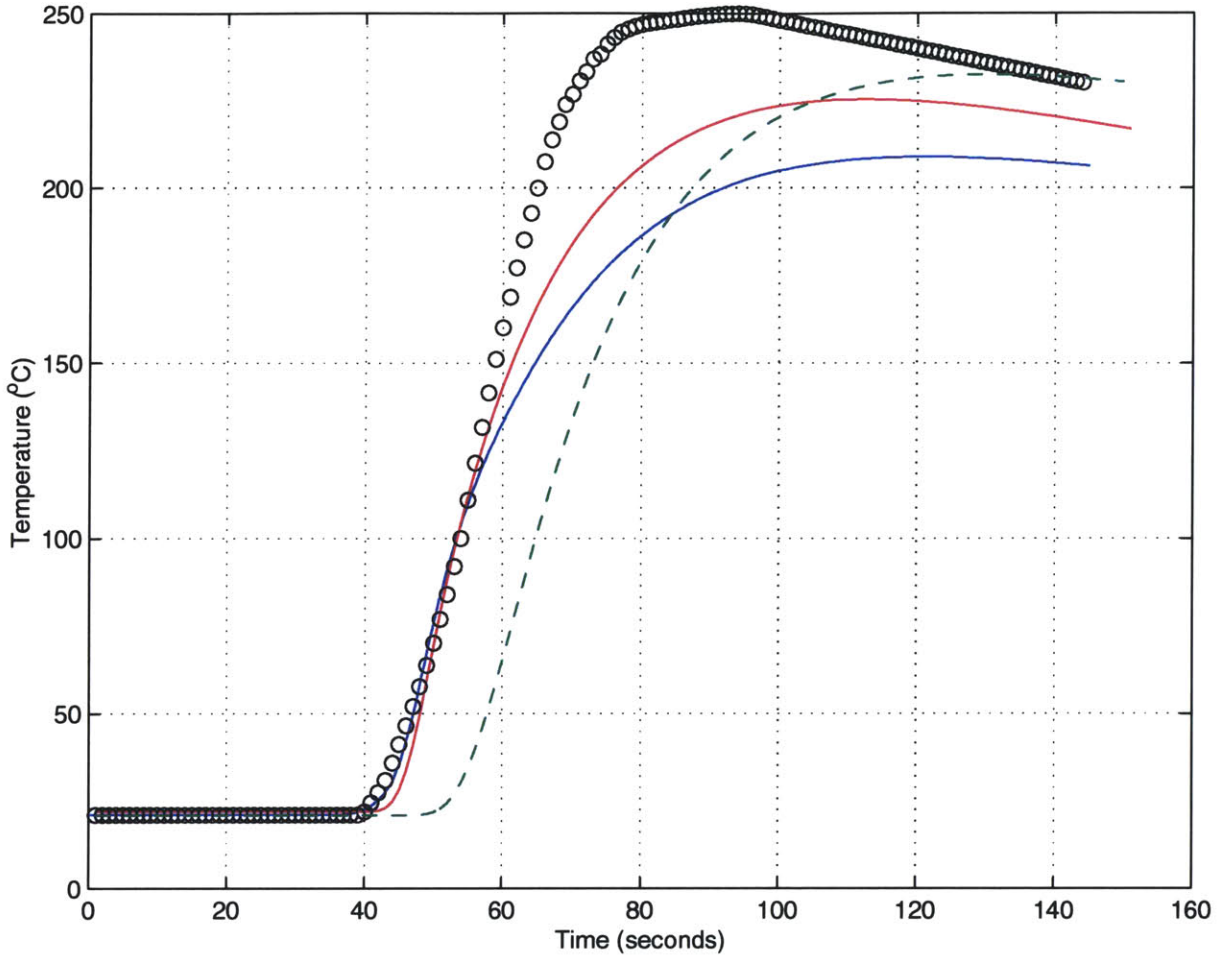

Figure 3-10: Temperature variations at thermo-couple location 3 (solid red line for the temperatures from the thermal model, dashed green line for the temperatures from Rothenthal's 3D model, circles for the temperature from measurement, and solid blue line for the temperatures from the FEM model)

modulus and yield stress become very small at a temperature above 725^oC [20] [7]. Due to the restraint of the surrounding material during line heating process, not only the area with temperature above 725^oC will become plastic, the region with lower temperature is also expected to become plastic. Thus we choose a critical temperature of 500^oC. The material properties of mild steel are also chosen to be those at 500^oC. The heat absorption rate is chosen to be the same as the one identified from the previous subsection. The resulting bending angles based on our simplified thermal and mechanical models are shown in Table 3.1, where b is the computed width of the plastic region; d is the computed depth of the plastic region; δ_a is the computed

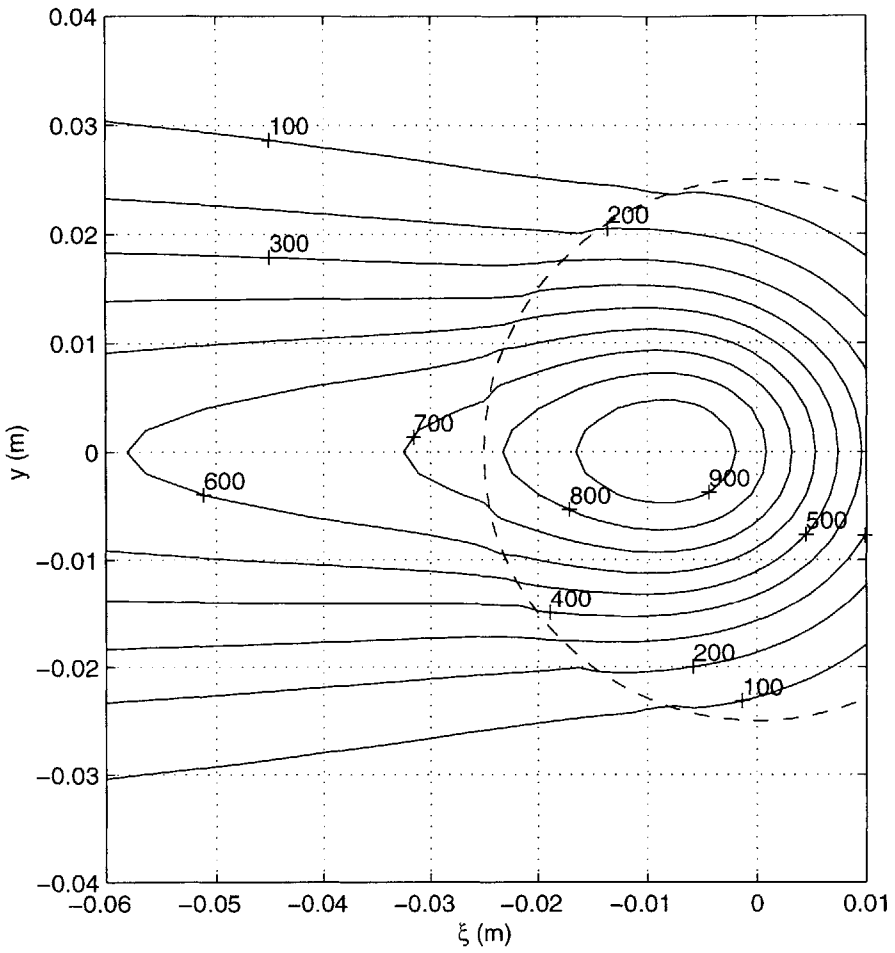

Figure 3-11: Temperature distribution on the top surface

bending angle, and δ_e is the average bending angle from experiments. We can see a general good match between the numerical and experimental results. The big error in Case 6 is probably due to experimental factors since only one specimen was heated for that case. This shows the effectiveness of the simplified model.

In order to show the efficiency and accuracy of the simplified model, we perform three-dimensional thermal and mechanical analysis of case 4 in Table 3.1 by using the finite element method. The mesh is shown in Figure 3-14. There are 4025 nodes in total and 3776 8-node or 6-node elements. Nonlinear thermal analysis is carried on first, followed by mechanical analysis. Table 3.2 shows the comparison of the CPU time spent on three dimensional FEM and that spent on simplified model, as well as the bending angles obtained. The bending angle obtained from FEM is the average

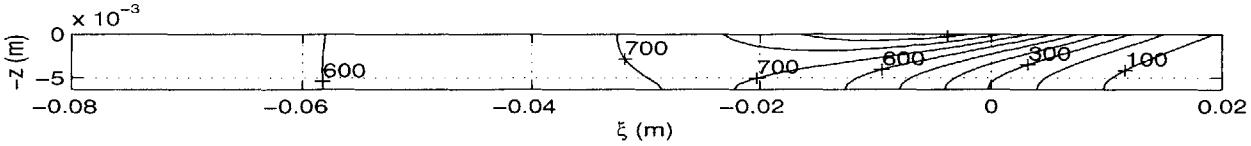

Figure 3-12: Temperature distribution at the cross section $y = 0$

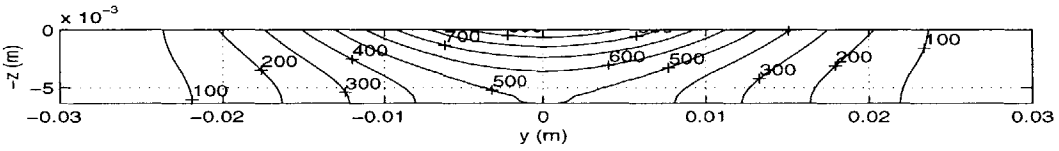

Figure 3-13: Temperature distribution at the cross section $\xi = -0.008$

of the bending angles evaluated at the 9 equal interval cross sections perpendicular to the heating line. All computations were executed on a Silicon Graphics workstation running at 200 MHz. It can be seen from Table 3.2 that the simplified model saves computation time by a factor of about 50, and the difference between the bending angle from FEM and that from the simplified model is within 10%.

3.4.3 Results of torch line heating on mild steel plates

Testing was conducted at the MIT Department of Ocean Engineering Fabrication Laboratory [1]. An oxy-acetylene heating torch was used as the heat source, the speed

Table 3.1: Plastic strain zone dimensions and bending angles

Case	spot size mm	speed mm/s	b mm	d mm	δ_a radians	δ_e radians	$\frac{\lvert\delta_a-\delta_e\rvert}{\delta_e} \times 100$
1	20.3	1.270	25.0930	6.1917	0.00836	0.00807	3.59
2	22.8	1.270	24.5918	5.2925	0.00664	0.00943	29.6
3	22.8	1.185	25.2760	5.6126	0.00723	0.00738	2.03
4	25.4	1.609	20.5524	3.2910	0.00329	0.00345	4.64
5	17.8	1.609	23.0076	6.0761	0.00806	0.00766	5.22
6	22.8	1.609	22.2612	4.2854	0.00484	0.00088	450
7	25.4	1.270	23.3916	4.3038	0.00492	0.00380	29.5
8	25.4	0.847	28.2550	6.4450	0.00880	0.00821	7.18
9	25.4	1.185	24.2075	4.6259	0.00548	0.00706	22.4

Table 3.2: Efficiency and accuracy of the simplified model

CPU (seconds) on 3D FEM			CPU (seconds) on	Bending angle (radians)	
Thermal	Mechanical	Total	simplified model	3D FEM	simplified model
12695	14401	27096	513.73	0.00299	0.00329

of which was controlled by a modified Kawasaki 6-axis programmable welding robot arm. Each line heating experiment by torch involved heating a plate along a single path at conditions which resulted in measurable deformation. Several parameters were measured during each experiment, including a calibrated value of heat flux, the angular deformation, and for some plates, the temperature variations at certain locations near the heating line. Prior to all line heating runs, a calibration procedure was conducted to establish a reference value of heat input for a given oxy-acetylene torch flame. The calibration was performed using an open steel container holding water. When a flame had been established for the line heating process, it was first applied to the container/water system for a given period of time. The temperature increase of the water was then measured. The heat input of the torch can be assumed to be proportional to the heat absorbed by water. Therefore, if we measure the temperature change of the water inside the container for a group of experiments, and we estimate the heat input from one experiment by measuring the temperature

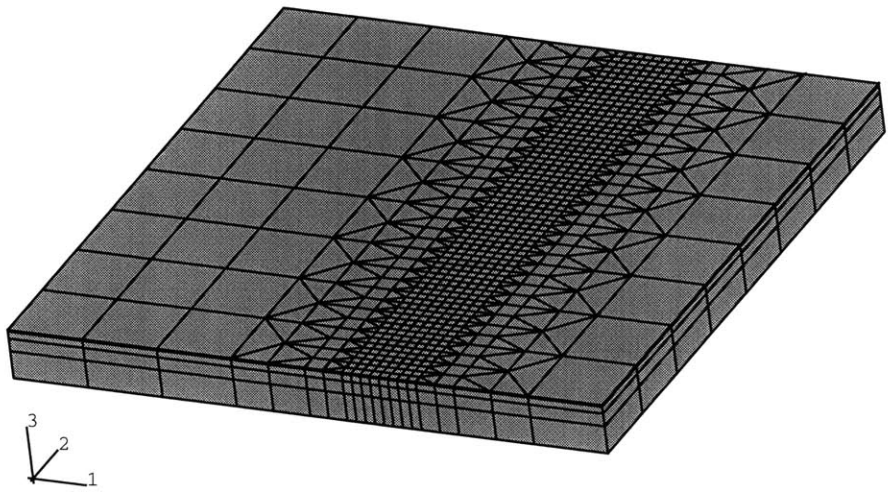

Figure 3-14: Mesh for three dimensional FEM analysis

distribution on the plate, we are able to estimate the heat flux from the torch to steel plates in each experiment. The reason for doing this is that measuring high temperature on steel plates while they are being heated is difficult. In order to have an accurate reading of the temperatures, thermo-couples for high temperature measurement must either be cemented or welded onto the plate. If thermo-couples are cemented onto metal plates, they can be reused, but the cement frequently cracks during experiments because of the deflection of the plates, so that good contact between thermo-couples and metal plates is compromised. If thermo-couples are welded onto metal plates, they risk being damaged during the welding process. In our experiments, thermo-couples were cemented onto the plates.

The plates used were AISI-SAE grade 1020 mild steel plates of $30.48 \times 30.48 \times 0.635$ (cm). For one of the plates tested, a line heating run was made in which temperatures were measured. During the line heating process, the temperature time histories at several points on the plate were recorded, which collectively provided the data for temperature distribution evaluation. The temperatures were measured using high temperature thermocouples, arranged as in Figure 3-15, and a data acquisition board.

Based on the temperature measurement, radius of heat flux region is determined

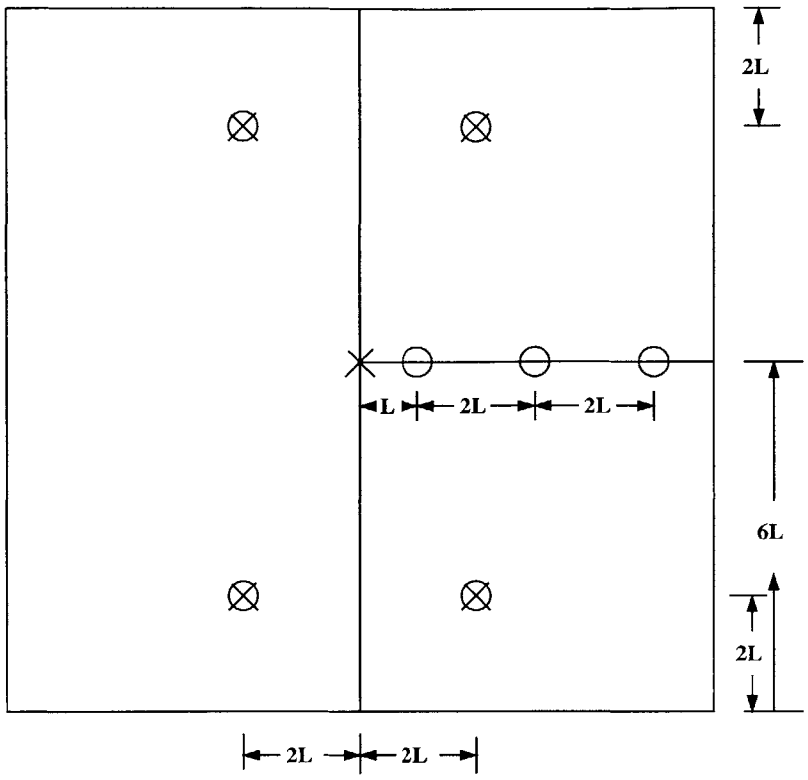

Figure 3-15: Thermocouple positions (circles for positions on top surface, cross for positions on bottom surface, and circle and cross together for positions on both top and bottom surfaces, and $L = 2.54\ cm$)

in an iterative way to match the peak temperatures at two measuring points on the plate. One is the center of the bottom surface, and the other is 2.54 cm off the heating line on the top surface. The determined radius of heat flux region is 2.76 cm. Figure 3-16 and 3-17 show the computed and the measured time series of temperatures at the two points.

Case 1 in Table 3.3 shows the computed bending plastic region dimensions, as well as the computed and the measured bending angles. For cases 2, 3, the same radius of the heat flux region as identified in case 1 is used. From the table, we can see that the computed bending angle in case 1 compares well with that measured in experiment, but the other cases are overheated cases ($d = g$), and the predicted bending angles are much smaller. This shows that line heating by torch is not an easily repeatable process. We can not use the heat flux size identified from one case in other cases. A series of separate experiments must be done to calibrate the heat flux, size of the

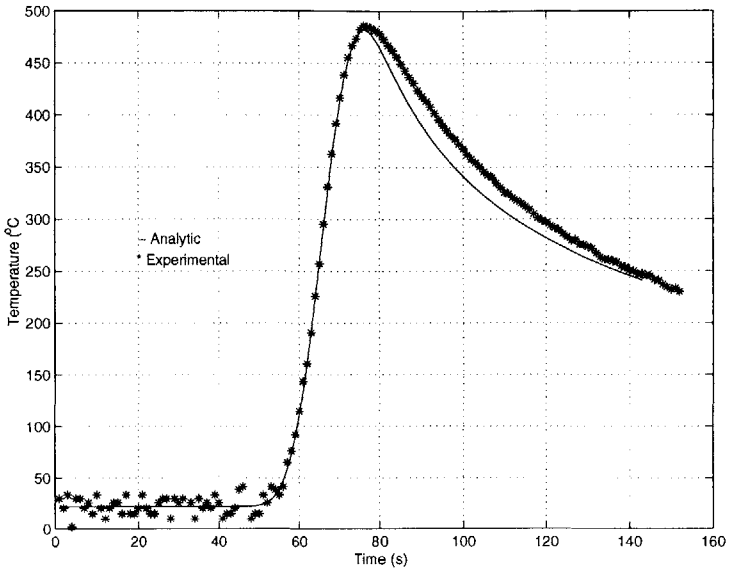

Figure 3-16: Comparison of experimental and matched analytic time temperature distributions on lower surface of the plate on heating line

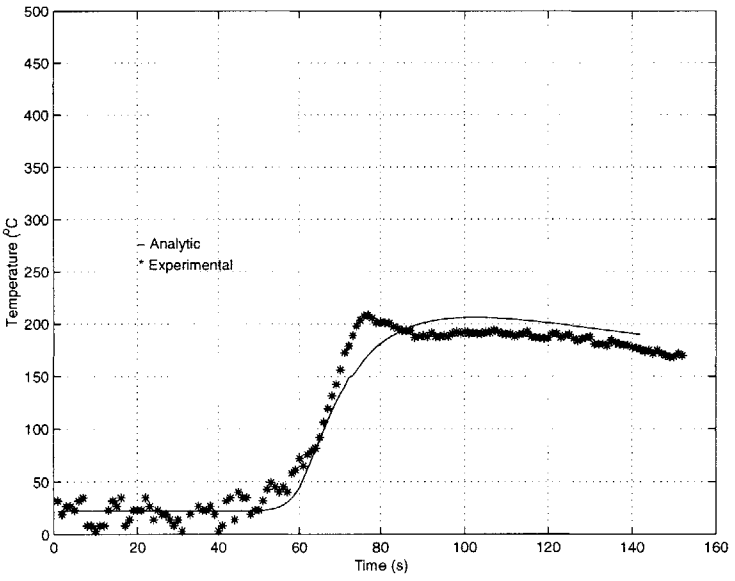

Figure 3-17: Comparison of experimental and matched analytic time temperature distributions on upper surface of the plate, 2.54 cm from the heating line

heat flux region with respect to the pressure of oxygen and acetylene gases.

Table 3.3: Plastic strain zone dimensions and bending angles for line heating using a torch

Case	q cal/s	r_0 mm	v mm/s	b mm	d mm	δ_a $radians$	δ_e $radians$
1	389	27.60	2.0	13.475	2.922	0.01968	0.01736
2	625	27.60	2.5	26.163	6.35	0.00275	0.0250
3	648	27.60	3.0	23.504	6.35	0.00548	0.0670

3.5 Discussion of outstanding issues

3.5.1 Approximation of material properties

The simplified model proposed in this chapter is based on the semi-analytical thermal model and the simplified mechanical model. The semi-analytical model employs Rothenthal's assumptions with respect to temperature distribution due to a moving heat source. The second assumption, that the speed of the moving heat source and the rate of heat input to the material are constant, is quite reasonable, so that the third assumption of a quasi-stationary heat flow holds. However, the first assumption, that the physical characteristics of the heated material are temperature-independent, is not true for most metallic materials. In our application, we use the material properties at an intermediate temperature, for both Inconel and mild steel. A reasonable choice of the temperature-independent material properties depends on the estimation of temperature field, which is unknown beforehand, and is itself dependent on the material properties. For example, if under a line heating condition, the maximum temperature inside a plate is T_{max}, then a choice of material properties based on an average temperature above T_{max} is certainly not reasonable.

3.5.2 Critical temperature in overheated case

Critical temperature plays an important role in approximately determining the width and depth of the plastic region and the resulting bending angle. For the underheated case, i.e. for smaller heat input or thicker plates, we have shown that 500^oC is a reasonable value. In overheated plates, temperature at the heated region is higher, so we can imagine that plastic strain occurs at a temperature higher than 500^oC, because the constraint from the surrounding areas becomes smaller. Therefore, a higher critical temperature should be used. Since in real practice, an overheated case is not desirable because of the possibility of material degradation, we do not investigate it in detail. It is possible to estimate a critical temperature for overheated case by performing additional experiments and comparing the numerical results with the experimental ones.

Chapter 4

Parametric study

4.1 Introduction

In simulation of the process of shell forming by line heating, it is found that certain critical parameters largely determine the temperature distribution and the resulting deformation of the plate. In this chapter, the effects of variations of these parameters on plate deformations are studied. Based on these studies, two nondimensional coefficients are derived from dimensional analysis. This chapter also presents edge effects, effects of repeated heating, and effects of parallel heating. These results are important in design of the line heating process.

4.2 Parametric study of heat input

In this section, we present the results of a parametric study of the effects of heat input on the angular distortion. The heating conditions similar to case 8 in Table 3.1 are used, except additional heat powers are investigated. The simplified model is used in simulation. The computed angular distortions are shown in Table 4.1 and Figure 4-1. The results are in general agreement with prior experimental observations [62]. That is, there is an optimal heat input, which generates the maximal bending angle.

Physically, this result can be explained from the change of temperature field with the change of heat flux. In metal forming by line heating, it is the gradient of the

Table 4.1: Bending angles under various heat input

Heat source power (kW)	Bending angle (radians)
2.0	0.00244
2.6	0.00880
3.2	0.01415
4.05	0.02266
4.3	0.02517
4.5	0.02649
4.8	0.02769
5.0	0.02719
5.1	0.02577
5.2	0.02149
5.4	0.00263

temperature field across the plate thickness that provides the mechanism of plate bending. Based on the simplified thermal model developed in Chapter 3, if only heat loss due to convection is considered, the temperature field is proportional to the heat input, which means that the temperature gradient is also proportional to the heat input. Therefore, before the heat input is large enough to overheat the plate, the size of plastic region and the resulting bending angle, increase with the increase of the heat input. We see from Figure 4-1 that the bending angle first increases with the increase of the heat input.

When the heat input becomes larger, plastic region penetrates through the thickness, and the equivalent bending moment decreases, so we see in Figure 4-1 that the bending angle decreases with the increase of the heat input at high heat input. In the mean time, because the radiation heat loss is proportional to the fourth power of temperature, heat loss is more significant on the hotter surface than on the cooler surface. Thus the temperature gradient may indeed decrease with the increase of heat input, when the heat input is very large. This also contributes the decrease of the bending angles at high heat input.

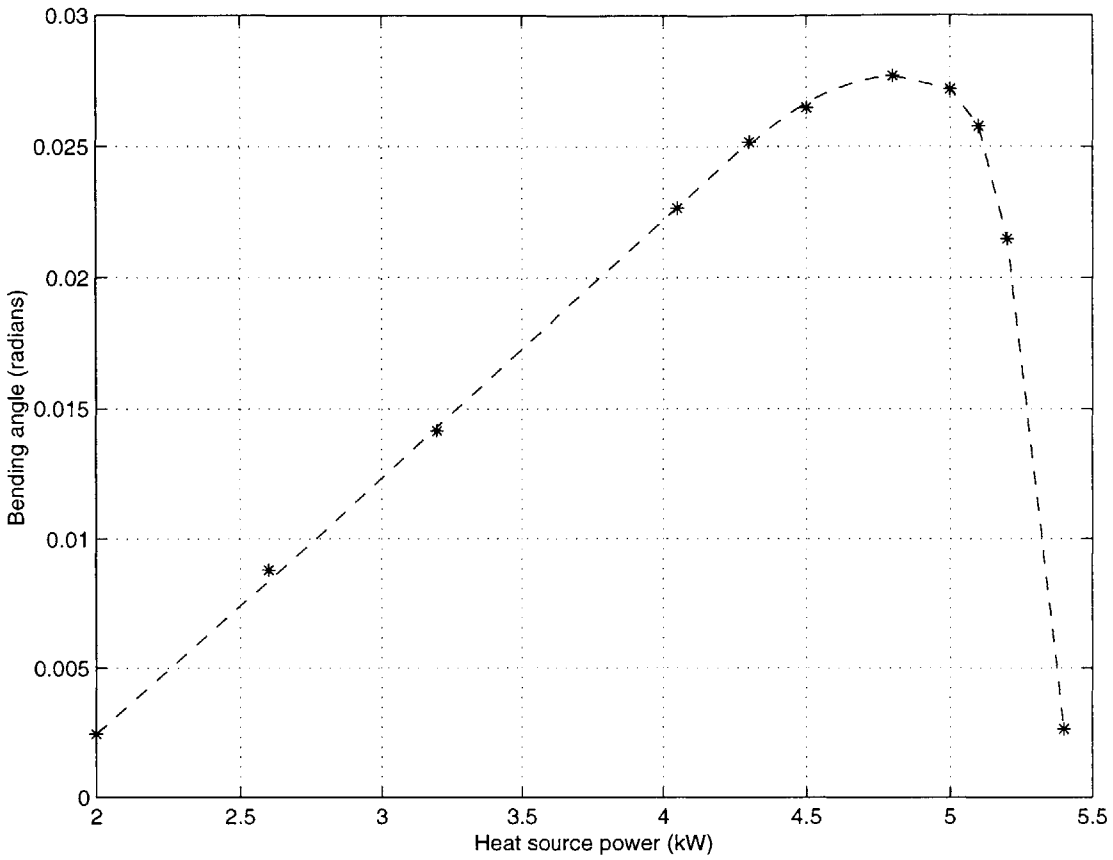

Figure 4-1: Bending angle as a function of heat source power

4.3 Parametric study of heat source velocity

In this section, the effects of varying heat source moving velocity on the dimensions of plastic region and the resulting bending angles are investigated. The heating conditions similar to cases 4, 7, 8, 9 in Table 3.1 are used, except additional velocities are investigated. The simplified model is used in the computation. Table 4.2 shows the resulting dimensions of plastic region and bending angles. Figure 4-2 shows the change of bending angles with respect to change of heat source moving velocity. From Figure 4-2 we see that there is also an optimal heat source velocity which generates maximal bending angle. Physically, based on the simplified model developed in Chapter 3, temperature at any location increases when heat source velocity decreases. Therefore, temperature gradient across the thickness, and the resulting bending angle increase when heat source velocity decreases, until the velocity is small enough for plastic

region to penetrate the thickness. At that time, if the heat source velocity is decreased further, the equivalent bending moment due to line heating decreases, so that bending angle decreases.

Table 4.2: Plastic strain zone dimensions and bending angles with varying heat source moving velocity

Case No.	spot size mm	speed mm/s	b mm	d mm	δ radians
1	25.4	0.200	53.6795	25.4	0.00076
2	25.4	0.250	47.7998	25.4	0.00145
3	25.4	0.280	45.3423	25.4	0.00183
4	25.4	0.290	44.4578	25.4	0.00188
5	25.4	0.293	44.3379	25.4	0.00191
6	25.4	0.294	44.1769	25.4	0.00193
7	25.4	0.295	44.145	24.358	0.01502
8	25.4	0.300	43.7952	22.373	0.01850
9	25.4	0.350	41.8027	16.3943	0.02254
10	25.4	0.400	38.5929	13.7559	0.02035
11	25.4	0.500	35.3361	10.9268	0.01668
12	25.4	0.600	32.7585	8.9702	0.01353
13	25.4	0.847	28.2550	6.4450	0.00880
14	25.4	0.900	27.5041	6.0779	0.00811
15	25.4	1.000	26.2295	5.4871	0.00702
16	25.4	1.185	24.2075	4.6259	0.00548
17	25.4	1.270	23.3916	4.3038	0.00492
18	25.4	1.400	22.2328	3.8706	0.00420
19	25.4	1.609	20.5524	3.2910	0.00329
20	25.4	1.800	19.1474	2.8494	0.00264

The shape of the curve in Figure 4-2 can also be obtained qualitatively by using results from heat transfer theory [53]. The characteristic heat diffusion length is $\sqrt{\alpha t}$, where α is the thermal diffusivity. The characteristic time $t = d_0/v$ with d_0 the diameter of the heated region, and v the heat source velocity. Therefore, both the breadth b and thickness d of the plastic region should be proportional to $\sqrt{1/v}$. When v is high, and d is small compared to the plate thickness g, the bending angle will be proportional to bd and therefore to $1/v$, based on equation (3.74). We see the right part of the curve in Figure 4-2 has this kind of shape. After one run of the

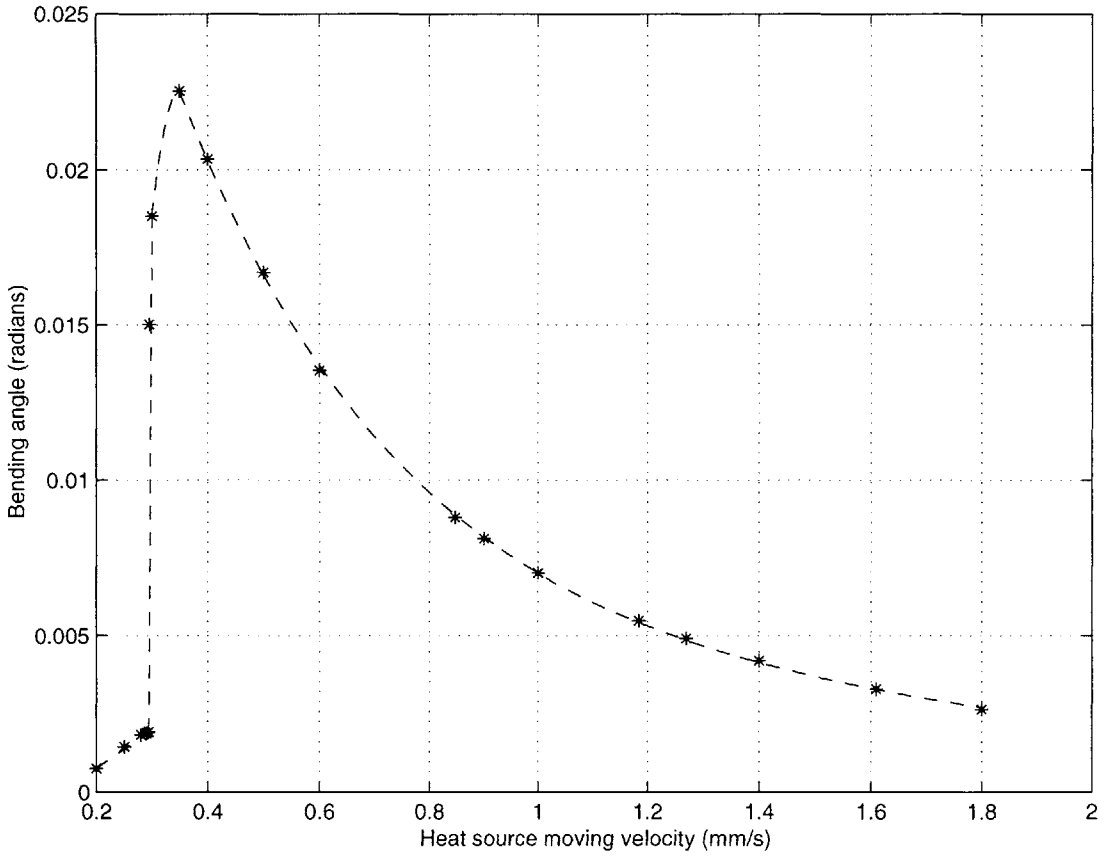

Figure 4-2: Bending angle as a function of heat source moving velocity

simplified model with high v, we can estimate roughly the velocity v_m corresponding to the maximum bending angle based on the relation $d \sim \sqrt{1/v}$, and the condition that at v_m, $d_m \approx \frac{g}{2}$. Of course, due to the finite thickness of the plate, this estimation is approximate, especially for the depth d of the plastic region, i.e. d will not be precisely proportional to $\sqrt{1/v}$.

4.4 Parametric study of spot size

In this section, the effects of varying spot size on the dimensions of plastic region and the resulting bending angles are investigated. The heating conditions similar to cases 1, 2, 7 in Table 3.1 are used, except additional spot sizes are investigated. The simplified model is used in simulation. Table 4.3 shows the resulting dimensions of plastic region and bending angles. Figure 4-3 shows the change of bending angles with respect to change of spot size. Physically, when spot size is very small, the heat flux is concentrated at a very small area, so that the plastic region is small even though the temperature inside the heat flux region is high. When spot size increases, the plastic region increases, so that bending angle first increases. When the spot size further increases, the heat flux becomes less and less concentrated, so the temperature inside the heat flux region decreases and the plastic region decreases. Therefore, bending angle decreases later when spot size further increases.

4.5 Effects of heat loss

In order to investigate the effects of heat loss, we performed numerical simulation of case 8 in Section 4.4, using 4 groups of heat loss coefficients (h_U, h_L): $(1.0, 0.5)$, $(10.0, 5.0)$, $(50.0, 25.0)$, $(100.0, 50.0)$ $Wm^{-2}K^{-1}$. The resulting plastic zone dimensions and the bending angles are shown in Table 4.4. In the table, $(h_U, h_L) = (10.0, 5.0)$ $Wm^{-2}K^{-1}$ corresponds to the coefficient of heat loss due to natural convection. $(h_U, h_L) = (100.0, 50.0)$ $Wm^{-2}K^{-1}$ corresponds to the upper bound of the equivalent coefficient of heat loss due to convection and radiation, and $(h_U, h_L) =$

Table 4.3: Plastic strain zone dimensions and bending angles with varying spot sizes

Case No.	spot size mm	speed mm/s	b mm	d mm	δ $radians$
1	15.0	1.270	21.8107	7.8530	0.01106
2	15.5	1.270	24.9311	7.7116	0.01214
3	15.8	1.270	24.4633	7.6236	0.01628
4	16.0	1.270	24.4354	7.6257	0.01492
5	16.25	1.270	24.4441	7.4945	0.01121
6	16.5	1.270	24.5682	7.4187	0.01105
7	17.5	1.270	24.9403	7.1529	0.01041
8	20.3	1.270	25.0930	6.1917	0.00836
9	22.8	1.270	24.5918	5.2925	0.00664
10	25.4	1.270	23.3916	4.3038	0.00492
11	30.0	1.270	18.9103	2.4386	0.00215

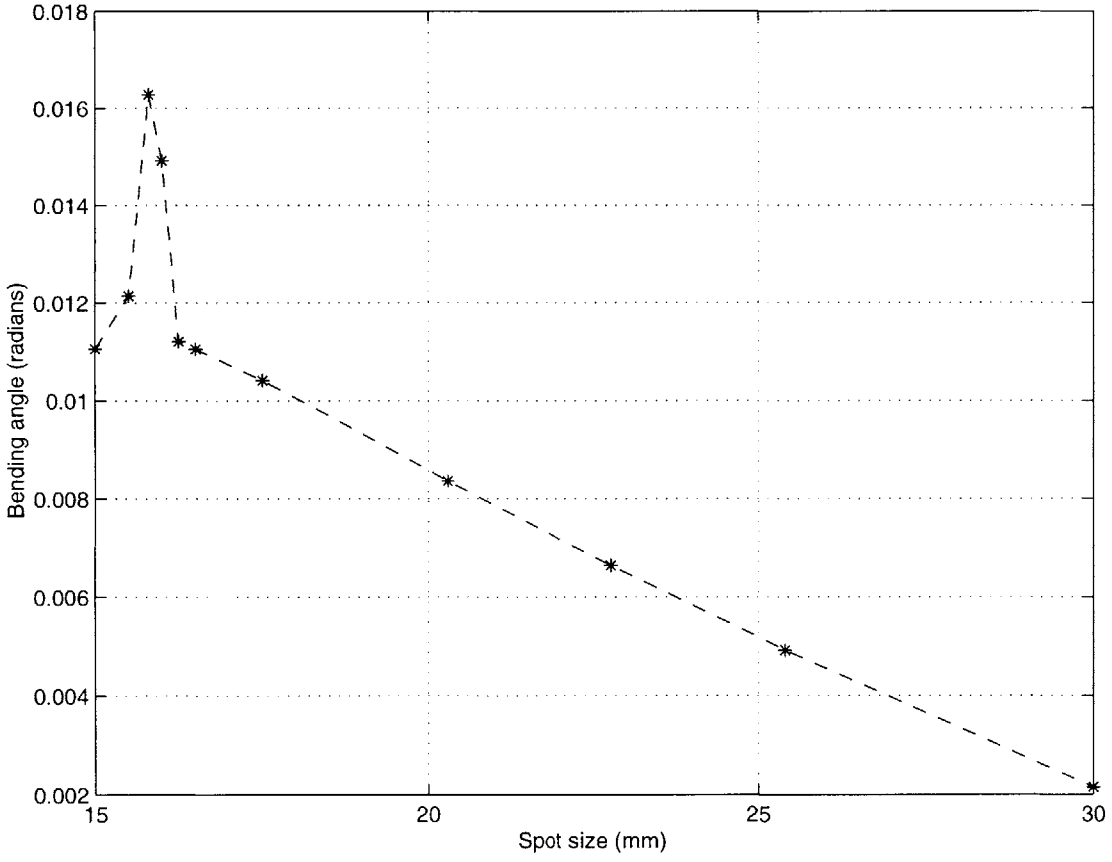

Figure 4-3: Bending angle as a function of spot size

$(1.0, 0.5)$ $Wm^{-2}K^{-1}$ corresponds to very small heat loss coefficients. From the table, we see the effects of heat loss on the plastic zone dimensions and bending angles are minimal. Figures 4-4, 4-5, and 4-6 show the temperature distributions (isothermal contours) on the top surface for cases 1, 2, 4, respectively. We see the difference in isothermal contour lines is also very small. The reason for this result is that heat conduction within the mild steel plate is much faster than that from mild steel plate to air because the heat conductivity of mild steel is much larger than that of air.

Table 4.4: Plastic strain zone dimensions and bending angles with varying heat loss coefficients

Case No.	h_U $Wm^{-2}K^{-1}$	h_L $Wm^{-2}K^{-1}$	b mm	d mm	δ $radians$
1	1.0	0.5	25.1405	6.21210	0.00841
2	10.0	5.0	25.0930	6.19172	0.00836
3	50.0	25.0	24.8872	6.10243	0.00816
4	100.0	50.0	24.6346	5.99435	0.00792

4.6 Proposed nondimensional coefficients

In this section, we derive the similarity rule for the process of shell forming by line heating. As we know, the process can be divided into a thermal conduction problem and the corresponding deformation problem. Therefore, we discuss the similarity rule in each problem.

Deformation problem

For two geometrically similar models with thickness g_1 and g_2, if the material properties E, E_D, ν, ν_D are the same, and the temperature distribution T at corresponding points is the same, i.e.

$$T_1(r_1, z_1) = T_2(r_2, z_2) \tag{4.1}$$

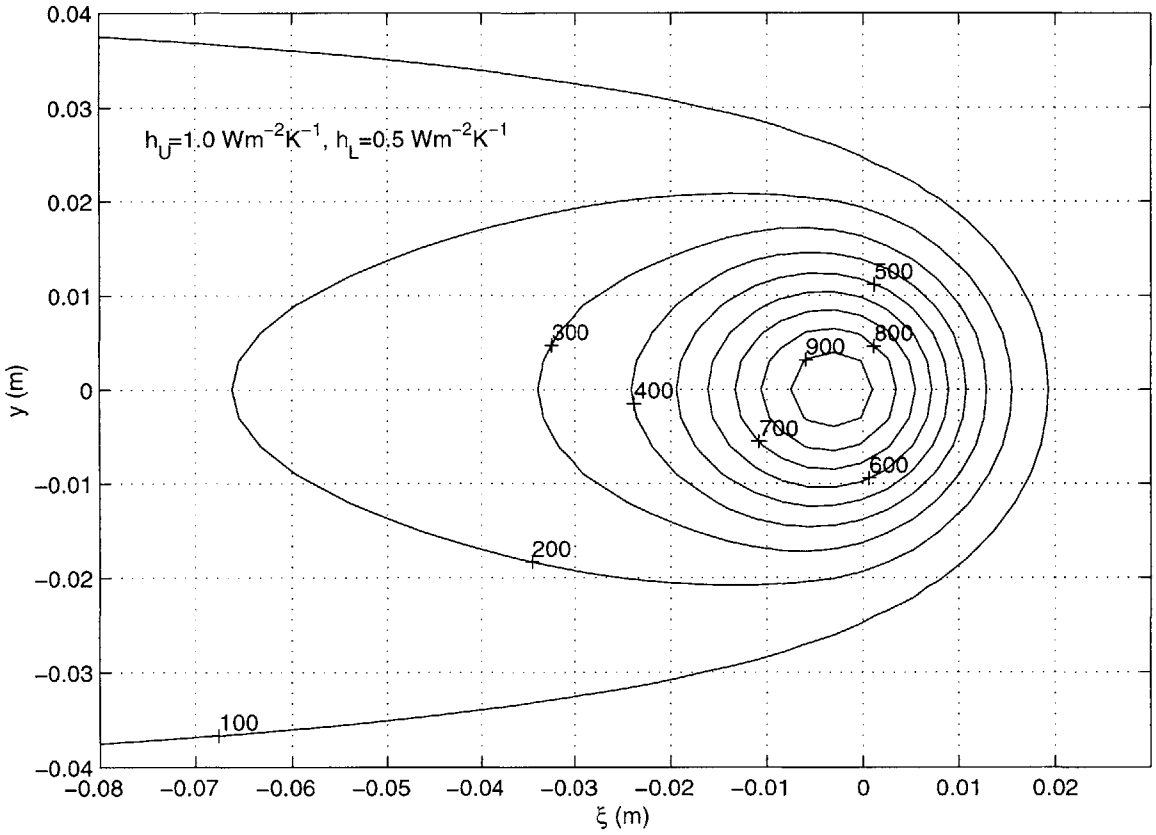

Figure 4-4: Temperature distributions on top surface for case 1

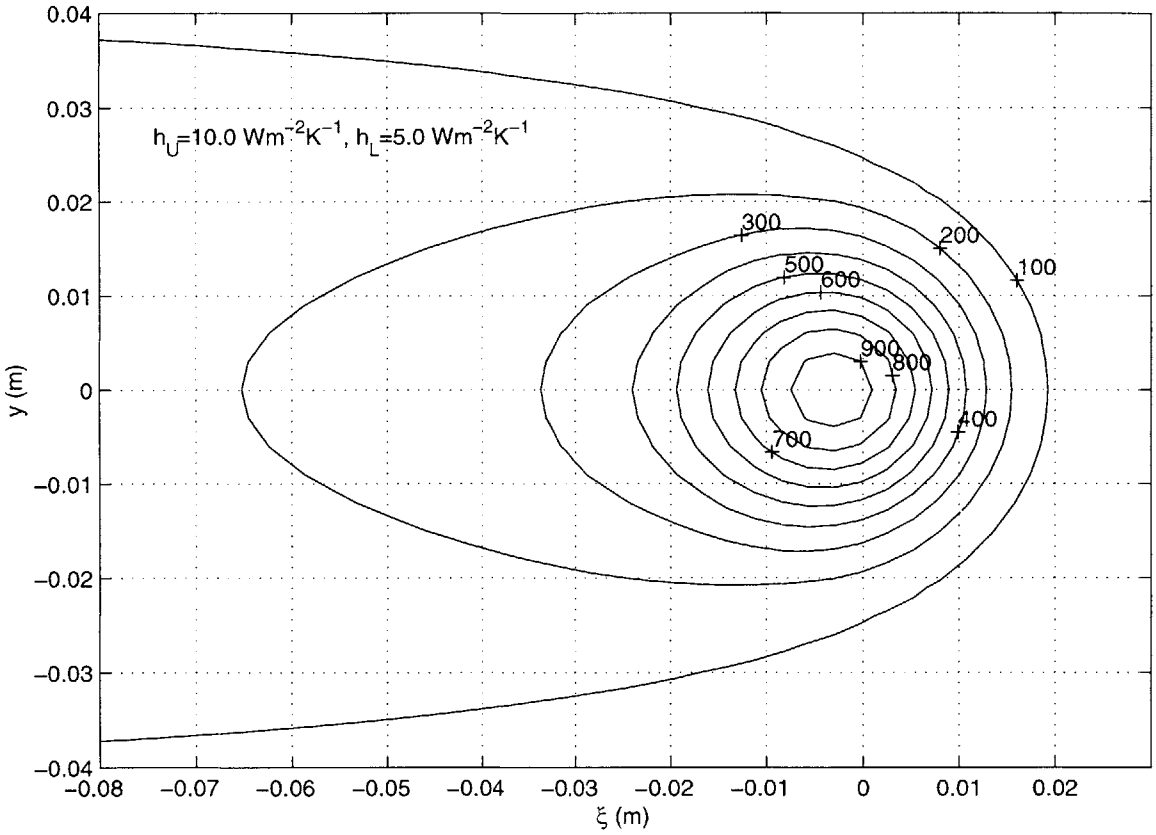

Figure 4-5: Temperature distributions on top surface for case 2

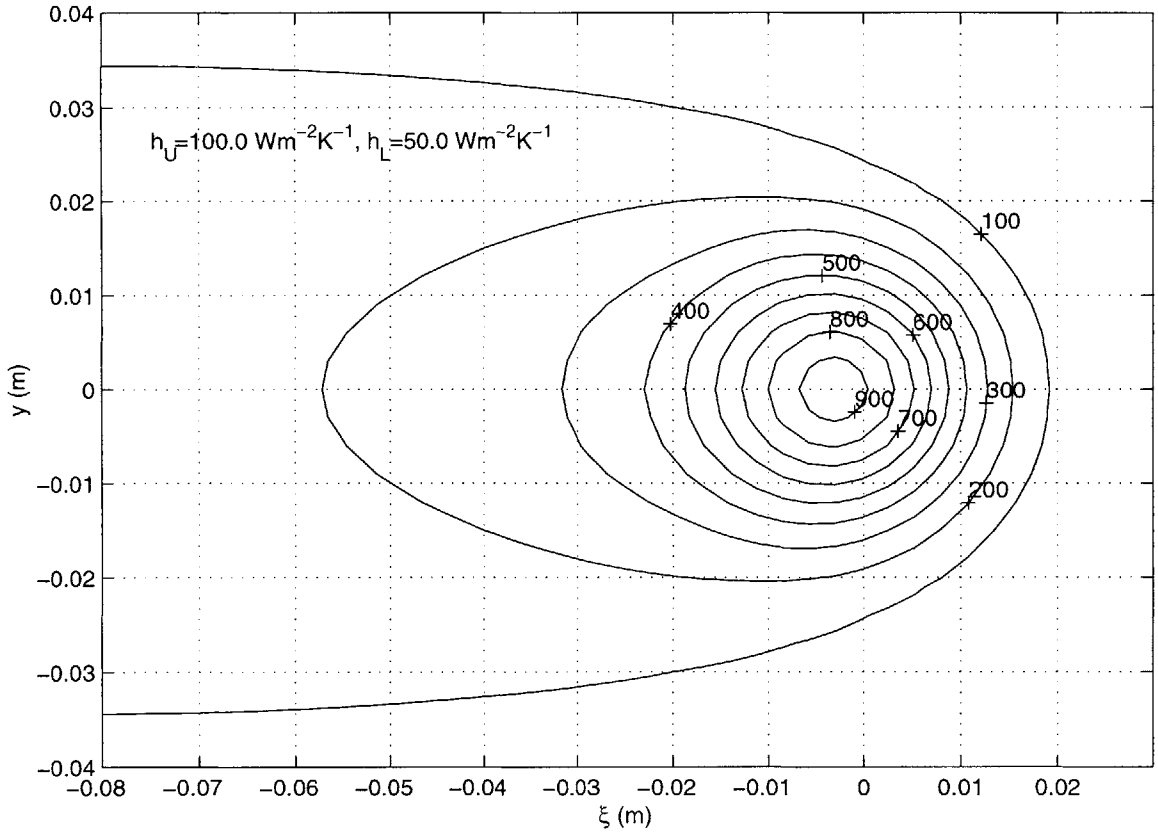

Figure 4-6: Temperature distributions on top surface for case 4

where

$$\frac{r_1}{r_2} = \frac{z_1}{z_2} = \frac{g_1}{g_2} = c \tag{4.2}$$

Then we can easily obtain the relations between the sizes of plastic regions

$$b_1 = cb_2, \quad d_1 = cd_2 \tag{4.3}$$

From equation (3.60), the residual strain

$$\epsilon^*_{rr1} = \epsilon^*_{rr2} \tag{4.4}$$

and from either equation (3.74) or equation (3.75), we obtain

$$\delta_1 = \delta_2 \tag{4.5}$$

Therefore, deformation similarity holds for geometrically similar models when temperature T is the same at corresponding points.

Heat conduction problem

Ueda et al. [60] first derived two governing nondimensional parameters for the heat conduction process. Since the heat input and heat source moving velocity are coupled together in these coefficients, interpreting their meanings is not easy. The two parameters derived here have clearer meaning and allow the separation of heat input and the heat source moving velocity.

For the heat conduction problem, the temperature field T in the process of metal forming by line heating is governed mainly by the heat conductivity k, thermal diffusivity $\alpha = \frac{1}{2\lambda}$, plate thickness g, total heat input from source q, heat source moving velocity v, and a reference temperature which is chosen as the maximum temperature in the plate T_{max}. We choose the basic dimensions to be mass (M), length (L), time (t), and temperature (T), then the governing parameters have the following

dimensions:

$$\begin{aligned} [q] &= [ML^2t^{-3}] \\ [v] &= [Lt^{-1}] \\ [k] &= [MLt^{-3}T^{-1}] \\ [\alpha] &= [L^2t^{-1}] \\ [g] &= [L] \\ [T_{max}] &= [T] \end{aligned}$$

According to the method for dimensional analysis [5] [50], the temperature T can be expressed as a function of these basic variables

$$T = \phi(q^a, v^b, k^c, \alpha^d, g^e, T_{max}^f) \tag{4.6}$$

The dimensional form of the above equation is

$$T = (ML^2t^{-3})^a(Lt^{-1})^b(MLt^{-3}T^{-1})^c(L^2t^{-1})^d L^e T_{max}^f \tag{4.7}$$

The dimensions of both sides of equation (4.7) must be the same, so we have the following relations

$$\begin{aligned} a + c &= 0 \\ 2a + b + c + 2d + e &= 0 \\ -3a - b - 3c - d &= 0 \\ -c + f &= 1 \end{aligned} \tag{4.8}$$

After solving for c, d, e, f from system (4.8), we obtain

$$c = -a, \quad d = -b, \quad e = b - a, \quad f = 1 - a \tag{4.9}$$

After substituting equations (4.9) into equation (4.7), we obtain

$$T = q^a v^b k^{-a} \alpha^{-b} g^{b-a} T_{max}^{1-a} \tag{4.10}$$

$$= \left(\frac{q}{kgT_{max}}\right)^a \left(\frac{vg}{\alpha}\right)^b T_{max} \tag{4.11}$$

or, in nondimensional form

$$\frac{T}{T_{max}} = \left(\frac{q}{kgT_{max}}\right)^a \left(\frac{vg}{\alpha}\right)^b \tag{4.12}$$

From equation (4.12), we see the two nondimensional parameters are

$$c_1 = \frac{q}{kgT_{max}} \tag{4.13}$$

$$c_2 = \frac{vg}{\alpha} \tag{4.14}$$

In the above equations, c_1 is the nondimensional heat input, and c_2 is the nondimensional heat source velocity. Compared with the nondimensional parameters presented by Ueda et al. [60], c_1 is the same, but c_2 presented here has a much simpler form and clearer meaning. As discussed, the maximum temperature must be the same for similarity in the deformation problem. Therefore, we can also choose

$$c_3 = \frac{q}{kg} \tag{4.15}$$

instead of c_1 as the parameter for heat input, but then c_3 is dimensional.

4.7 Edge effects

In the experimental study [62], it was observed that a laser line heat pass creates less bending as it approaches a free edge. We investigated this phenomenon by 3D FEM simulations. Five heating lines at locations $\frac{1}{2}L$, $\frac{3}{8}L$, $\frac{1}{4}L$, $\frac{1}{8}L$, and $\frac{1}{16}L$ from the free edge were simulated, where L is the edge length of the plate, $L = 30.48cm$. The heat source moving velocity is $7.62cm/min$; the power of the laser is 2.6 kW.

After thermo-mechanical analyses, the bending angles for various locations of the heating lines are computed by averaging the bending angles at 9 cross sections at $y = \frac{i}{8}L,\ i = 0, 1, ..., 8$, see Figure 4-7 for the coordinate system. The results are shown in Table 4.5 and Figure 4-8. In Table 4.5, d/L is the non-dimensional distance of the heating line from the free edge. δ is the bending angle. These results are in good agreement with the experimental observations, i.e. it is more difficult to bend a plate by heating it near the free edge than in the middle area.

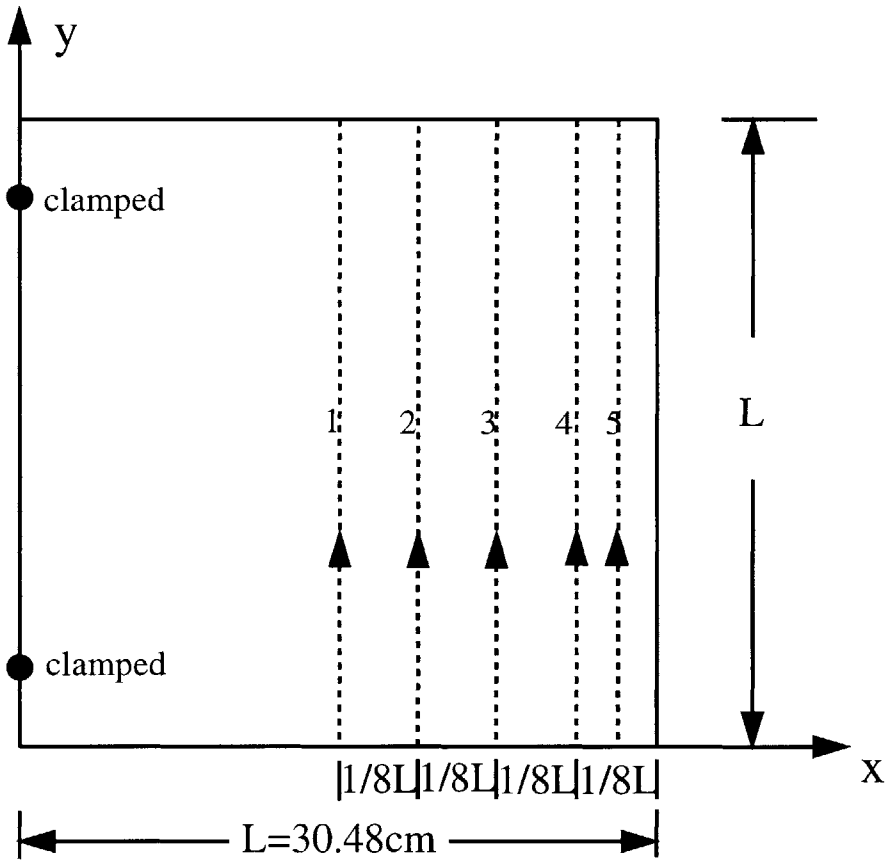

Figure 4-7: Heating lines for analysis of edge effects

Table 4.5: Average bending angles when heating at various locations

Heating line No.	1	2	3	4	5
d/L	1/2	3/8	1/4	1/8	1/16
δ (degrees)	0.2341	0.2287	0.2041	0.1331	0.0320

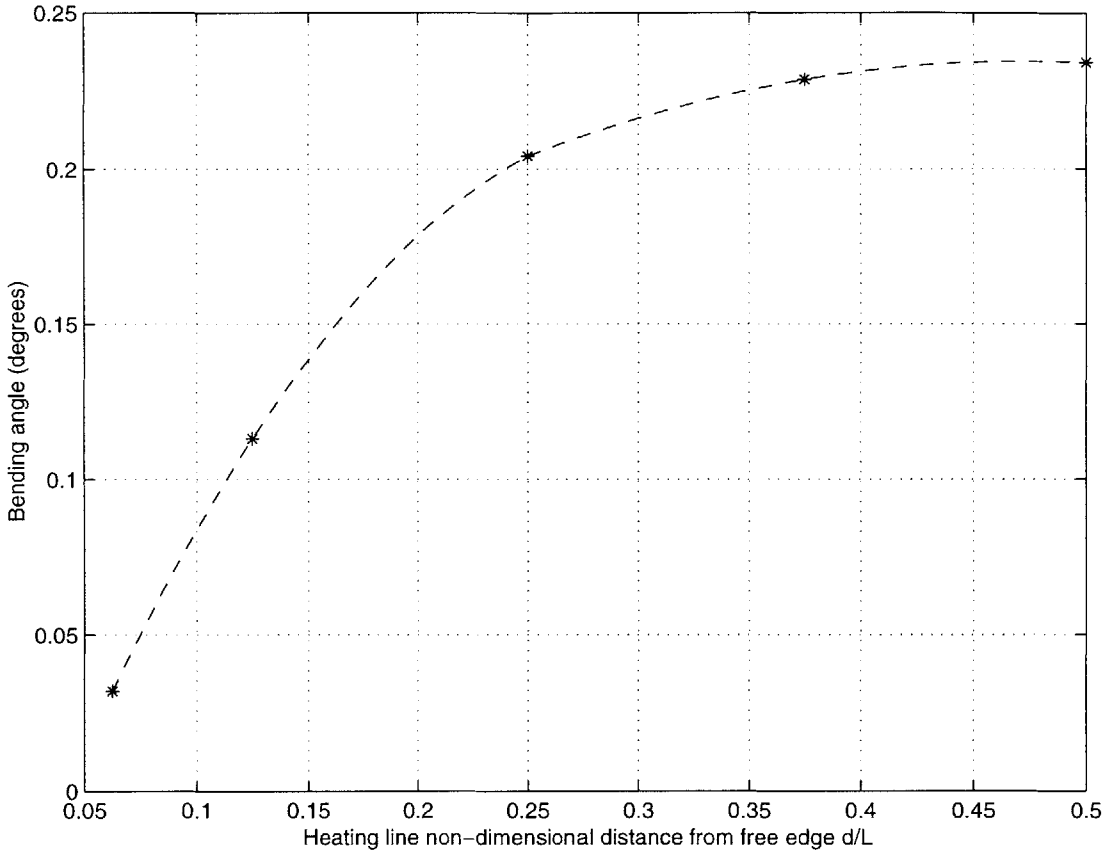

Figure 4-8: Edge effect – bending angle as a function of heating line distance from edge

4.8 Effects of repeated heating

In this section, the effects of repeated heating on plate deformations are investigated. Three dimensional thermo-mechanical FEM simulations are performed for repeatedly heating along line 1 in Figure 4-7. The plates are still $30.48cm \times 30.48cm \times 2.54cm$ mild steel plates. The heat source moving velocity is $7.62cm/min$, and the power of the laser heat source is 2.6 kW. The plate is heated by the first pass, then cools down, and is heated by the second pass, cools down, and is heated by the third pass. Figure 4-9 shows the time series of the vertical displacement at the point with the coordinate $(L,\ L/2,\ 0)$, see Figure 4-7 for the coordinate system. From Figure 4-9, we see later

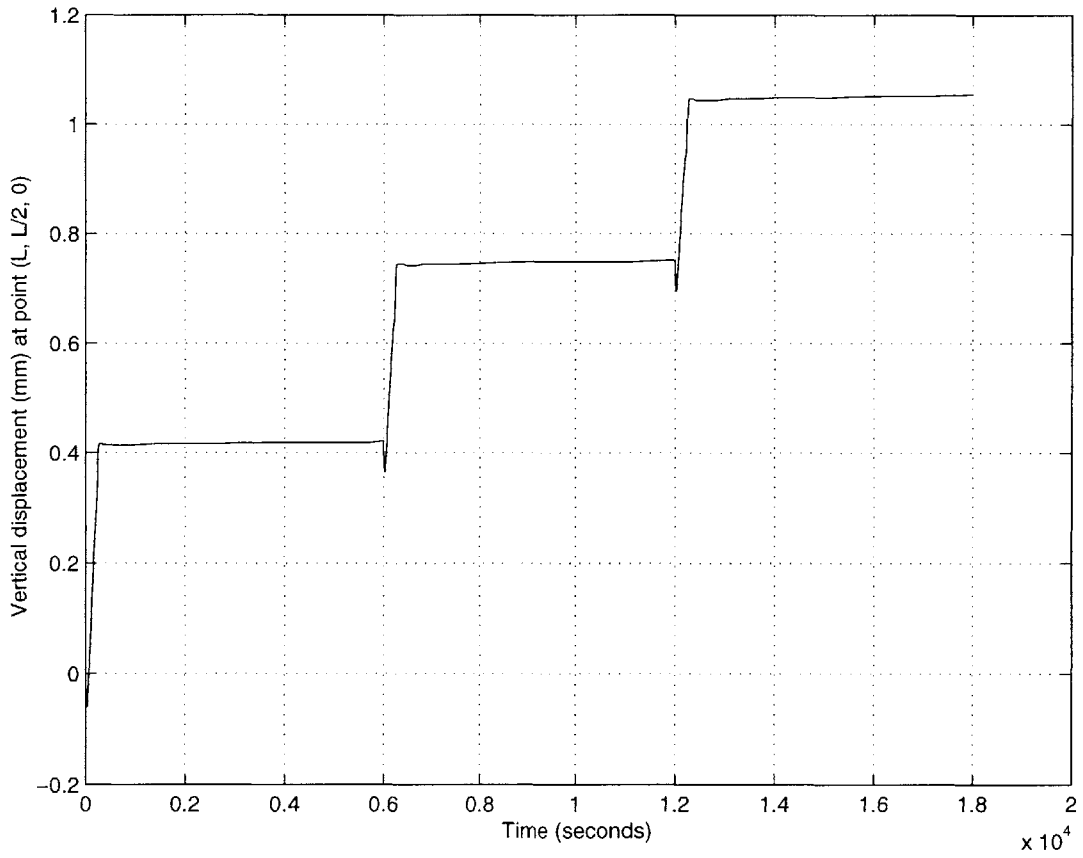

Figure 4-9: Vertical displacement at the point $(L,\ L/2,\ 0)$

heating passes generate similar displacements compared with the first pass, which is consistent with the experimental observation that repeated heating increasingly bends a plate. However, the displacement in a later pass is progressively smaller than

that from a previous heating pass. Physically, this means that later heating passes generate less plastic strains if the peak temperatures for points in the heated flux region stay the same during each heating pass. Since the sole mechanism of bending the plate during the line heating process is thermal stress, without heating condition change, the subsequent heating passes tend to repeat the elastic-platic loading and unloading process with less new plastic strains generated. Therefore, we see later heating passes become less effective.

4.9 Effects of parallel heating

In this section, the effects of parallel heating on plate deformations are investigated. Three dimensional thermo-mechanical FEM simulations are performed both for sequentially heating along two parallel lines and for heating along each line separately. The plates are still $30.48cm \times 30.48cm \times 2.54cm$ mild steel plates. The heat source moving velocity is $7.62cm/min$, and the power of the laser heat source is 2.6 kW. The two heating lines are shown in Figure 4-10. In sequential heating, the plate is first heated along line 1 in Figure 4-10, and after it cools, it is heated along line 2 in Figure 4-10. Table 4.6 shows the vertical displacements at locations A, B, C in Figure 4-10. For comparison, the vertical displacements at locations A, B, C after heating only along line 1 or line 2 are also presented. We see that here superposition holds well for displacements at these points, which implies that the residual stresses after heating along line 1 have small effects on the heating along line 2.

In general, residual stresses from previous heating have bigger effects on subsequent heating if the distance between the heating lines is smaller.

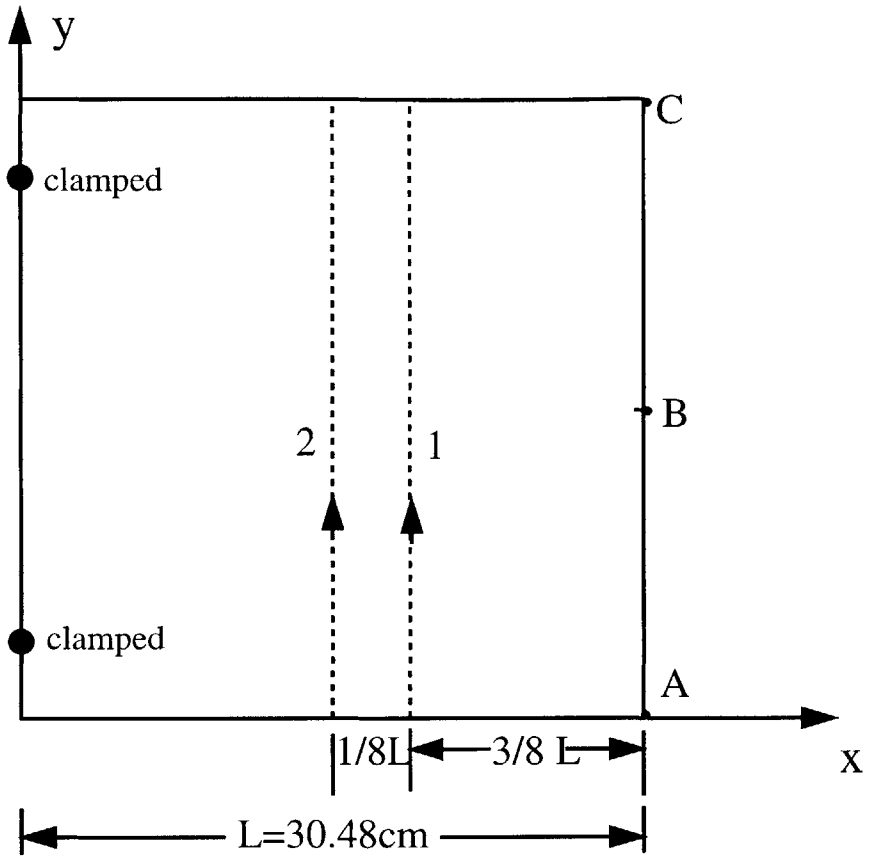

Figure 4-10: Parallel heating lines

Table 4.6: Vertical displacements at locations A, B, C

Case No.	Heating condition	z_A (cm)	z_B (cm)	z_C (cm)
1	Line 1 only	0.0480	0.0425	0.0503
2	Line 2 only	0.0630	0.0600	0.0646
3	Superposition of cases 1, 2	0.1110	0.1025	0.1149
4	Line 1 first, then line 2	0.1195	0.1081	0.1237
	Error between cases 3, 4 (%)	7.7	5.4	7.6

Chapter 5

Optimal development of doubly curved surfaces for line heating planning

5.1 Introduction

In this chapter, we develop algorithms for optimal development of a general doubly curved surface in the sense that the strain from the surface to its planar development is minimized. A tensile strain (stretching) from the curved surface to its planar development is assumed which corresponds to forming from the planar shape to curved surface by the line heating approach [49, 63]. From optimal development of a double curved surface, we can not only determine the initial planar shape to start from, but also obtain the ideal compressive strains to produce during the line heating process. Determine the initial planar shape first is important since it not only save material, but also make the cutting process easy. Heating line directions can be determined based on the surface development process. The surface development process is based on geometric theory except for the use of the concept of strains. The results from optimal development of doubly curved surfaces are published in a recent paper [64].

5.2 Surface theory

5.2.1 Background on differential geometry of surfaces

A parametric surface in 3D Euclidean space is defined by [17]

$$\mathbf{r} = \mathbf{r}(u, v) \tag{5.1}$$

where the parameters u and v are restricted to some intervals (i.e., $u_1 \leq u \leq u_2$, $v_1 \leq v \leq v_2$) leading to parametric surface patches. This rectangular domain D of u, v is called *parametric space* and it is frequently the unit square. If derivatives of the surface are continuous up to the r^{th} order, the surface is said to be of class r, denoted C^r.

First and second fundamental forms

Consider a curve C on a surface S defined by $\mathbf{r} = \mathbf{r}(u(t), v(t))$. The arc length of the curve on the surface is given by [12]

$$ds = \sqrt{Edu^2 + 2Fdudv + Gdv^2} \tag{5.2}$$

where

$$E = \mathbf{r}_u \cdot \mathbf{r}_u, \quad F = \mathbf{r}_u \cdot \mathbf{r}_v, \quad G = \mathbf{r}_v \cdot \mathbf{r}_v \tag{5.3}$$

and subscripts u, v denote partial derivatives. The first fundamental form is defined as

$$I = d\mathbf{r} \cdot d\mathbf{r} = Edu^2 + 2Fdudv + Gdv^2 \tag{5.4}$$

where E, F, G are called coefficients of the first fundamental form.

In order to quantify the curvatures of a surface S, we consider a curve C on S which passes through a point P as shown in Figure 5-1. $\mathbf{t}$ is the unit tangent vector

and $\mathbf{n}$ is the unit normal vector of the curve C at point P. Then the curvature vector $\mathbf{k}$ of the curve C can be expressed as:

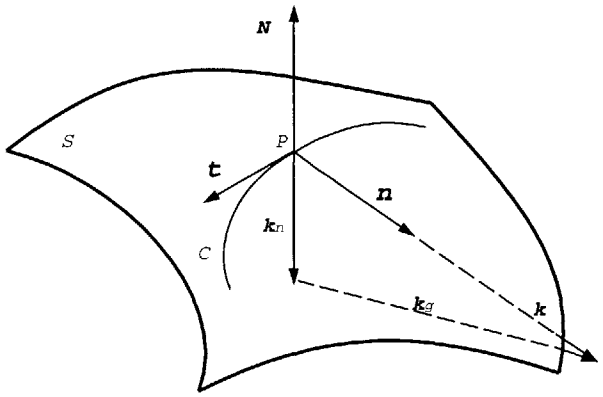

Figure 5-1: Definition of normal curvature

$$\mathbf{k} = \frac{d\mathbf{t}}{ds} = \kappa\mathbf{n} = \mathbf{k}_n + \mathbf{k}_g \tag{5.5}$$

where $\mathbf{k}_n$ is the normal curvature vector normal to the surface; $\mathbf{k}_g$ is the geodesic curvature vector tangent to the surface. Since $\mathbf{k}_n$ is along the surface normal, it can be written as

$$\mathbf{k}_n = \kappa_n\mathbf{N}, \tag{5.6}$$

where κ_n is called the normal curvature of the surface at P in the direction $\mathbf{t}$, and $\mathbf{N}$ is the unit normal of the surface

$$\mathbf{N} = \frac{\mathbf{r}_u \times \mathbf{r}_v}{|\mathbf{r}_u \times \mathbf{r}_v|} \tag{5.7}$$

The second fundamental form is given by

$$II = -d\mathbf{r} \cdot d\mathbf{N} = Ldu^2 + 2Mdudv + Ndv^2 \tag{5.8}$$

where

$$\begin{aligned} L &= \mathbf{N} \cdot \mathbf{r}_{uu} = -\mathbf{r}_u \cdot \mathbf{N}_u \\ M &= \mathbf{N} \cdot \mathbf{r}_{uv} = -\mathbf{r}_u \cdot \mathbf{N}_v = -\mathbf{r}_v \cdot \mathbf{N}_u \end{aligned}$$

$$N = \mathbf{N} \cdot \mathbf{r}_{vv} = -\mathbf{r}_v \cdot \mathbf{N}_v \tag{5.9}$$

are coefficients of the second fundamental form. The normal curvature can be expressed by

$$\kappa_n = \frac{II}{I} = \frac{L + 2M\lambda + N\lambda^2}{E + 2F\lambda + G\lambda^2} \tag{5.10}$$

where $\lambda = \frac{dv}{du}$.

Gauss curvature

The extreme values of κ_n can be obtained by evaluating $\frac{d\kappa_n}{d\lambda} = 0$ of Equation (5.10), which gives after several algebraic manipulations:

$$\kappa_n^2 - 2H\kappa_n + K = 0 \tag{5.11}$$

The values K and H are called Gauss (Gaussian) and mean curvature respectively. They are functions of the coefficients of the first and second fundamental forms as follows:

$$K = \frac{LN - M^2}{EG - F^2} \tag{5.12}$$

$$H = \frac{EN + GL - 2FM}{2(EG - F^2)} \tag{5.13}$$

Alternatively, the Gaussian curvature K can be expressed as a function of E, F, G and their derivatives [52]. After substituting Equation (5.7) into Equation (5.9) and substituting Equation (5.9) into Equation (5.12), the Gaussian curvature is expressed as a function of triple scalar products of the derivatives of $\mathbf{r}$. These triple scalar products are then expressed by products of the partial derivatives of the first fundamental form coefficients, and the result is:

$$\begin{aligned} 4(EG - F^2)^2 K &= E\left(E_v G_v - 2F_u G_v + G_u^2\right) \\ &+ F\left(E_u G_v - E_v G_u - 2E_v F_v + 4E_u F_v - 2F_u G_u\right) \end{aligned}$$

$$+ \quad G\left(E_u G_u - 2E_u F_v + E_v^2\right) - 2(EG - F^2)\left(E_{vv} - 2F_{uv} + G_{uu}\right) \qquad (5.14)$$

5.2.2 Theorems on the gradients of the first fundamental form coefficients

In this section, some theorems are presented on the gradients of the first fundamental form coefficients of the offset surface along the offset distance direction, which correspond to the gradients of those coefficients across the thickness for a curved shell plate. These theorems show that the gradients of the first fundamental form coefficients of the offset surface provide the mechanism of surface curvature. In metal forming, this means that the non-uniformity of the tensile or compressive strains across the thickness generates surface curvature. The proofs of these results are presented in [64].

For a curved shell plate with thickness h, we consider $\mathbf{r}(u, v)$ as the mid-surface if its offset surfaces with signed distances $h/2$ and $-h/2$ are the upper and lower surfaces.

Theorem 5.2.1 *The coefficients of the second fundamental form of a parametric surface can be expressed by the derivatives of the coefficients of the first fundamental form of its offset surface $\hat{E}$, $\hat{F}$, $\hat{G}$ with respect to the offset distance d, evaluated at $d = 0$. i.e.,*

$$\left.\frac{\partial \hat{E}}{\partial d}\right|_{d=0} = -2L \qquad (5.15)$$

$$\left.\frac{\partial \hat{F}}{\partial d}\right|_{d=0} = -2M \qquad (5.16)$$

$$\left.\frac{\partial \hat{G}}{\partial d}\right|_{d=0} = -2N \qquad (5.17)$$

A similar result can be derived for the metrics along principal curvature directions.

Corollary 5.2.1 *Let the parameters along maximum principal curvature and mini-*

mum principal curvature directions be s and t. Then

$$\left.\frac{\partial(\hat{\mathbf{r}}_s \cdot \hat{\mathbf{r}}_s)}{\partial d}\right|_{d=0} = -2k_{max}(\hat{\mathbf{r}}_s \cdot \hat{\mathbf{r}}_s)|_{d=0} \tag{5.18}$$

$$\left.\frac{\partial(\hat{\mathbf{r}}_t \cdot \hat{\mathbf{r}}_t)}{\partial d}\right|_{d=0} = -2k_{min}(\hat{\mathbf{r}}_t \cdot \hat{\mathbf{r}}_t)|_{d=0} \tag{5.19}$$

Equations (5.15-5.17), (5.18, 5.19) play an important role in surface development algorithms, since in engineering applications, curved plates have finite thickness, no matter how thin they are.

5.3 Surface development along isoparametric directions

In this section, algorithms for surface development along isoparametric directions are presented. The process of surface development is expressed by tensile strains along u, v isoparametric directions. This corresponds to forming a plate into a curved surface only by shrinkage which can be realized by line heating process [49, 63].

5.3.1 Determination of strain field

Formulation

We assume that the surface is defined by a parametric vector equation of the form (5.1). The surface and its planar development are shown in Figure 5-2. The coefficients of the first fundamental form of the curved surface are given by Equation (5.3).

Assume that during metal forming by line heating, the normal strain along u line is $\epsilon^u(u,v) \leq 0$, and the normal strain along v line is $\epsilon^v(u,v) \leq 0$. On the contrary, the strains due to expansion from curved surface to its planar development are $\varepsilon^u(u,v) \geq 0$ and $\varepsilon^v(u,v) \geq 0$, as shown in Figure 5-3. Normal strains are a non-dimensional quantity defined by the ratio of extension or shrinkage of a fiber and its original length. After surface development a strain distribution $\varepsilon^u(u,v)$ along

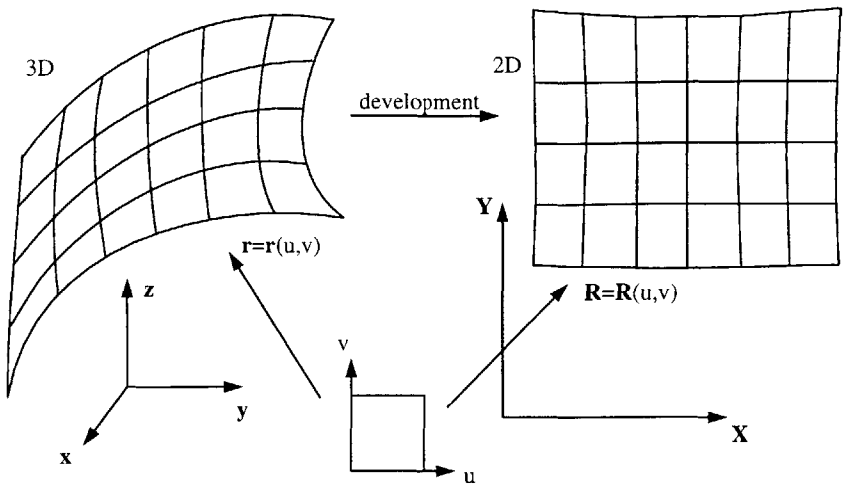

Figure 5-2: Curved surface and its planar development

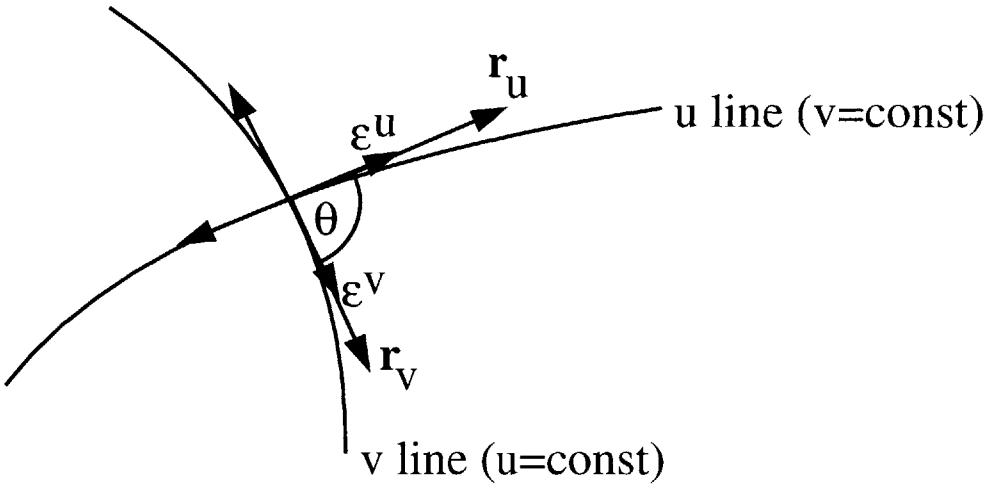

Figure 5-3: Strain distribution produced during surface development

isoparametric line $v = const$, and a strain distribution $\varepsilon^v(u, v)$ along isoparametric line $u = const$ are produced. Consequently an infinitesimal length $|\mathbf{r}_u du|$ changes to $(1 + \varepsilon^u)|\mathbf{r}_u du|$, and an infinitesimal length $|\mathbf{r}_v dv|$ changes to $(1 + \varepsilon^v)|\mathbf{r}_v dv|$, according to the definition of strain. Thus we have

$$|\mathbf{R}_u| = (1 + \varepsilon^u)|\mathbf{r}_u|, \quad |\mathbf{R}_v| = (1 + \varepsilon^v)|\mathbf{r}_v| \tag{5.20}$$

where $\mathbf{R}(u, v)$ is the planar development (see Figure 5-2). The first fundamental form

coefficients of the developed surface $\mathbf{R}(u,v)$ are given by

$$e = \mathbf{R}_u \cdot \mathbf{R}_u, \quad f = \mathbf{R}_u \cdot \mathbf{R}_v, \quad g = \mathbf{R}_v \cdot \mathbf{R}_v \tag{5.21}$$

After substituting Equation (5.20) and the relations

$$\mathbf{R}_u \cdot \mathbf{R}_u = |\mathbf{R}_u|^2, \;\; \mathbf{R}_v \cdot \mathbf{R}_v = |\mathbf{R}_v|^2$$

into Equation (5.21), the coefficients of the first fundamental form of the planar developed surface are

$$e = (1+\varepsilon^u)^2 E, \quad f = (1+\varepsilon^u)(1+\varepsilon^v)F, \quad g = (1+\varepsilon^v)^2 G \tag{5.22}$$

Here, in computing f, we assume the angle between $\mathbf{r}_u$ and $\mathbf{r}_v$ does not change after surface development. This is equivalent to ignoring the effect of shear strain.

We then minimize the strains $\varepsilon^u(u,v)$ and $\varepsilon^v(u,v)$ which satisfy the condition that after adding these strains to the doubly curved surface, it maps to a planar shape on which Gaussian curvature is zero. This minimization is done in an integral sense using the squares of the strains. Using Equation (5.14), this results into

$$\begin{aligned} &\min \quad \int\int_D \{(\varepsilon^u)^2 + (\varepsilon^v)^2\} |\mathbf{r}_u \times \mathbf{r}_v| du dv = \\ &\min \quad \int\int_D \{(\varepsilon^u)^2 + (\varepsilon^v)^2\} \sqrt{EG - F^2}\, du dv \end{aligned} \tag{5.23}$$

$$\begin{aligned} \text{such that} \quad 0 \;=\; & \left\{ e \left(\frac{\partial e}{\partial v} \cdot \frac{\partial g}{\partial v} - 2\frac{\partial f}{\partial u} \cdot \frac{\partial g}{\partial v} + (\frac{\partial g}{\partial u})^2 \right) \right. \\ & + \; f \left(\frac{\partial e}{\partial u} \cdot \frac{\partial g}{\partial v} - \frac{\partial e}{\partial v} \cdot \frac{\partial g}{\partial u} - 2\frac{\partial e}{\partial v} \cdot \frac{\partial f}{\partial v} + 4\frac{\partial e}{\partial u} \cdot \frac{\partial f}{\partial v} - 2\frac{\partial f}{\partial u} \cdot \frac{\partial g}{\partial u} \right) \\ & + \; g \left(\frac{\partial e}{\partial u} \cdot \frac{\partial g}{\partial u} - 2\frac{\partial e}{\partial u} \cdot \frac{\partial f}{\partial v} + (\frac{\partial e}{\partial v})^2 \right) \\ & - \; \left. 2(eg - f^2) \left(\frac{\partial^2 e}{\partial v^2} - 2\frac{\partial^2 f}{\partial u \partial v} + \frac{\partial^2 g}{\partial u^2} \right) \right\} / 4(eg - f^2)^2 \end{aligned} \tag{5.24}$$

$$\varepsilon^u(u,v) \geq 0; \varepsilon^v(u,v) \geq 0; (u,v) \in D$$

where D denotes the parametric domain. The objective function is a measure of energy due to stretching and is used in the area of deformable surface design [9]. We keep the denominator in Equation (5.24) (i.e. $4(eg - f^2)^2$) so that the constraint essentially forces the Gaussian curvature to be zero. It can be shown that minimizing the strains $\varepsilon^u(u,v)$ and $\varepsilon^v(u,v)$ is equivalent to minimizing the magnitude of the strains $\epsilon^u(u,v)$ and $\epsilon^v(u,v)$. We choose to work with $\varepsilon^u(u,v)$ and $\varepsilon^v(u,v)$ since we are starting from the curved design surface.

Alternatively, we can also use $(\varepsilon^u + \varepsilon^v)$ instead of $\{(\varepsilon^u)^2 + (\varepsilon^v)^2\}$ in the above integral objective function. In this case, the objective function represents the area difference between the doubly curved surface and the planar development to the first order. We use the quadratic objective function $\{(\varepsilon^u)^2+(\varepsilon^v)^2\}$ here instead of the linear one to make the solution easier. After substituting Equations (5.22) into the above formulae, we obtain an optimization problem with respect to $\varepsilon^u(u,v)$ and $\varepsilon^v(u,v)$.

This constrained minimization problem is discretized by using the finite difference method and trapezoidal rule of integration. A grid of $N_g^u \times N_g^v$ points in the parametric domain are used in the discretization. Therefore, the total number of variables is $2N_g^u N_g^v$. To guarantee the independence of each constraint, constraints are imposed at the internal points of the grid, so there are $(N_g^u - 2) \times (N_g^v - 2)$ constraints.

After discretization, the objective function becomes

$$\sum_{i=1}^{N_g^u} \sum_{j=1}^{N_g^v} \alpha_{ij}((\varepsilon_{ij}^u)^2 + (\varepsilon_{ij}^v)^2)\sqrt{E_{ij}G_{i,j} - F_{ij}^2}\Delta u \Delta v \tag{5.25}$$

where following the trapezoid rule of integration [11]

$$\begin{cases} \alpha_{ij} = 1 & \text{when } 1 < i < N_g^u;\ 1 < j < N_g^v \\ \alpha_{ij} = 0.5 & \text{when } 1 < i < N_g^u;\ j = 1 \text{ or } j = N_g^v \\ \alpha_{ij} = 0.5 & \text{when } i = 1 \text{ or } i = N_g^u;\ 1 < j < N_g^v \\ \alpha_{ij} = 0.25 & \text{when } i = j = 0 \text{ or } i = N_g^u, j = N_g^v \\ \alpha_{ij} = 0.25 & \text{when } i = N_g^u, j = 0 \text{ or } i = 0, j = N_g^v \end{cases} \tag{5.26}$$

As $\Delta u, \Delta v \to 0$, the error between the objective functions in (5.23) and (5.25) due to numerical integration is $O((\Delta u)^2, (\Delta v)^2)$ as is well known [11].

We use the central difference method to approximate all the derivatives in Equation (5.24) at internal points of the grid.

$$\frac{\partial e}{\partial u}|_{ij} = \frac{(1+\varepsilon^u_{i+1,j})^2 E_{i+1,j} - (1+\varepsilon^u_{i-1,j})^2 E_{i-1,j}}{2\Delta u} \tag{5.27}$$

$$\frac{\partial e}{\partial v}|_{ij} = \frac{(1+\varepsilon^u_{i,j+1})^2 E_{i,j+1} - (1+\varepsilon^u_{i,j-1})^2 E_{i,j-1}}{2\Delta v} \tag{5.28}$$

$$\frac{\partial f}{\partial u}|_{ij} = \frac{(1+\varepsilon^u_{i+1,j})(1+\varepsilon^v_{i+1,j}) F_{i+1,j} - (1+\varepsilon^u_{i-1,j})(1+\varepsilon^v_{i-1,j}) F_{i-1,j}}{2\Delta u} \tag{5.29}$$

$$\frac{\partial f}{\partial v}|_{ij} = \frac{(1+\varepsilon^u_{i,j+1})(1+\varepsilon^v_{i,j+1}) F_{i,j+1} - (1+\varepsilon^u_{i,j-1})(1+\varepsilon^v_{i,j-1}) F_{i,j-1}}{2\Delta v} \tag{5.30}$$

$$\frac{\partial g}{\partial u}|_{ij} = \frac{(1+\varepsilon^v_{i+1,j})^2 G_{i+1,j} - (1+\varepsilon^v_{i-1,j})^2 G_{i-1,j}}{2\Delta u} \tag{5.31}$$

$$\frac{\partial g}{\partial v}|_{ij} = \frac{(1+\varepsilon^v_{i,j+1})^2 G_{i,j+1} - (1+\varepsilon^v_{i,j-1})^2 G_{i,j-1}}{2\Delta v} \tag{5.32}$$

$$\frac{\partial^2 e}{\partial v^2}|_{ij} = \frac{(1+\varepsilon^u_{i,j+1})^2 E_{i,j+1} - 2(1+\varepsilon^u_{i,j})^2 E_{i,j} + (1+\varepsilon^u_{i,j-1})^2 E_{i,j-1}}{(\Delta v)^2} \tag{5.33}$$

$$\frac{\partial^2 f}{\partial u \partial v}|_{ij} = \frac{(1+\varepsilon^u_{i+1,j+1})(1+\varepsilon^v_{i+1,j+1}) F_{i+1,j+1} + (1+\varepsilon^u_{i-1,j-1})(1+\varepsilon^v_{i-1,j-1}) F_{i-1,j-1}}{4\Delta u \Delta v} - \frac{(1+\varepsilon^u_{i-1,j+1})(1+\varepsilon^v_{i-1,j+1}) F_{i-1,j+1} + (1+\varepsilon^u_{i+1,j-1})(1+\varepsilon^v_{i+1,j-1}) F_{i+1,j-1}}{4\Delta u \Delta v} \tag{5.34}$$

$$\frac{\partial^2 g}{\partial u^2}|_{ij} = \frac{(1+\varepsilon^v_{i+1,j})^2 G_{i+1,j} - 2(1+\varepsilon^v_{i,j})^2 G_{i,j} + (1+\varepsilon^v_{i-1,j})^2 G_{i-1,j}}{(\Delta u)^2} \tag{5.35}$$

As $\Delta u, \Delta v \to 0$, the errors in Equations (5.27)-(5.35) due to central difference approximation are of the order $(\Delta u)^2$ or $(\Delta v)^2$, or $\Delta u \cdot \Delta v$ as is well known [11].

After discretization, we obtain a nonlinear optimization problem with a convex

cost function and nonlinear polynomial constraints. This nonlinear programming problem is solved by using the Fortran NAG routine E04VDF [42], which is designed to solve the nonlinear programming problem – the minimization of a smooth nonlinear function subject to a set of constraints on the variables.

Strain gradients

After solving for the strain distribution at the mid-surface, we can determine the ideal gradient of the strains along the normal of the mid-surface. As mentioned in Section 2, the strain gradients provide the mechanism of surface curvature in metal forming process. Based on Equation (5.22), and

$$F = \mathbf{r}_u \cdot \mathbf{r}_v = |\mathbf{r}_u||\mathbf{r}_v| \cos\theta = \sqrt{E}\sqrt{G}\cos\theta \tag{5.36}$$

where θ is the angle between $\mathbf{r}_u$ and $\mathbf{r}_v$, the coefficients of the first fundamental form of the planar developed shape of the offset surface at distance d from the mid-surface are:

$$\hat{e} = (1+\hat{\varepsilon}^u)^2\hat{E}, \quad \hat{f} = (1+\hat{\varepsilon}^u)(1+\hat{\varepsilon}^v)\sqrt{\hat{E}\hat{G}}\cos(\hat{\theta}+\Delta\theta), \quad \hat{g} = (1+\hat{\varepsilon}^v)^2\hat{G} \tag{5.37}$$

where $\hat{E}, \hat{F}, \hat{G}$ are the coefficients of the first fundamental form of the offset surface; $\hat{e}, \hat{f}, \hat{g}$ are the coefficients of the first fundamental form of the planar developed shape of the offset surface; $\hat{\theta}$ is the angle between isoparametric lines $u = const$ and $v = const$ on the offset surface; $\Delta\theta$ is the change of this angle after development. According to the assumption in this section, $\Delta\theta = 0$ at $d = 0$. Ideally, after development, the 2D developed shape of the offset surface is the same for any given offset distance d, thus we have

$$\frac{\partial \hat{e}}{\partial d} = 0 \tag{5.38}$$

$$\frac{\partial \hat{f}}{\partial d} = 0 \tag{5.39}$$

$$\frac{\partial \hat{g}}{\partial d} = 0 \tag{5.40}$$

After substituting $\hat{e}$ in Equation (5.37) into Equation (5.38), we have

$$2\hat{E}(1+\hat{\varepsilon}^u)\frac{\partial(1+\hat{\varepsilon}^u)}{\partial d}+(1+\hat{\varepsilon}^u)^2\frac{\partial\hat{E}}{\partial d}=0 \tag{5.41}$$

After dividing the above equation by $(1+\hat{\varepsilon}^u)$ and using Equation (5.15), at $d=0$,

$$2E\frac{\partial(1+\varepsilon^u)}{\partial d}\bigg|_{d=0}+(1+\varepsilon^u)(-2L)=0, \tag{5.42}$$

so

$$\frac{\partial[\ln(1+\varepsilon^u)]}{\partial d}\bigg|_{d=0}=\frac{L}{E} \tag{5.43}$$

Similarly, Equation (5.40) leads to

$$\frac{\partial[\ln(1+\varepsilon^v)]}{\partial d}\bigg|_{d=0}=\frac{N}{G} \tag{5.44}$$

After substituting $\hat{f}$ in Equation (5.37) into Equation (5.39), we obtain

$$\sqrt{\hat{E}\hat{G}}\cos(\hat{\theta}+\Delta\theta)\frac{\partial[(1+\hat{\varepsilon}^u)(1+\hat{\varepsilon}^v)]}{\partial d}+(1+\hat{\varepsilon}^u)(1+\hat{\varepsilon}^v)\frac{\partial\left(\sqrt{\hat{E}\hat{G}}\cos(\hat{\theta}+\Delta\theta)\right)}{\partial d}=0 \tag{5.45}$$

At $d=0$, the above equation results in

$$\sqrt{EG}\cos\theta\frac{\partial[(1+\varepsilon^u)(1+\varepsilon^v)]}{\partial d}\bigg|_{d=0}+(1+\varepsilon^u)(1+\varepsilon^v)\frac{\partial\left(\sqrt{\hat{E}\hat{G}}\cos(\hat{\theta}+\Delta\theta)\right)}{\partial d}\bigg|_{d=0}=0 \tag{5.46}$$

Since

$$\begin{aligned}\frac{\partial\left(\sqrt{\hat{E}\hat{G}}\cos(\hat{\theta}+\Delta\theta)\right)}{\partial d}\bigg|_{d=0} &= \frac{\partial\left(\sqrt{\hat{E}\hat{G}}\cos\hat{\theta}\cos\Delta\theta-\sqrt{\hat{E}\hat{G}}\sin\hat{\theta}\sin\Delta\theta\right)}{\partial d}\bigg|_{d=0}\\ &= \frac{\partial(\hat{F}\cos\Delta\theta)}{\partial d}\bigg|_{d=0}-\frac{\partial(\hat{F}\tan\hat{\theta}\sin\Delta\theta)}{\partial d}\bigg|_{d=0}\\ &= \frac{\partial\hat{F}}{\partial d}\cos\Delta\theta\bigg|_{d=0}-\hat{F}\sin\Delta\theta\frac{\partial(\Delta\theta)}{\partial d}\bigg|_{d=0}\end{aligned}$$

$$
\begin{aligned}
&- \hat{F}\tan\hat{\theta}\cos\Delta\theta\frac{\partial(\Delta\theta)}{\partial d}\bigg|_{d=0} - \frac{\partial(\hat{F}\tan\hat{\theta})}{\partial d}\sin\Delta\theta\bigg|_{d=0} \\
&= -2M - F\tan\theta\frac{\partial(\Delta\theta)}{\partial d}\bigg|_{d=0} \qquad (5.47)
\end{aligned}
$$

from Equation (5.46), we have

$$
F\frac{\partial[(1+\varepsilon^u)(1+\varepsilon^v)]}{\partial d}\bigg|_{d=0} + (1+\varepsilon^u)(1+\varepsilon^v)\left(-2M - F\tan\theta\frac{\partial(\Delta\theta)}{\partial d}\bigg|_{d=0}\right) = 0 \quad (5.48)
$$

or equivalently,

$$
\frac{\partial[\ln(1+\varepsilon^u)+\ln(1+\varepsilon^v)]}{\partial d}\bigg|_{d=0} = \frac{2M}{F} + \tan\theta\frac{\partial(\Delta\theta)}{\partial d}\bigg|_{d=0} \qquad (5.49)
$$

During the derivation of Equation (5.47), Equation (5.16) is used, as well as the relation

$$
\Delta\theta|_{d=0} = 0
$$

After substituting Equations (5.43, 5.44) into Equation (5.49), we obtain

$$
\frac{\partial(\Delta\theta)}{\partial d}\bigg|_{d=0} = \cot\theta\left(\frac{L}{E} + \frac{N}{G} - \frac{2M}{F}\right) \qquad (5.50)
$$

The system of equations (5.43, 5.44, 5.50) give out ideal strain gradients, and the gradient of change of angle between isoparametric directions. In other words, if the strain gradients of $\ln(1+\varepsilon^u)$ and $\ln(1+\varepsilon^v)$ at $d = 0$ are equal to the ratios of the corresponding second and first fundamental form coefficients at the mid-surface before development, and the gradient of $\Delta\theta$ at $d = 0$ satisfy the relation (5.50), the 2D developed shape of the offset surface with small offset distance will be the same.

5.3.2 Determination of planar developed shape

After solving the nonlinear minimization problem, we obtain the strains ε^u and ε^v at all grid points. We now determine the planar coordinates (X_{ij}, Y_{ij}) of the grid points at the corresponding planar development. Ideally, these coordinates (X_{ij}, Y_{ij}) should

satisfy the following equations at all grid points:

$$\mathbf{R}_u \cdot \mathbf{R}_u = e, \;\; \mathbf{R}_u \cdot \mathbf{R}_v = f, \;\; \mathbf{R}_v \cdot \mathbf{R}_v = g \tag{5.51}$$

where $\mathbf{R} = (X, Y)$, and e, f, g are obtained from Equation (5.22) as functions of u and v. Equations (5.51) can be expressed as

$$\begin{aligned} X_u^2 + Y_u^2 &= e \\ X_u X_v + Y_u Y_v &= f \\ X_v^2 + Y_v^2 &= g \end{aligned} \tag{5.52}$$

After discretization of the above equations (5.52) using finite difference method (central difference for internal points, and forward or backward difference for boundary points), we obtain a system of over-determined nonlinear polynomial equations. Instead of solving the system directly, we solve the following least squares error unconstrained minimization problem

$$\min \sum_{i=1}^{N_g^u} \sum_{j=1}^{N_g^v} (\mathbf{R}_u \cdot \mathbf{R}_u|_{ij} - e_{ij})^2 + (\mathbf{R}_u \cdot \mathbf{R}_v|_{ij} - f_{ij})^2 + (\mathbf{R}_v \cdot \mathbf{R}_v|_{ij} - g_{ij})^2 \tag{5.53}$$

This optimization problem can be solved by using the quasi-Newton method [4] for finding an unconstrained minimization of a sum-of-squares of M_1 nonlinear functions in M_2 variables ($M_1 \geq M_2$). This can be done by using the NAG Fortran library routine E04GBF [42]. In the implementation, rigid body motion of the developed planar shape is prohibited by forcing the coordinates of the grid points:

$$(X_{ij}, Y_{ij})|_{(i=0,j=0)} = (0, 0), \;\; \text{and} \;\; X_{ij}|_{(i=0,j=1)} = 0$$

The starting points of the minimization are given by

$$(X_{ij}, Y_{ij}) = (\frac{i}{N_g^u}, \frac{j}{N_g^v})\beta \quad (i = 1, ..., N_g^u; j = 1, ..., N_g^v)$$

where β is a scalar factor.

5.4 Surface development along principal curvature directions

In section 5.3, surface development is expressed by tensile strains along the isoparametric lines. The assumption made is that the angle between isoparametric directions remains unchanged after a doubly curved surface is developed into a two-dimensional shape. This assumption is reasonable when the angle between isoparametric directions is large and the strains are small. In the case when the angle between $\mathbf{r}_u$ and $\mathbf{r}_v$ is small at some area of the surface, this assumption may cause errors which can not be ignored.

In this section, algorithms for surface development based on strains along principal curvature directions are presented. Since the principal curvature directions are independent of the parametrization of surfaces and are unique except at umbilic points, this surface development is more general. Also, since the angle between two principal curvature directions is a right angle, the assumption that this angle does not change significantly after development is more reasonable.

5.4.1 Determination of strain field

We assume that the surface is defined by the parametric vector equation (5.1). The surface and its planar development are shown in Figure 5-2. The coefficients of the first fundamental form of the curved surface are given by Equation (5.3). We further assume that during the surface development process, the strains due to expansion from curved surface to its planar development are $\varepsilon^s(u,v) \geq 0$ and $\varepsilon^t(u,v) \geq 0$, along the maximum and minimum principal curvature directions, respectively. Therefore an infinitesimal length $|\mathbf{r}_s ds|$ changes to $(1+\varepsilon^s)|\mathbf{r}_s ds|$, and an infinitesimal length

$|\mathbf{r}_t dt|$ changes to $(1+\varepsilon^t)|\mathbf{r}_t dt|$, according to the definition of strain. Thus we have

$$|\mathbf{R}_s| = (1+\varepsilon^s)|\mathbf{r}_s|, \quad |\mathbf{R}_t| = (1+\varepsilon^t)|\mathbf{r}_t| \tag{5.54}$$

where $\mathbf{R}(u,v)$ is the planar development. $\mathbf{R}(u,v)$ can also be considered as a parametric surface with its first fundamental form coefficients defined by Equation (5.21). Since

$$\begin{aligned} \mathbf{R}_s \cdot \mathbf{R}_s &= (\mathbf{R}_u u_s + \mathbf{R}_v v_s) \cdot (\mathbf{R}_u u_s + \mathbf{R}_v v_s) \\ &= e u_s^2 + 2 f u_s v_s + g v_s^2 \end{aligned} \tag{5.55}$$

and

$$\begin{aligned} \mathbf{r}_s \cdot \mathbf{r}_s &= (\mathbf{r}_u u_s + \mathbf{r}_v v_s) \cdot (\mathbf{r}_u u_s + \mathbf{r}_v v_s) \\ &= E u_s^2 + 2 F u_s v_s + G v_s^2 \end{aligned} \tag{5.56}$$

using the relations in Equation (5.54, 5.55, 5.56), we obtain

$$e u_s^2 + 2 f u_s v_s + g v_s^2 = (1+\varepsilon^s)^2 (E u_s^2 + 2 F u_s v_s + G v_s^2) \tag{5.57}$$

Similarly, along minimum principal curvature direction, we have

$$e u_t^2 + 2 f u_t v_t + g v_t^2 = (1+\varepsilon^t)^2 (E u_t^2 + 2 F u_t v_t + G v_t^2) \tag{5.58}$$

We also assume that after development, the principal curvature directions remain orthogonal, which gives

$$\mathbf{R}_s \cdot \mathbf{R}_t = (\mathbf{R}_u u_s + \mathbf{R}_v v_s) \cdot (\mathbf{R}_u u_t + \mathbf{R}_v v_t) = 0 \tag{5.59}$$

Simplifying the above equation gives

$$e u_s u_t + f(u_s v_t + u_t v_s) + g v_s v_t = 0 \tag{5.60}$$

Then we have a system of three linear equations (5.57, 5.58, 5.60) in e, f, g whose solution is given by

$$e = \frac{v_t^2\left[Eu_s^2+2Fu_sv_s+Gv_s^2\right](1+\varepsilon^s)^2+v_s^2\left[Eu_t^2+2Fu_tv_t+Gv_t^2\right](1+\varepsilon^t)^2}{(v_su_t-u_sv_t)^2} \quad (5.61)$$

$$f = -\frac{u_tv_t\left[Eu_s^2+2Fu_sv_s+Gv_s^2\right](1+\varepsilon^s)^2+u_sv_s\left[Eu_t^2+2Fu_tv_t+Gv_t^2\right](1+\varepsilon^t)^2}{(v_su_t-u_sv_t)^2} \quad (5.62)$$

$$g = \frac{u_t^2\left[Eu_s^2+2Fu_sv_s+Gv_s^2\right](1+\varepsilon^s)^2+u_s^2\left[Eu_t^2+2Fu_tv_t+Gv_t^2\right](1+\varepsilon^t)^2}{(v_su_t-u_sv_t)^2} \quad (5.63)$$

We minimize the strains $\varepsilon^s(u,v)$ and $\varepsilon^t(u,v)$ which satisfy the condition that after adding these strains to the doubly curved surface along principal curvature directions, the surface maps to a planar shape on which Gaussian curvature is zero. Using Equation (5.14), this results into

$$\begin{aligned} &\min && \int\int_D\{(\varepsilon^s)^2+(\varepsilon^t)^2\}|\mathbf{r}_u\times\mathbf{r}_v|dudv = \\ &\min && \int\int_D\{(\varepsilon^s)^2+(\varepsilon^t)^2\}\sqrt{EG-F^2}dudv \end{aligned} \quad (5.64)$$

$$\begin{aligned} \text{such that}\quad 0 &= \left\{e\left(\frac{\partial e}{\partial v}\cdot\frac{\partial g}{\partial v}-2\frac{\partial f}{\partial u}\cdot\frac{\partial g}{\partial v}+(\frac{\partial g}{\partial u})^2\right)\right. \\ &+ f\left(\frac{\partial e}{\partial u}\cdot\frac{\partial g}{\partial v}-\frac{\partial e}{\partial v}\cdot\frac{\partial g}{\partial u}-2\frac{\partial e}{\partial v}\cdot\frac{\partial f}{\partial v}+4\frac{\partial e}{\partial u}\cdot\frac{\partial f}{\partial v}-2\frac{\partial f}{\partial u}\cdot\frac{\partial g}{\partial u}\right) \\ &+ g\left(\frac{\partial e}{\partial u}\cdot\frac{\partial g}{\partial u}-2\frac{\partial e}{\partial u}\cdot\frac{\partial f}{\partial v}+(\frac{\partial e}{\partial v})^2\right) \\ &- \left.2(eg-f^2)\left(\frac{\partial^2 e}{\partial v^2}-2\frac{\partial^2 f}{\partial u\partial v}+\frac{\partial^2 g}{\partial u^2}\right)\right\}/4(eg-f^2)^2 \\ &\varepsilon^s(u,v)\geq 0;\varepsilon^t(u,v)\geq 0;(u,v)\in D \end{aligned} \quad (5.65)$$

where D denotes the parametric domain. After substituting Equations (5.61-5.63) into the above formulae, we obtain an optimization problem with respect to $\varepsilon^s(u,v)$ and $\varepsilon^t(u,v)$. As shown in Section 5.3, this constrained minimization problem is discretized by using the finite difference method and trapezoidal rule of integration. The final formulation is similar to that in Section 5.3 except that $\varepsilon^u, \varepsilon^v$ are replaced

by $\varepsilon^s, \varepsilon^t$. Again, the nonlinear constrained minimization problem is solved by using the Fortran NAG routine E04VDF [42].

5.4.2 Strain gradients

After solving for the strain distribution at the mid-surface, we then can determine the ideal gradient of the strains along the normal of the mid-surface. As mentioned in Section 2, the strain gradients provide the mechanism of surface curvature in metal forming process. Based on Equations (5.57, 5.58), the relations of the first fundamental form coefficients of the offset surface of distance d along the normal from the mid-surface are:

$$\hat{e}u_s^2 + 2\hat{f}u_s v_s + \hat{g}v_s^2 = (1+\hat{\varepsilon}^s)^2(\hat{E}u_s^2 + 2\hat{F}u_s v_s + \hat{G}v_s^2) \tag{5.66}$$

$$\hat{e}u_t^2 + 2\hat{f}u_t v_t + \hat{g}v_t^2 = (1+\hat{\varepsilon}^t)^2(\hat{E}u_t^2 + 2\hat{F}u_t v_t + \hat{G}v_t^2) \tag{5.67}$$

Since after development, the 2D shape is the same across the thickness, we have

$$\frac{\partial(\hat{e}u_s^2 + 2\hat{f}u_s v_s + \hat{g}v_s^2)}{\partial d} = 0 \tag{5.68}$$

$$\frac{\partial(\hat{e}u_t^2 + 2\hat{f}u_t v_t + \hat{g}v_t^2)}{\partial d} = 0 \tag{5.69}$$

After substituting Equation (5.66) into Equation (5.68), we have

$$\frac{\partial}{\partial d}\left((1+\hat{\varepsilon}^s)^2(\hat{\mathbf{r}}_s \cdot \hat{\mathbf{r}}_s)\right) = 0 \tag{5.70}$$

Expanding the above equation, we obtain at $d = 0$,

$$2(1+\varepsilon^s)\frac{\partial(1+\varepsilon^s)}{\partial d}(\hat{\mathbf{r}}_s \cdot \hat{\mathbf{r}}_s)\Big|_{d=0} + (1+\varepsilon^s)^2\frac{\partial(\hat{\mathbf{r}}_s \cdot \hat{\mathbf{r}}_s)}{\partial d}\Big|_{d=0} = 0 \tag{5.71}$$

This results in

$$\frac{\partial[\ln(1+\varepsilon^s)]}{\partial d}\Big|_{d=0} = -\frac{1}{2\hat{\mathbf{r}}_s \cdot \hat{\mathbf{r}}_s}\frac{\partial(\hat{\mathbf{r}}_s \cdot \hat{\mathbf{r}}_s)}{\partial d}\Big|_{d=0} = \kappa_{max} \tag{5.72}$$

The last equality comes from Equation (5.18). Similarly,

$$\left.\frac{\partial[\ln(1+\varepsilon^t)]}{\partial d}\right|_{d=0} = -\frac{1}{2\hat{\mathbf{r}}_t \cdot \hat{\mathbf{r}}_t}\left.\frac{\partial(\hat{\mathbf{r}}_t \cdot \hat{\mathbf{r}}_t)}{\partial d}\right|_{d=0} = \kappa_{min} \tag{5.73}$$

For the special case when the strain gradient is constant across the thickness, and the strains ε^s, ε^t are small, Equations (5.72) and (5.73) represent the Kirchhoff assumption in plate theory [13]. To show this, consider an explicit surface represented by the height function $z = h(x, y)$. Its Gauss and mean curvatures are [45]

$$K = \frac{h_{xx}h_{yy} - h_{xy}^2}{(1 + h_x^2 + h_y^2)^2} \tag{5.74}$$

$$H = \frac{(1 + h_x^2)h_{yy} - 2h_x h_y h_{xy} + (1 + h_y^2)h_{xx}}{2(1 + h_x^2 + h_y^2)^{3/2}} \tag{5.75}$$

For small deformation, $h_x << 1$ and $h_y << 1$. After omitting higher order terms in Equations (5.74) and (5.75), we obtain the Gauss curvature and mean curvature

$$K \simeq h_{xx}h_{yy} - h_{xy}^2 \tag{5.76}$$

$$H \simeq \frac{h_{xx} + h_{yy}}{2} \tag{5.77}$$

Therefore, the maximum and minimum principal curvatures [45] are

$$\kappa_{max} \simeq H + \sqrt{H^2 - K} = \frac{h_{xx} + h_{yy}}{2} + \sqrt{\left(\frac{h_{xx} - h_{yy}}{2}\right)^2 + h_{xy}^2} \tag{5.78}$$

$$\kappa_{min} \simeq H - \sqrt{H^2 - K} = \frac{h_{xx} + h_{yy}}{2} - \sqrt{\left(\frac{h_{xx} - h_{yy}}{2}\right)^2 + h_{xy}^2} \tag{5.79}$$

Denote ϵ^s, ϵ^t the strains from the planar shape to the doubly curved surface due to the forming process, then we have the following relationships

$$1 + \varepsilon^s = \frac{1}{1 + \epsilon^s} \tag{5.80}$$

$$1 + \varepsilon^t = \frac{1}{1 + \epsilon^t} \tag{5.81}$$

After substituting Equation (5.80) into Equation (5.72), and taking account the assumption of small strains, we obtain

$$\left.\frac{\partial \epsilon^s}{\partial d}\right|_{d=0} = -\kappa_{max} \tag{5.82}$$

And, for constant strain gradient across thickness

$$\epsilon^s = -\kappa_{max} d = -\left(\frac{h_{xx} + h_{yy}}{2} + \sqrt{\left(\frac{h_{xx} - h_{yy}}{2} \right)^2 + h_{xy}^2} \right) d + c_s \tag{5.83}$$

where the first term in the above equation represents the strain due to bending, and c_s represents the strain due to inplane deformation. Similarly, in the other principal curvature direction,

$$\epsilon^t = -\kappa_{max} d = -\left(\frac{h_{xx} + h_{yy}}{2} - \sqrt{\left(\frac{h_{xx} - h_{yy}}{2} \right)^2 + h_{xy}^2} \right) d + c_t \tag{5.84}$$

On the other hand, from the thin plate theory under the Kirchhoff assumption [13], the strains due to bending are

$$\begin{Bmatrix} \epsilon_{xx} \\ \epsilon_{yy} \\ \epsilon_{xy} \end{Bmatrix} = -d \begin{Bmatrix} h_{xx} \\ h_{yy} \\ h_{xy} \end{Bmatrix} \tag{5.85}$$

The maximum principal strain in magnitude is

$$\epsilon_a = -\left(\frac{h_{xx} + h_{yy}}{2} + \sqrt{\left(\frac{h_{xx} - h_{yy}}{2} \right)^2 + h_{xy}^2} \right) d \tag{5.86}$$

which is exactly the same as the bending strain part of ϵ^s in Equation (5.83) obtained from surface development.

Next, we verify that the directions of the principal bending strains are those of

principal curvatures. The directions $\lambda = \frac{dy}{dx}$ of the principal curvatures satisfy [45]

$$\kappa_n = \frac{L + 2M\lambda + N\lambda^2}{E + 2F\lambda + G\lambda^2} = \frac{L + M\lambda}{E + F\lambda} = \frac{M + N\lambda}{F + G\lambda} \tag{5.87}$$

where for the implicit surface

$$E = 1 + h_x^2 \quad F = h_x h_y \quad G = 1 + h_y^2$$

$$L = \frac{h_{xx}}{\sqrt{1 + h_x^2 + h_y^2}} \quad M = \frac{h_{xy}}{\sqrt{1 + h_x^2 + h_y^2}} \quad N = \frac{h_{yy}}{\sqrt{1 + h_x^2 + h_y^2}}$$

We solve Equation (5.87) for λ. After omitting the lower order terms in E, F, G, L, M, N, we obtain the principal curvature direction

$$\tan\theta = \frac{dy}{dx} = \frac{E\kappa_n - L}{M - F\kappa_n} = \frac{\kappa_n - h_{xx}}{h_{xy} - h_x h_y \kappa_n} = -\frac{h_{xx} - h_{yy}}{2h_{xy}} \pm \sqrt{1 + \left(\frac{h_{xx} - h_{yy}}{2h_{xy}}\right)^2} \tag{5.88}$$

On the other hand, from thin plate theory [13], the maximum strain direction satisfies

$$\tan 2\theta = \frac{2\tan\theta}{1 - \tan^2\theta} = \frac{2\epsilon_{xy}}{\epsilon_{xx} - \epsilon_{yy}} = \frac{2h_{xy}}{h_{xx} - h_{yy}} \tag{5.89}$$

Solving the above equation for $\tan\theta$, we obtain

$$\tan\theta = -\frac{h_{xx} - h_{yy}}{2h_{xy}} \pm \sqrt{1 + \left(\frac{h_{xx} - h_{yy}}{2h_{xy}}\right)^2} \tag{5.90}$$

Therefore, the directions of principal strain due to bending are the same as the principal curvature directions, and Equations (5.72) and (5.73) represent the Kirchhoff assumption in plate theory. From the surface development along principal curvature directions, the principal inplane strains are also along the principal curvature directions. Therefore, the resulting inplane strains and bending strains have the same principal directions, facilitating the planning of the forming process.

5.4.3 Determination of planar developed shape

After solving the nonlinear minimization problem (5.64 – 5.65), we obtain the strains ε^s and ε^t at all grid points. The first fundamental form coefficients e, f, g of the planar developed shape is then obtained from Equations (5.61 – 5.63). The method in Section 5.3.2 can be used to determine the planar developed shape.

5.5 Comparison of results

In this section, we demonstrate how the algorithms of Chapter 5 work for surface development based on strains along isoparametric lines and along lines of curvature. The surfaces in the examples include surfaces with all elliptical points (positive Gaussian curvature), surfaces with all hyperbolic points (negative Gaussian curvature), and more complex surfaces that have both positive and negative Gaussian curvature regions. Then the results are compared with those from isometric development and those from development by using FEM. All examples were executed on a graphics workstation running at 200 MHz.

5.5.1 Results from optimal development

Example 1

An elliptical bicubic Bézier surface $\mathbf{r}(u,v) = \sum_{i=0}^{3}\sum_{j=0}^{3}\mathbf{r}_{ij}B_{i,3}(u)B_{j,3}(v)$ with the following control points:

$$\begin{array}{cccc}
(0,0,0) & (0,1/3,0.15) & (0,2/3,0.15) & (0,1,0) \\
(1/3,0,0.25) & (1/3,1/3,0.5) & (1/3,2/3,0.5) & (1/3,1,0.25) \\
(2/3,0,0.25) & (2/3,1/3,0.5) & (2/3,2/3,0.5) & (2/3,1,0.25) \\
(1,0,0) & (1,1/3,0.15) & (1,2/3,0.15) & (1,1,0)
\end{array}$$

The surface along with its control polygon is shown in Figure 5-4. The constrained minimization problem (5.23-5.24) or (5.64-5.65) is discretized at 13×13 grid points which are equally distributed in u, v domain.

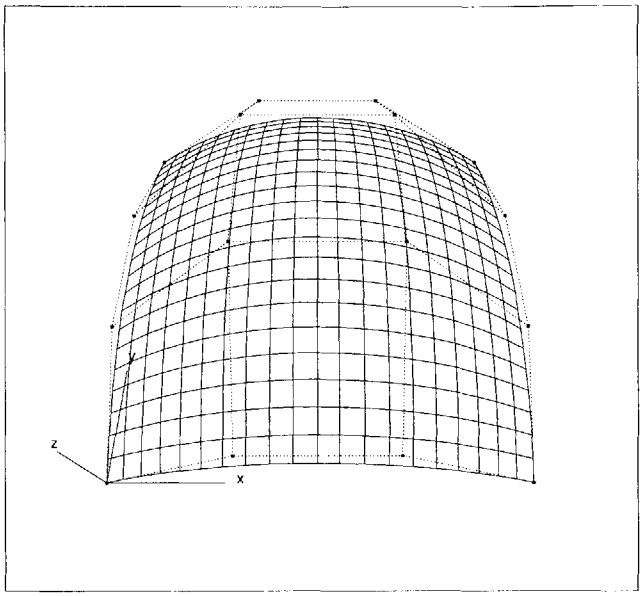

Figure 5-4: The bi-cubic Bézier surface in Example 1

Results from surface development along isoparametric lines

Figure 5-5 shows the strain distribution after the constrained minimization problem was solved using tolerances of 10^{-5} for the constraints and 10^{-4} for the objective function. The strains are scaled to fit into the figure. The extreme values of the strain field are located at $(u, v) = (0, 0.5)$ or $(u, v) = (1.0, 0.5)$ with $(\varepsilon^u, \varepsilon^v) = (0.0012101, 0.203391)$, and at $(u, v) = (0.5, 0)$ or $(u, v) = (0.5, 1.0)$ with $(\varepsilon^u, \varepsilon^v) = (0.242961, 0.00136569)$. The objective function converges to the value of 6.3857×10^{-3} at the solution, and all the constraints are within the tolerance of 1.0×10^{-5}.

After development, the planar shape is shown in Figure 5-6. The four corner points have coordinates of (0,0), (-0.14799,1.10615), (1.18199,0.15838), (1.03399,1.26452) respectively. The final value of the formula (5.53) is less than 10^{-4} times $\sum_{i=1}^{N_g^u} \sum_{j=1}^{N_g^v} (e_{ij}^2 + f_{ij}^2 + g_{ij}^2)$, the sum of the squares of the right side of system (5.52) at all grid points.

Figures 5-7 and 5-8 show the ideal strain gradients $\frac{\partial[\ln(1+\varepsilon^u)]}{\partial d}\Big|_{d=0}$ and $\frac{\partial[\ln(1+\varepsilon^v)]}{\partial d}\Big|_{d=0}$ evaluated at grid points such that the first fundamental form coefficients of the 2D developed shape are constant at any offset distance d close to 0.

Table 5.1 shows the CPU time spent on each optimization for various numbers of

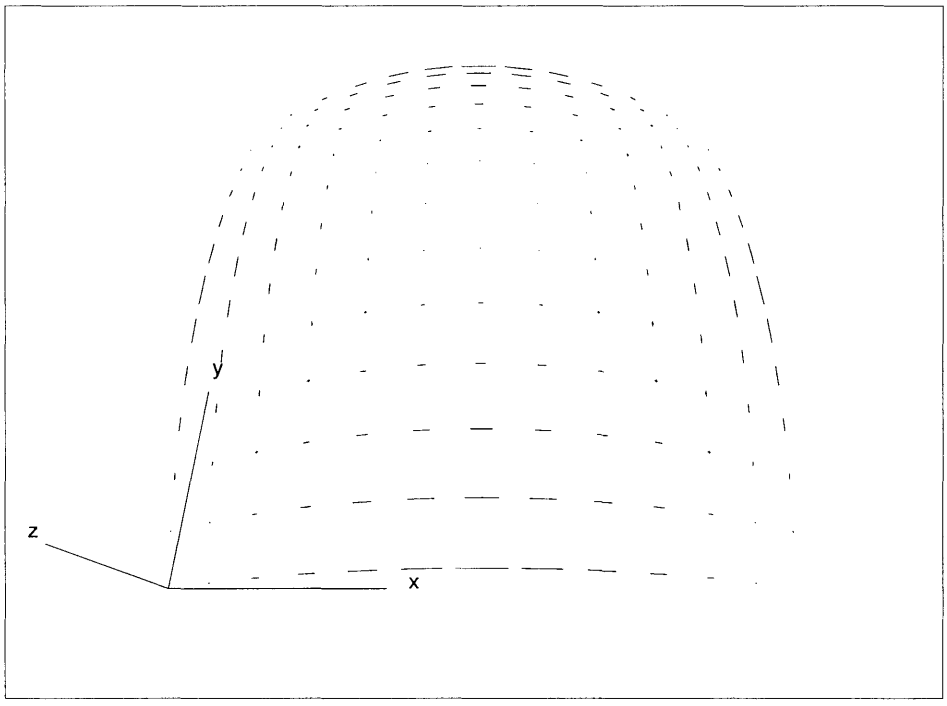

Figure 5-5: The strain distribution of the surface in Example 1, developed along isoparametric lines

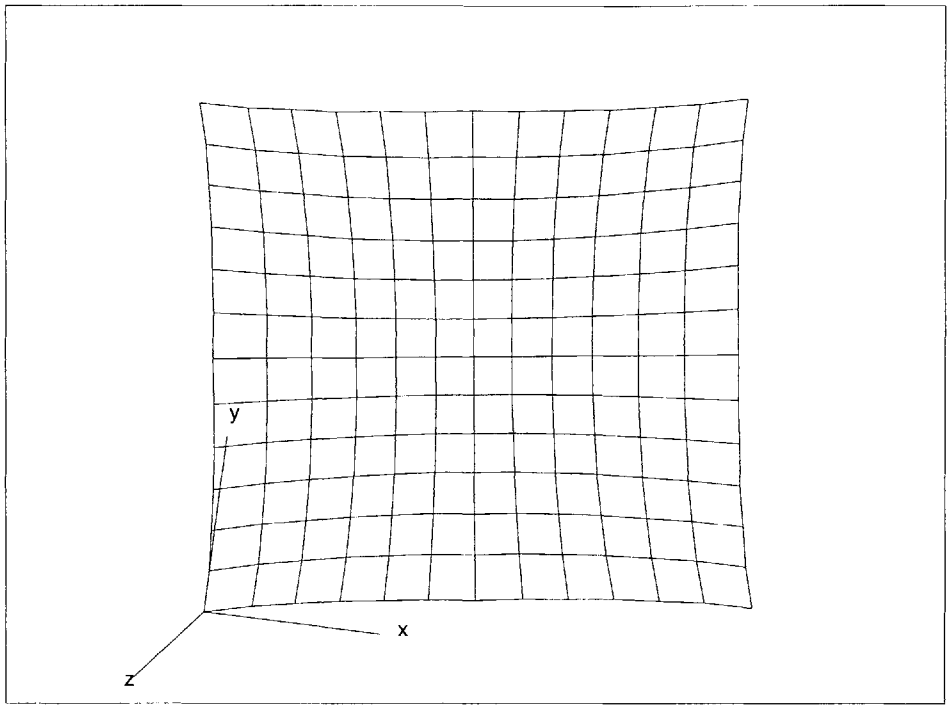

Figure 5-6: The corresponding 2D shape of the surface in Example 1, developed along isoparametric lines

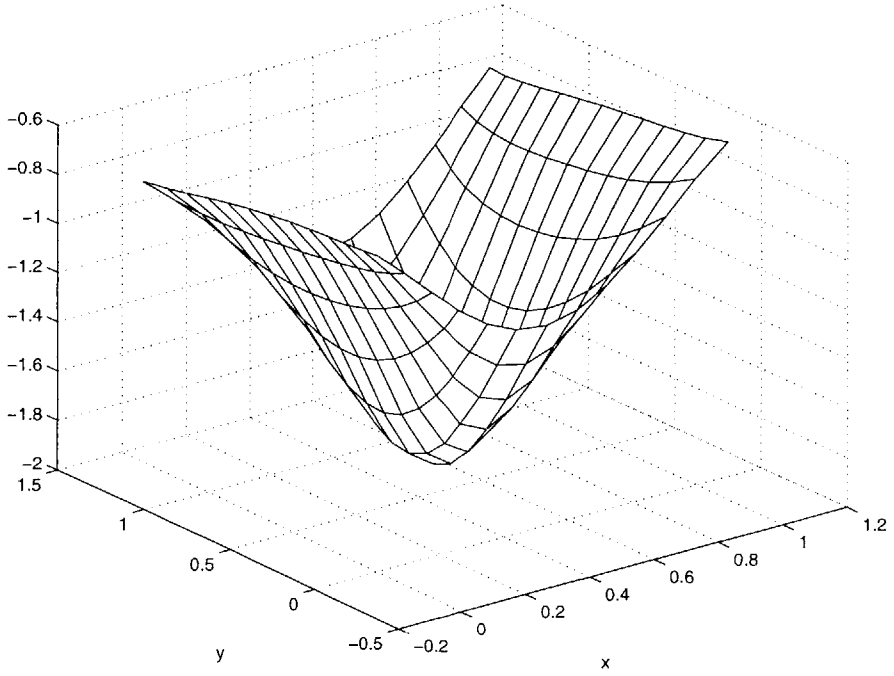

Figure 5-7: Logarithmic strain gradients along u-isoparametric line

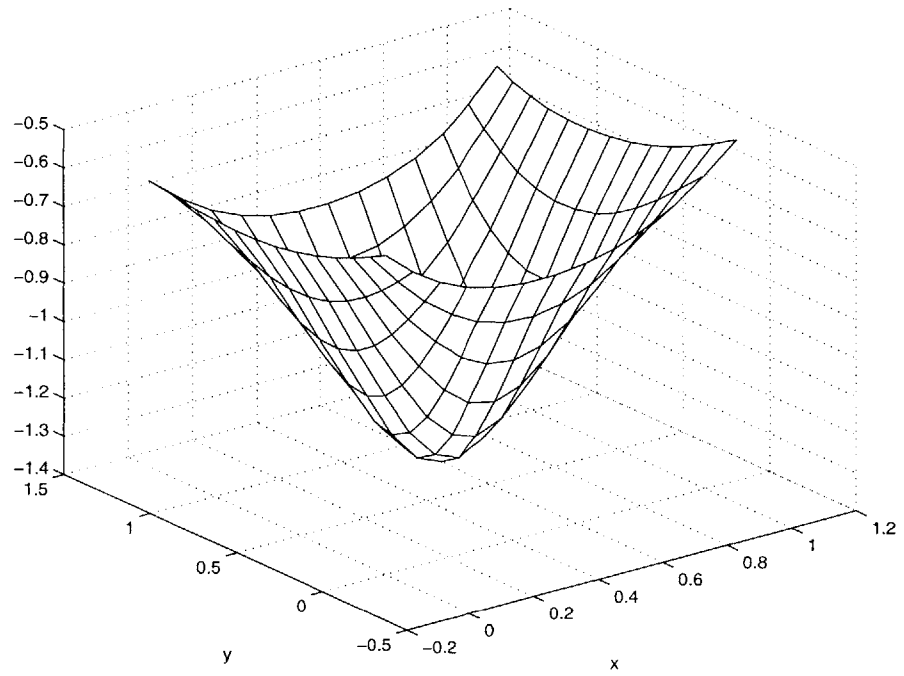

Figure 5-8: Logarithmic strain gradients along v-isoparametric line

grid points, objective functions, etc., where Ng is the number of grid points in both u and v directions; Niter1 is the number of iterations in the first optimization; obj1 is the converged value of the objective function in the first optimization; CPU1 is the CPU time spent on the first optimization; Niter2 is the number of iterations in the second optimization and CPU2 is the CPU time spent on the second optimization. For various numbers of grid points, the tolerance for constraints is 10^{-5}, and the tolerance for objective function is 10^{-4}.

Results from surface development along principal curvature directions

Figure 5-9 shows the strain distribution after the constrained minimization problem was solved using tolerances 10^{-5} for the constraints and 10^{-4} for the objective function. The strains are scaled to fit into the figure. The extreme values of the strain field are located at $(u, v) = (0, 0.5)$ or $(u, v) = (1.0, 0.5)$ with $(\varepsilon^s, \varepsilon^t) = (0.1808969, 0.006270948)$, and at $(u, v) = (0.5, 0)$ or $(u, v) = (0.5, 1.0)$ with $(\varepsilon^s, \varepsilon^t) = (0.001567142, 0.1790917)$. The objective function converges to 6.78804×10^{-3} at the solution, and all the constraints are within the tolerance of 1.0×10^{-5}.

Table 5.1: CPU time for each optimization at various number of grid points (Example 1, development along isoparametric lines)

Ng	Niter1	obj1 (10^{-3})	CPU1 (s)	Niter2	CPU2 (s)
7	2	6.658	0.71	11	5.86
9	8	6.492	8.53	6	12.67
11	7	6.428	34.72	5	37.00
13	18	6.386	177.49	5	110.66
15	13	6.359	401.26	6	333.23
17	15	6.341	1097.28	5	658.71
19	33	6.327	3869.18	5	1390.80
21	37	6.317	8168.48	5	2761.26

After development, the planar shape is shown in Figure 5-10. The four corner points have coordinates of (0,0), (-0.11802,1.09373), (1.17949,0.12786), (1.06147,1.22159) respectively. The final value of the formula (5.53) is less than 2×10^{-4} times $\sum_{i=1}^{N_g^u}\sum_{j=1}^{N_g^v}(e_{ij}^2+f_{ij}^2+g_{ij}^2)$, the sum of the squares of the right side of system (5.52) at all grid points.

Figure 5-11 and Figure 5-12 show the ideal strain gradient $\frac{\partial[\ln(1+\varepsilon^s)]}{\partial d}\Big|_{d=0}$ and $\frac{\partial[\ln(1+\varepsilon^t)]}{\partial d}\Big|_{d=0}$ evaluated at grid points such that the first fundamental form coefficients of the 2D developed shape are constant at any offset distance d close to 0.

Table 5.2 shows the CPU time spent on each optimization for various number of grid points, objective functions, etc.

Table 5.2: CPU time for each optimization at various numbers of grid points (Example 1, development along principal curvature directions)

Ng	Niter1	obj1 (10^{-3})	CPU1(s)	Niter2	CPU2(s)
7	6	6.389	1.45	11	5.66
9	6	6.610	6.52	6	11.84
11	9	6.703	32.16	6	41.75
13	13	6.788	124.99	5	106.97
15	16	6.826	413.91	5	298.96
17	15	6.842	942.79	5	682.85
19	18	6.846	2341.75	5	1419.11
21	28	6.850	5770.87	5	2761.5

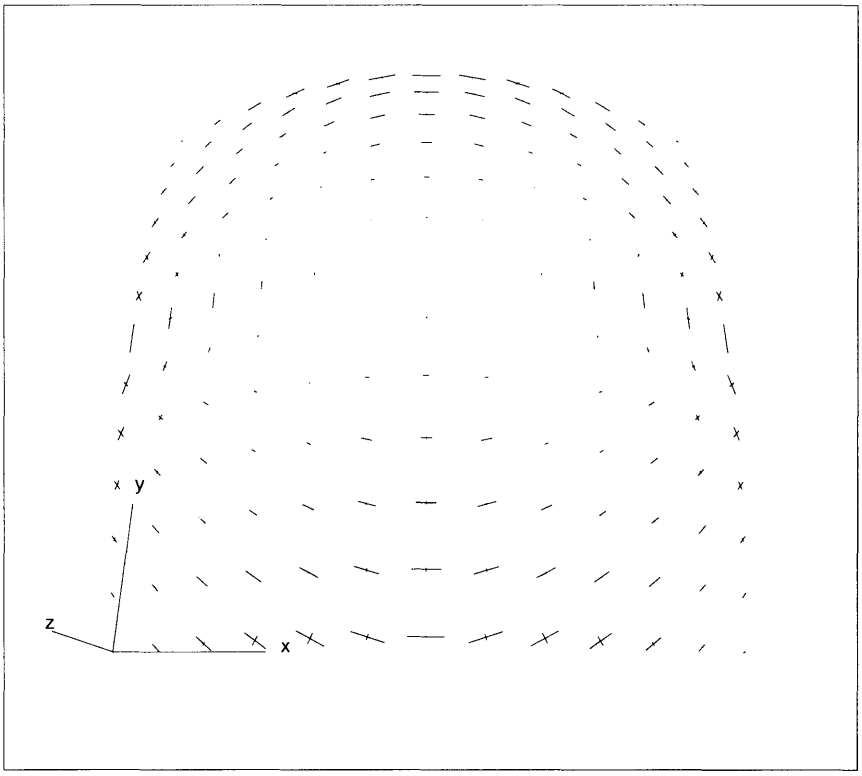

Figure 5-9: The strain distribution of the surface in Example 1, developed along the principal curvature directions

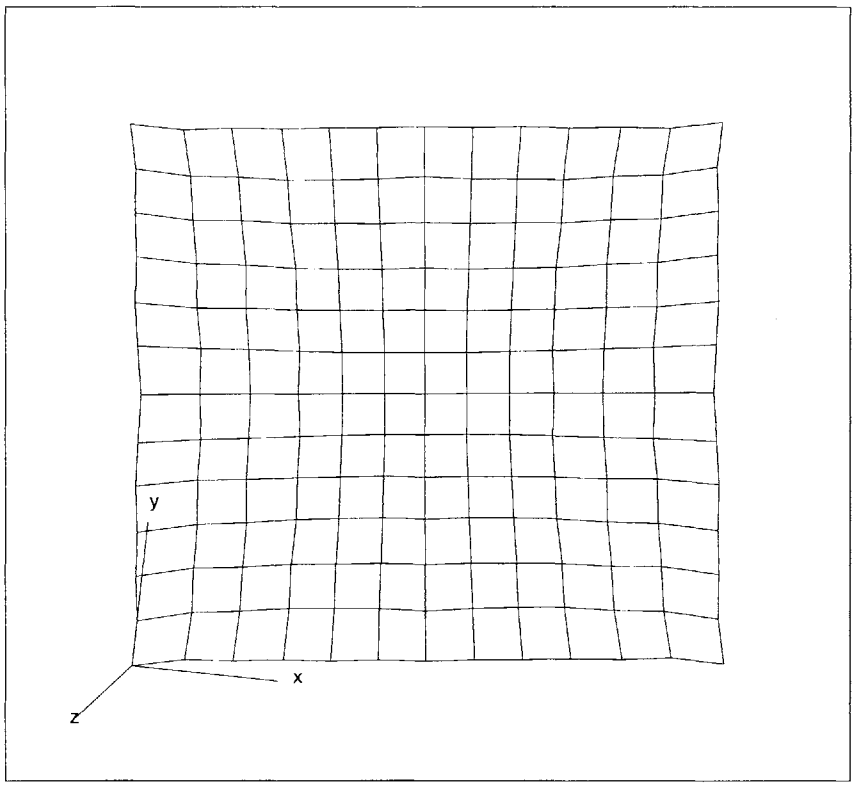

Figure 5-10: The corresponding 2D shape of the surface in Example 1, developed along the principal curvature directions

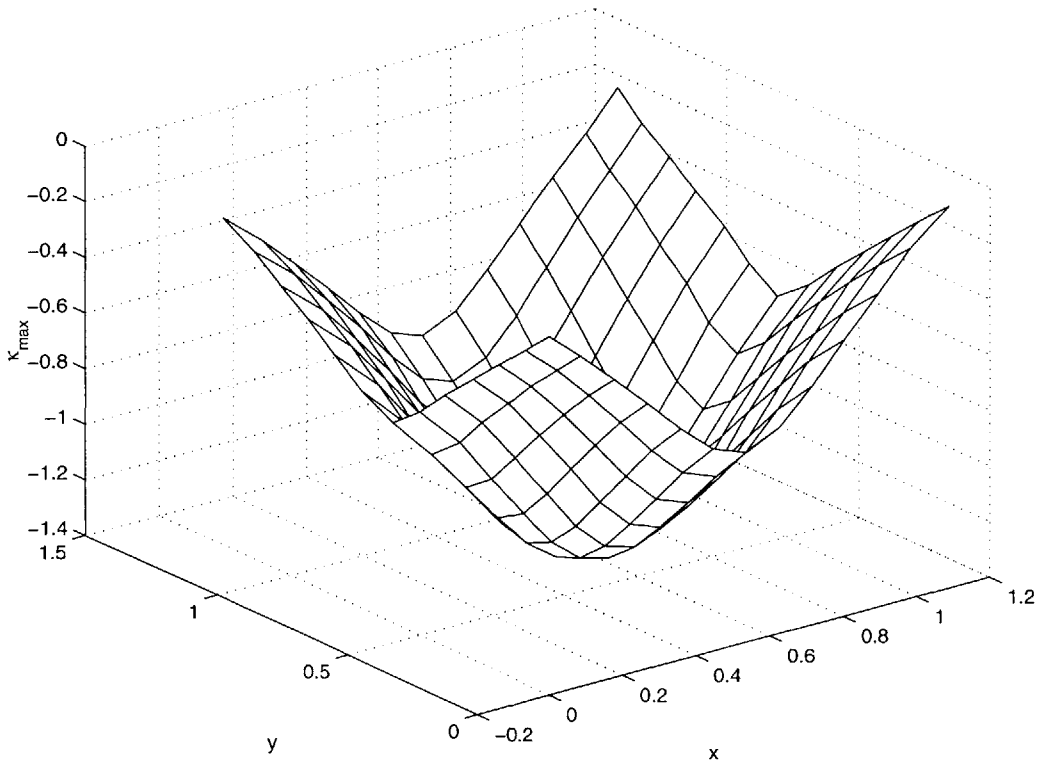

Figure 5-11: Logarithmic strain gradients along maximum curvature direction for the surface in Example 1, developed along the principal curvature directions

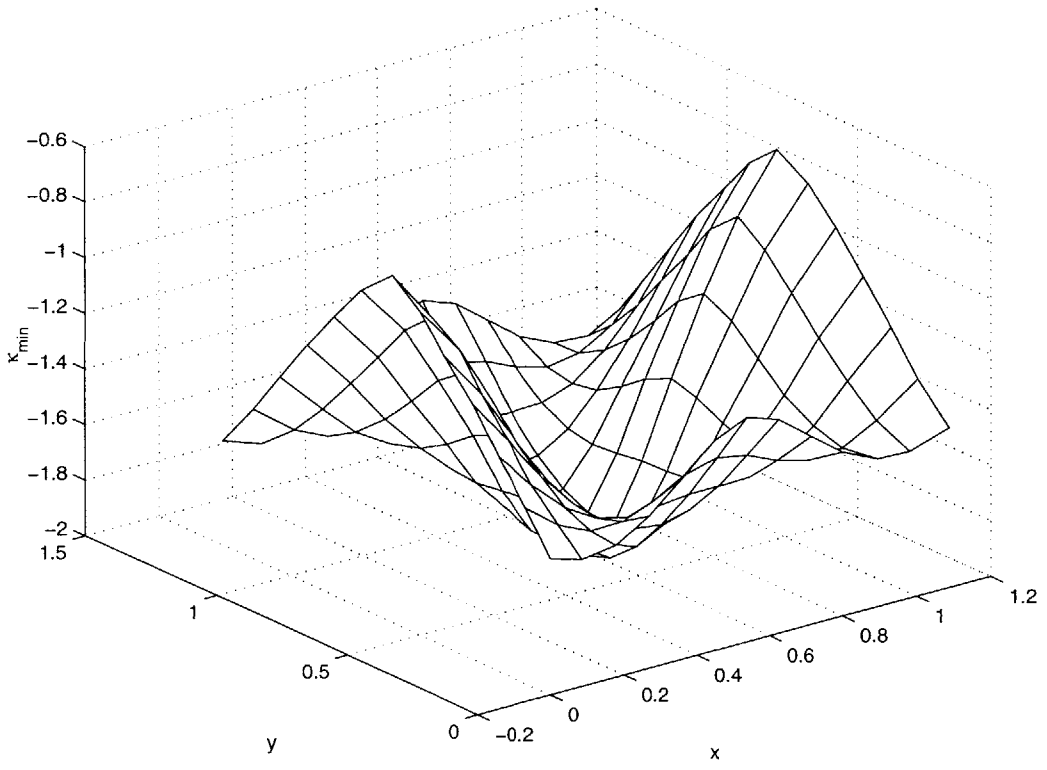

Figure 5-12: Logarithmic strain gradients along minimum curvature direction for the surface in Example 1, developed along the principal curvature directions

Example 2

We use this example to show how the algorithms work and the convergence of the objective function during the process.

The second surface is a bicubic Bézier surface $\mathbf{r}(u,v) = \sum_{i=0}^{3}\sum_{j=0}^{3}\mathbf{r}_{ij}B_{i,3}(u)B_{j,3}(v)$, where all the points on the surface are hyperbolic. The control points of the saddle-shaped surface are given by:

$(0,0,0.25)$	$(0,1/3,0.1)$	$(0,2/3,-0.1)$	$(0,1,-0.25)$
$(1/3,0,0.1)$	$(1/3,1/3,0.05)$	$(1/3,2/3,-0.05)$	$(1/3,1,-0.1)$
$(2/3,0,-0.1)$	$(2/3,1/3,-0.05)$	$(2/3,2/3,0.05)$	$(2/3,1,0.1)$
$(1,0,-0.25)$	$(1,1/3,-0.1)$	$(1,2/3,0.1)$	$(1,1,0.25)$

The surface is shown in Figure 5-13. Again, 13×13 grid points are used in discretization.

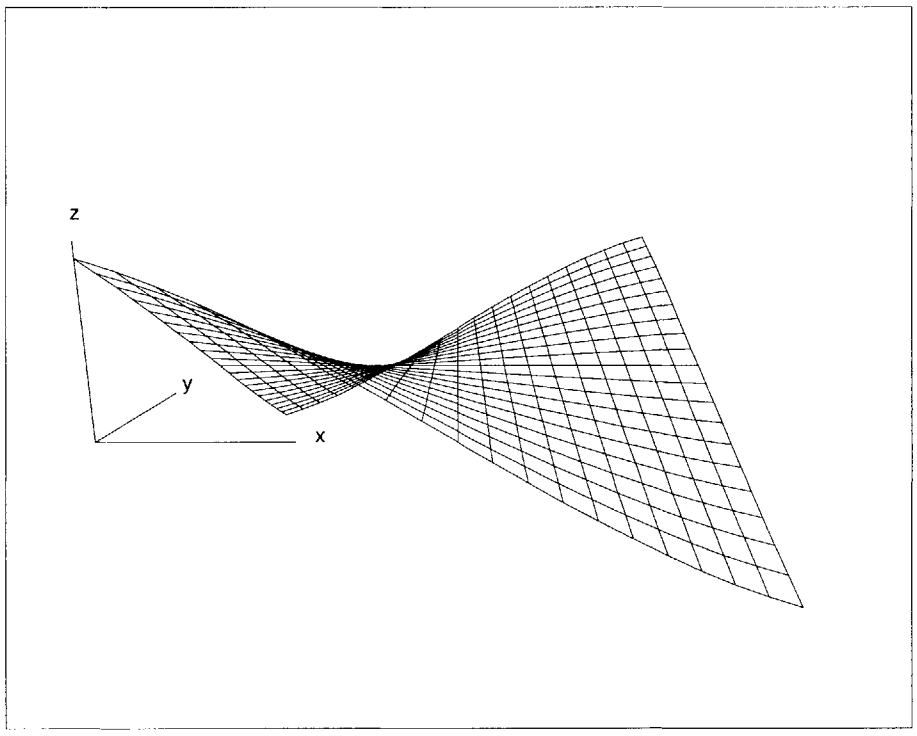

Figure 5-13: The bicubic Bézier surface in Example 2

Results from surface development along isoparametric lines

Figure 5-14 shows the strain distribution after the constrained minimization problem was solved using tolerances of 10^{-5} for the constraints and 10^{-4} for the objective function. The strains are scaled to fit into the figure. The extreme values of the strain field are located at $(u, v) = (0.5, 0.5)$ with $(\varepsilon^u, \varepsilon^v) = (0.0867214, 0.0886954)$. The objective function converges to the value of 4.005672×10^{-3} at the solution, and all the constraints are within the tolerance of 10^{-5}.

After development, the planar shape is shown in Figure 5-15. The four corner points have coordinates of (0,0), (-0.09223, 1.11186), (1.11534,0.09258), (1.02311, 1.20444), respectively. The final value of the formula (5.53) is less than 10^{-5} times $\sum_{i=1}^{N_g^u} \sum_{j=1}^{N_g^v} (e_{ij}^2 + f_{ij}^2 + g_{ij}^2)$, the sum of the squares of the right side of system (5.52) at all grid points. Here we see a planar development similar to that in Example 1.

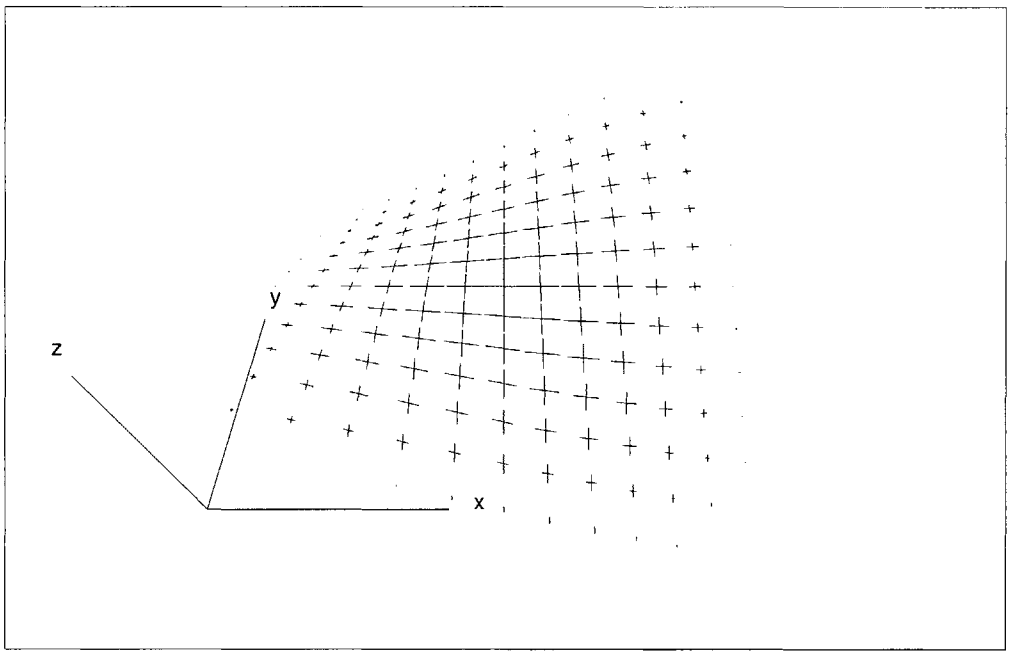

Figure 5-14: The strain distribution of the surface in Example 2, developed along isoparametric lines

Table 5.3 and Figure 5-16 show the variation of the objective function in the first

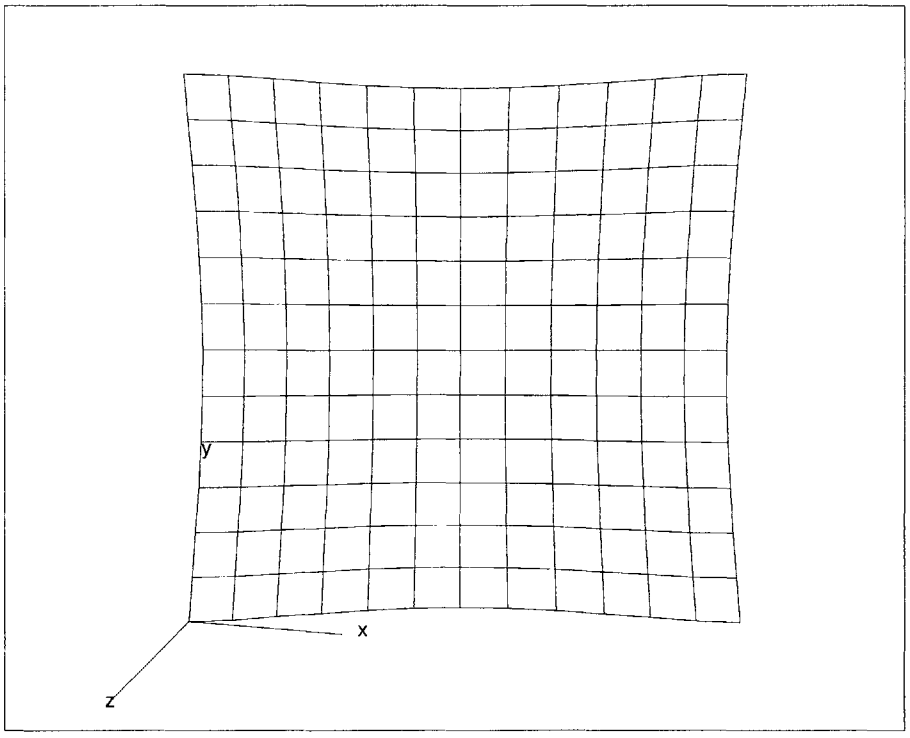

Figure 5-15: The corresponding 2D shape of the surface in Example 2, developed along isoparametric lines

optimization with respect to $\Delta u(=\Delta v)$ and number of grid points. A quadratic convergence is observed in the objective function of the first optimization. If we allow extrapolation, we can estimate the objective function approaches 0.003909 as $\Delta u = \Delta v \to 0$, see Figure 5-16. The curve in Figure 5-16 comes from fitting all the data points with the parabolic equation $y = a + bx^2$ with coefficients a, b determined by the least squares error method.

Table 5.3: The objective function of the 1st optimization (Example 2, development along isoparametric lines)

Grid number	7	9	11	13	15	17	19	21
$\Delta u = \Delta v$	1/6	1/8	1/10	1/12	1/14	1/16	1/18	1/20
obj1 ($\times 10^{-3}$)	4.2831	4.125	4.038	4.006	3.970	3.964	3.953	3.945

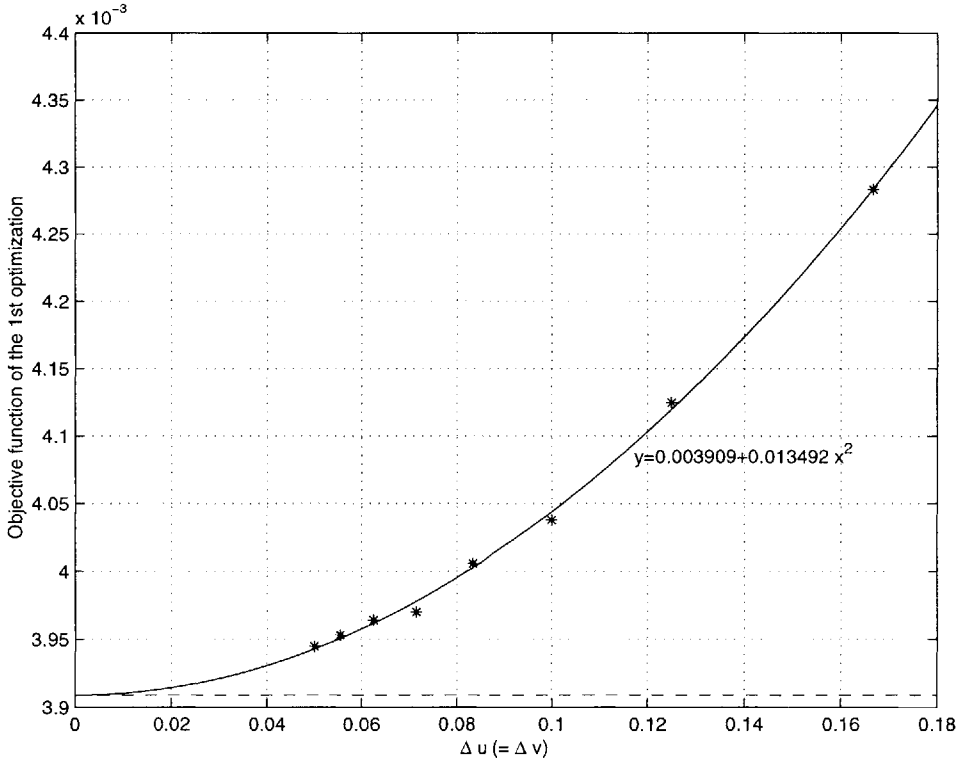

Figure 5-16: Variation of objective function in 1st optimization for the surface in Example 2, developed along isoparametric lines

Results from surface development along principal curvature directions

Figure 5-17 shows the strain distribution after the constrained minimization problem was solved using tolerances 10^{-5} for the constraints and 10^{-4} for the objective function. The strains are scaled to fit into the figure. As a comparison with the results in Section 5.5.1, the strains at $(u, v) = (0.5, 0.5)$ are $(\varepsilon^s, \varepsilon^t) = (0.05627, 0.05581)$. The objective function is 2.791×10^{-3} at the solution, and all the constraints are within the tolerance of 1.0×10^{-5}.

After development, the planar shape is shown in Figure 5-18. The four corner points have coordinates of (0,0), (-0.09909,1.11083), (1.11505,0.09953), (1.01596,1.21035) respectively. The final value of the formula (5.53) is less than 3×10^{-5} times $\sum_{i=1}^{N_g^u} \sum_{j=1}^{N_g^v} (e_{ij}^2 + f_{ij}^2 + g_{ij}^2)$, the sum of the squares of the right side of system (5.52) at all grid points.

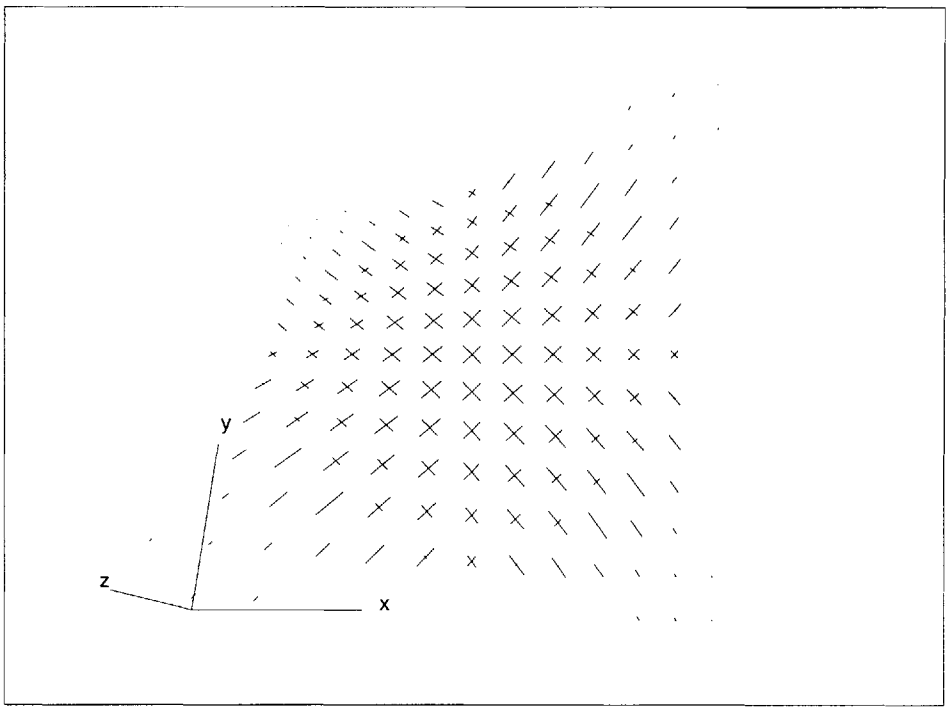

Figure 5-17: The strain distribution of the surface in Example 2, developed along the principal curvature directions

Table 5.4 and Figure 5-19 shows the variation of the objective function in the

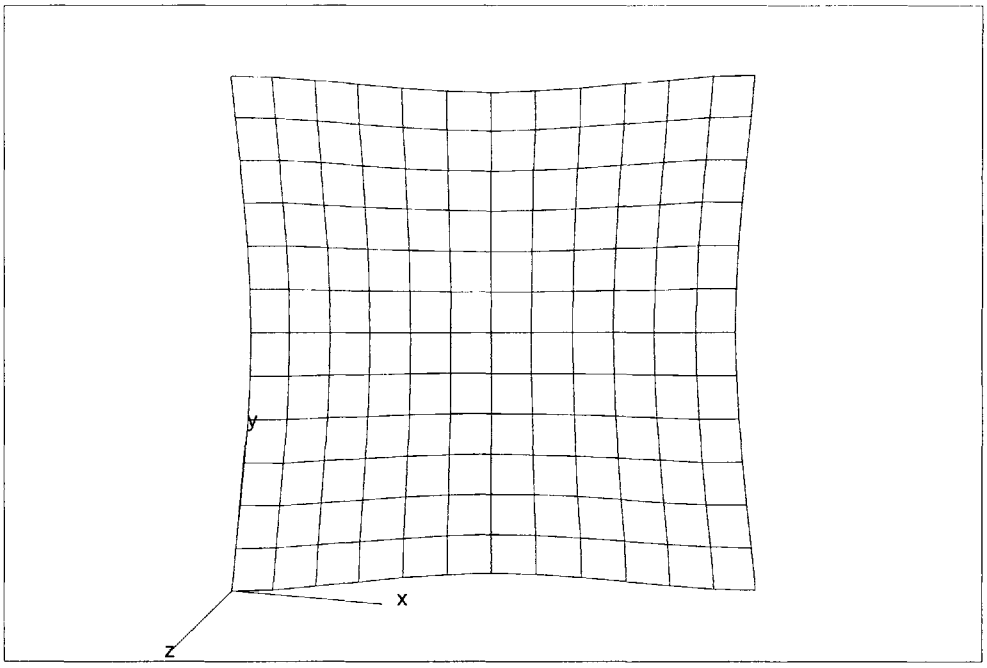

Figure 5-18: The corresponding 2D shape of the surface in Example 2, developed along the principal curvature directions

first optimization with respect to $\Delta u(=\Delta v)$ and number of grid points. As pointed in Section 5, a quadratic convergence is observed of the objective function of the first optimization. If we allow extrapolation, we can estimate the objective function approaches 0.002689 as $\Delta u = \Delta v \to 0$.

Table 5.4: The objective function of the 1st optimization (Example 2, development along principal curvature directions)

Grid number	7	9	11	13	15	17	19	21
$\Delta u = \Delta v$	1/6	1/8	1/10	1/12	1/14	1/16	1/18	1/20
obj1 ($\times 10^{-3}$)	3.1611	2.93382	2.8422	2.7909	2.7661	2.7486	2.7388	2.7331

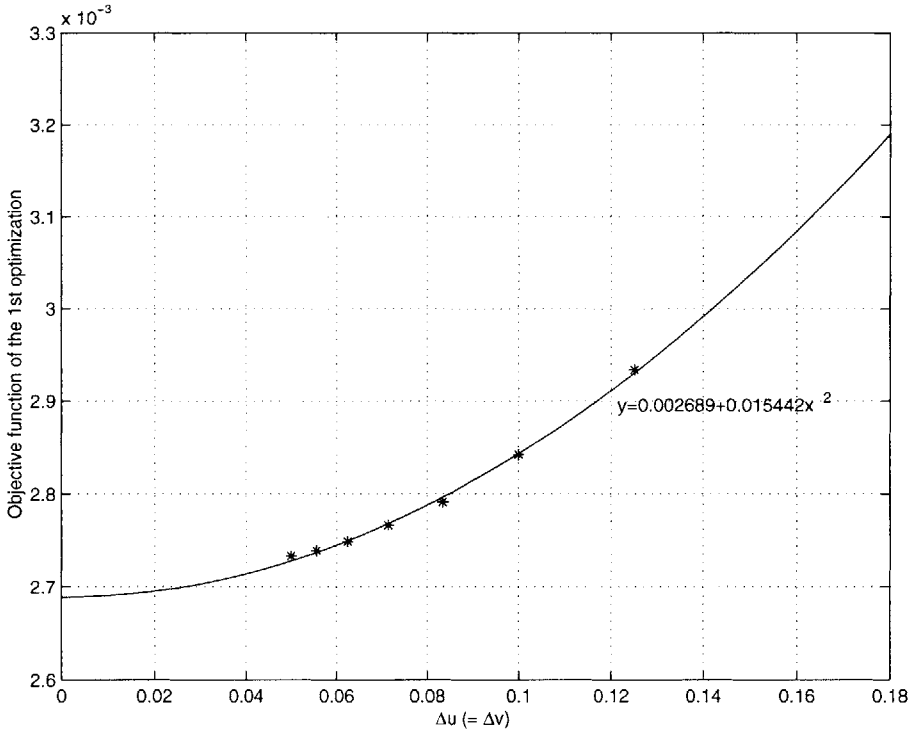

Figure 5-19: Variation of objective function in 1st optimization for the surface in Example 2, developed along the principal curvature directions

Example 3

This example shows the performance of the algorithms on a general B-spline surface. A wave-like bicubic integral B-spline surface

$$\mathbf{r}(u,v) = \sum_{i=0}^{4}\sum_{j=0}^{4} \mathbf{r}_{ij} N_{i,4}(u) N_{j,4}(v)$$

on a uniform knot vector with the following control points (x, y, z)

$(0,0,0)$	$(0,0.25,0)$	$(0,0.5,0)$	$(0,0.75,0)$	$(0,1,0)$
$(0.25,0,0)$	$(0.25,0.25,0.2)$	$(0.25,0.5,0)$	$(0.25,0.75,-0.2)$	$(0.25,1,0)$
$(0.5,0,0)$	$(0.5,0.25,0)$	$(0.5,0.5,0)$	$(0.5,0.75,0)$	$(0.5,1,0)$
$(0.75,0,0)$	$(0.75,0.25,-0.2)$	$(0.75,0.5,0)$	$(0.75,0.75,0.2)$	$(0.75,1,0)$
$(1,0,0)$	$(1,0.25,0)$	$(1,0.5,0)$	$(1,0.75,0)$	$(1,1,0)$

is shown in Figure 5-20. 17×17 grid points are used in discretization.

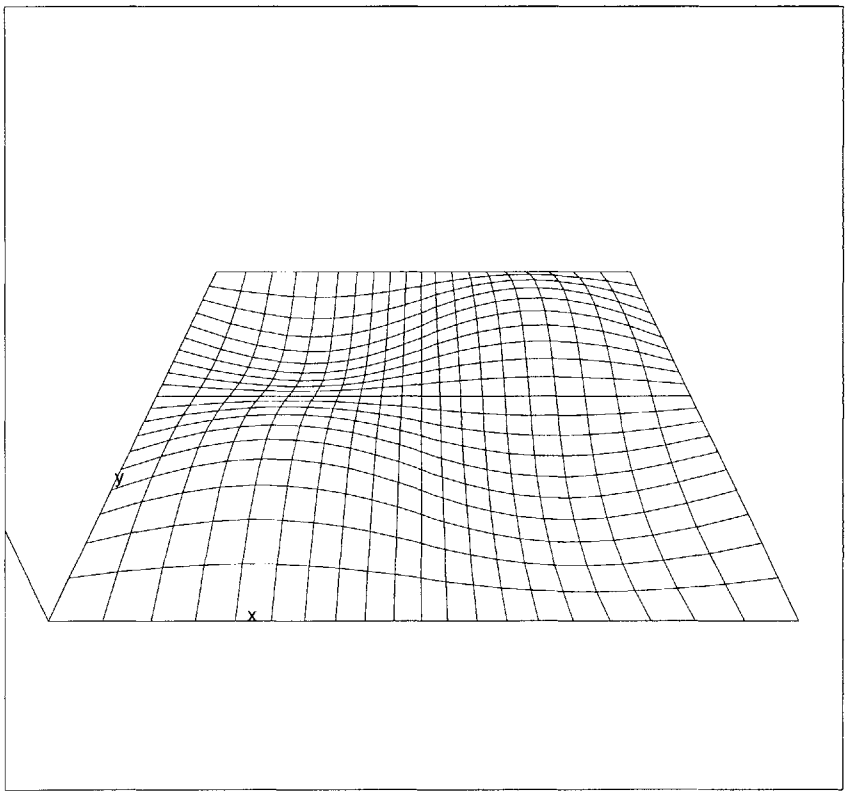

Figure 5-20: A wave-like B-spline surface in example 3

Results from surface development along isoparametric lines

Figure 5-21 shows the strain distribution after the constrained minimization problem was solved using tolerances of 10^{-7} for the constraints and 10^{-4} for the objective function. The strains are scaled to fit into the figure. The strains at the center of the surface $(u, v) = (0.5, 0.5)$ are $(\varepsilon^u, \varepsilon^v) = (0.0555, 0.0550)$. The objective function converges to the value of 9.84842×10^{-4} at the solution, and all the constraints are within the tolerance of 10^{-7}.

After development, the planar shape is shown in Figure 5-22. The four corner points have coordinates of (0, 0), (0.00315, 1.03617), (1.03618, −0.00312), (1.03933, 1.03306), respectively. The final value of the formula (5.53) is about 10^{-4} times $\sum_{i=1}^{N_g^u} \sum_{j=1}^{N_g^v} (e_{ij}^2 + f_{ij}^2 + g_{ij}^2)$, the sum of the squares of the right side of system (5.52) at all grid points.

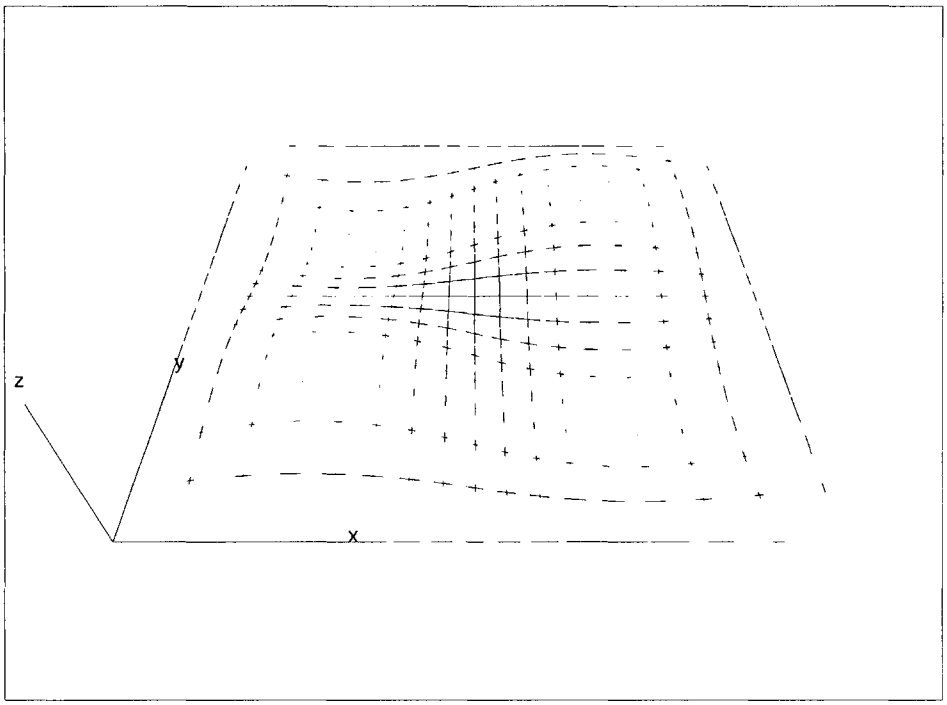

Figure 5-21: The strain distribution of the surface in Example 3, developed along isoparametric lines

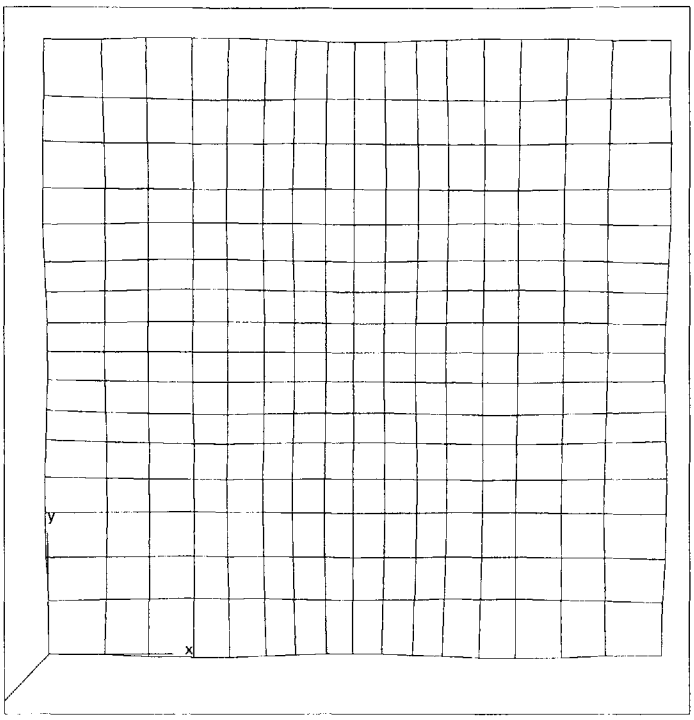

Figure 5-22: The corresponding 2D shape of the surface in Example 3, developed along isoparametric lines

Results from surface development along principal curvature directions

Figure 5-23 shows the strain distribution after the constrained minimization problem was solved using the tolerance of 10^{-8} for the constraints and 10^{-4} for the objective function. The strains are scaled to fit into the figure. As a comparison with the results in Section 5.5.1, the strains at $(u, v) = (0.5, 0.5)$ are $(\varepsilon^s, \varepsilon^t) = (0.08258, 0.08267)$. The objective function is 1.6018×10^{-3} at the solution, and all the constraints are within the tolerance of 1.0×10^{-8}.

After development, the planar shape is shown in Figure 5-24. The four corner points have coordinates of (0, 0), (0.01073, 1.03467), (1.03467, −0.01074), (1.04540, 1.02393), respectively. The final value of the formula (5.53) is about 1.4×10^{-4} times $\sum_{i=1}^{N_g^u} \sum_{j=1}^{N_g^v} (e_{ij}^2 + f_{ij}^2 + g_{ij}^2)$, the sum of the squares of the right side of system (5.52) at all grid points.

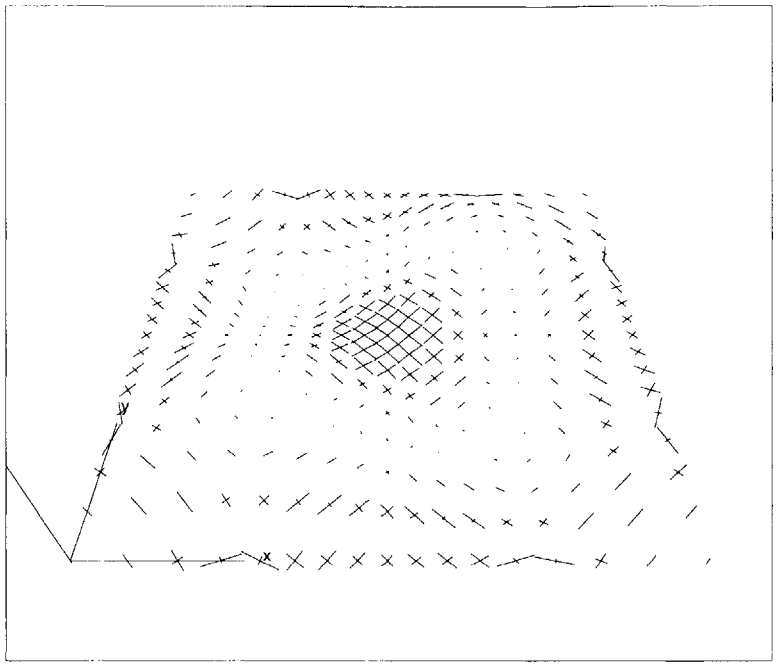

Figure 5-23: The strain distribution of the surface in Example 3, developed along the principal curvature directions

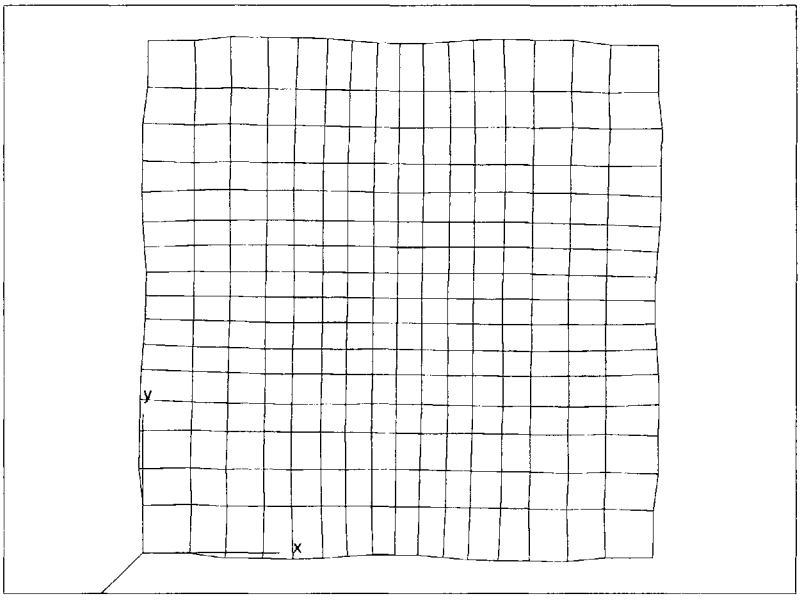

Figure 5-24: The corresponding 2D shape of the surface in Example 3, developed along the principal curvature directions

Example 4

The surface to be developed in this example is a sphere cap as shown in Figure 5-25. The radius of the sphere is 1, and the height of the sphere cap is $1 - \frac{\sqrt{2}}{2}$. The sphere cap is expressed as a B-spline surface, with isoparametric lines $v = const$ the meridians, and isoparametric lines $u = const$ the parallels. For this surface, all points are umbilic points, so it is developed along the isoparametric lines. Since for this example, the surface has a periodic parametrization along v direction, the formulation of the discrete version of the optimization problem is slightly modified to allow $v = 1$ isoparametric line to be the same as $v = 0$ isoparametric line. A set of 17×17 grid points are used in discretization. Figure 5-26 shows the strain distribution after the constrained minimization problem is solved using tolerances of 10^{-5} for both the constraints and the objective function. The strains are scaled to fit into the figure. The strains at the edge of the sphere cap are $(\varepsilon^u, \varepsilon^v) = (0.0, 0.05708)$. The objective function converges to the value of 1.832972×10^{-3} at the solution. After development, the planar shape is shown in Figure 5-27. The coordinate of the rightmost grid point is $(0.0767, 0)$. It is easy to see that we will obtain a circular planar shape when we increase the number of grid points, i.e., a spherical shape will be developed into a circular shape.

5.5.2 Results from isometric development

In this section, surfaces are developed using the method proposed by Manning [30]. When the spine curve is a geodesic, this method is similar to the geodesic development in shipyards [37]. In geodesic development widely used in shipyards, both the spine curve and the branches are chosen to be geodesics. For the applications in line heating design, we have made further improvement so that by the surface development process, we can also determine the shrinkages necessary to fabricate the 2D shape into the 3D design surface.

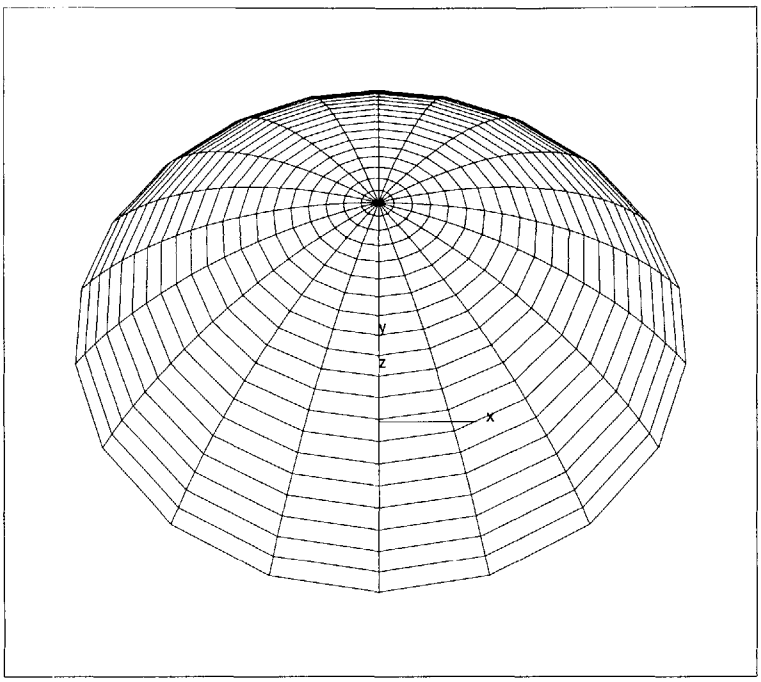

Figure 5-25: A sphere cap in example 4

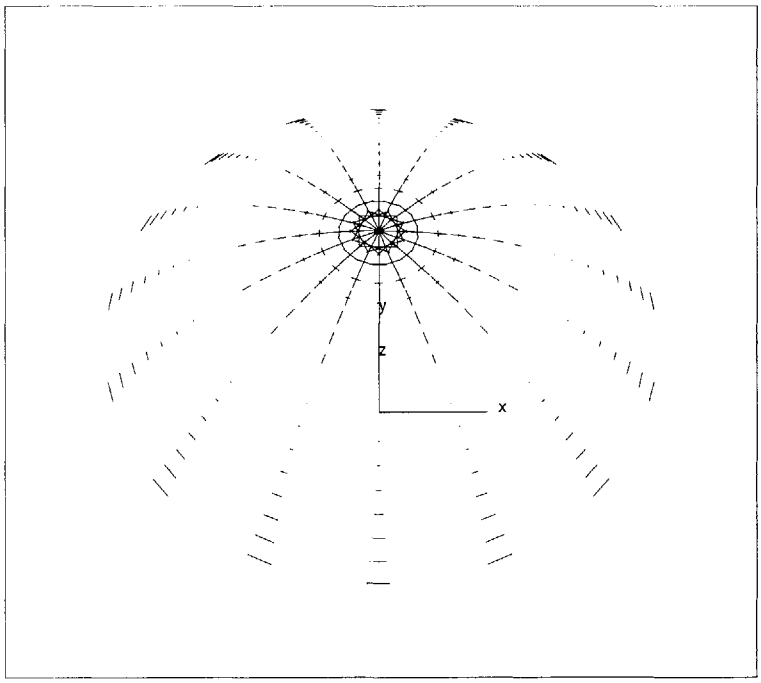

Figure 5-26: The strain distribution of the sphere cap after development

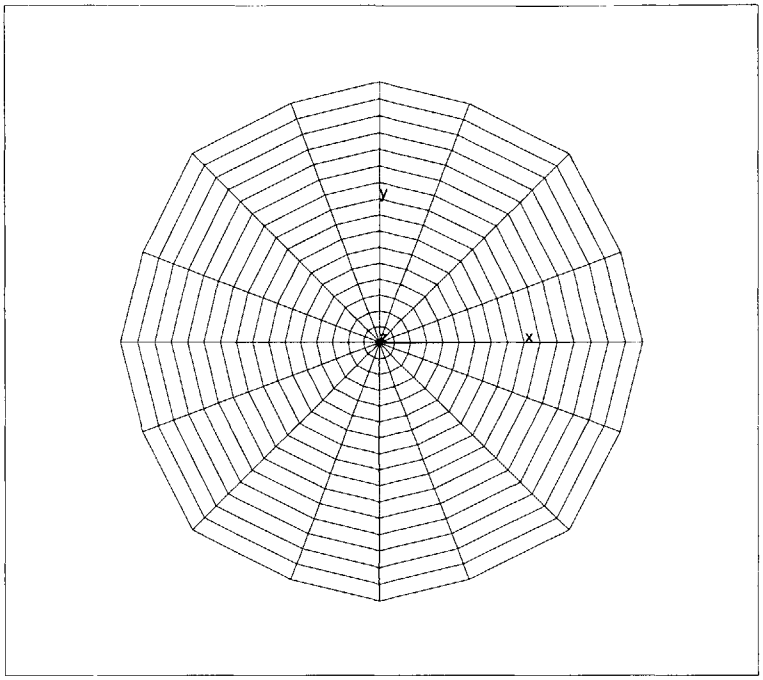

Figure 5-27: The corresponding planar shape of the sphere cap

Example 1

We develop the Bézier surface where all the points are elliptic, as shown in example 1 of Section 5.5.1. The isoparametric curve $v = 0.5$, which is also a geodesic, is chosen to be the spine curve for surface development. The 11 branches selected are the isoparametric curves $u = \frac{i}{10}$, $i = 0, 1, ..., 10$. The spine curve and the 11 branches are expanded isometrically into a 2D plane.

Figure 5-28 shows the developed 2D shape, along with the grid points for isometric development. After development, the geodesic curve is expanded into a straight line of length 1.14119. The four corner points of the 2D shape have coordinates of $(-0.07693, -0.50891)$, $(1.21812, -0.50891)$, $(1.21812, 0.50891)$, $(-0.07693, 0.50891)$ respectively. The numerical integration of each branch curve is carried on in 40 steps. After the development, the arc lengths between neighboring grid points on the 3D design surface are deducted from that on the 2D shape, which results in the shrinkages needed to fabricate the 2D shape into the 3D design surface. The shrinkages are shown in Figure 5-29.

It can be seen that isometric development of a surface produces a 2D shape usually

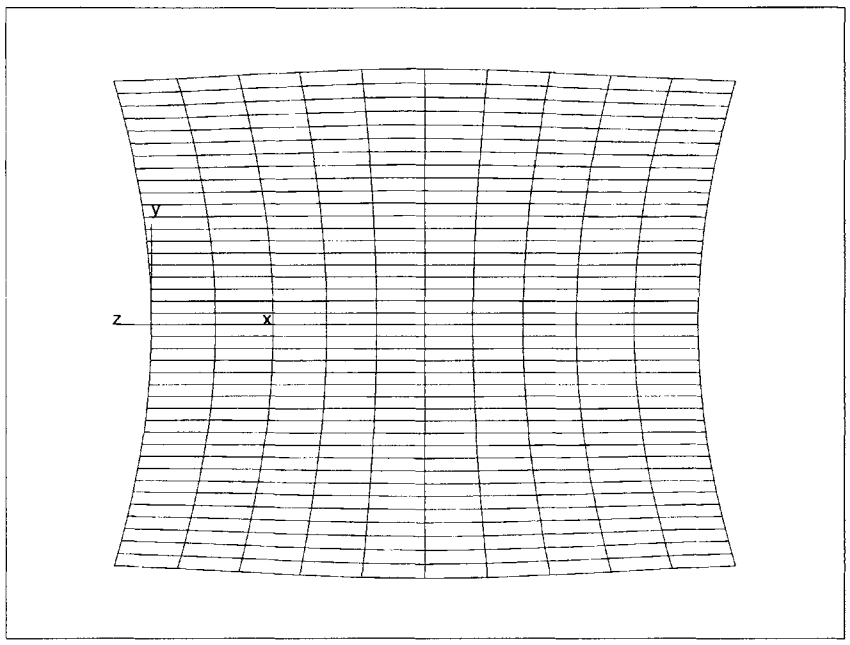

Figure 5-28: The 2D shape of the surface in Example 1 after isometric development

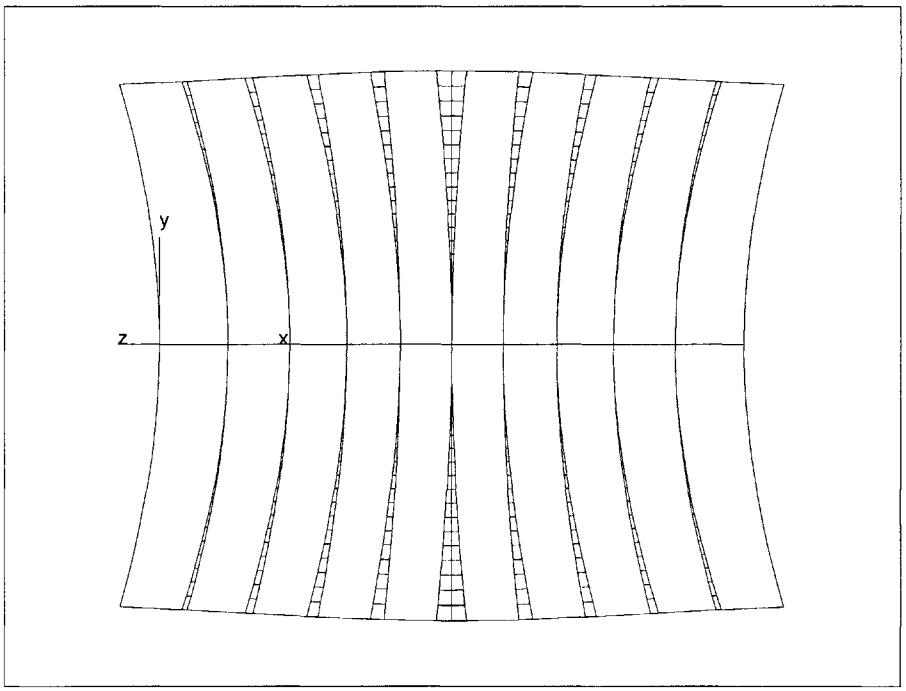

Figure 5-29: The shrinkages needed to fabricate the 2D shape into the 3D surface

larger than that from optimal development presented in earlier sections. Also, this 2D shape and the corresponding shrinkages are highly dependent on the spine curve selected. For some surface, it may be very hard to find a spine curve so that the deformation from 2D shape to 3D surface is only shrinkage, i.e., at some locations, expansion may be necessary, which is not realizable by line heating. We illustrate this problem in the following example.

Example 2

We develop the Bézier surface where all the points are hyperbolic, as shown in example 2 of Section 5.5.1. The isoparametric curve $v = 0.5$, which is also a geodesic, is chosen to be the spine curve for surface development. The 11 branches selected are the isoparametric curves $u = \frac{i}{10}$, $i = 0, 1, ..., 10$. The spine curve and the 11 branches are expanded isometrically into a 2D plane.

Figure 5-28 shows the developed 2D shape, along with the grid points for isometric development. After development, the spine curve is expanded into a straight line of length 1.0000. The four corner points of the 2D shape have coordinates of (0.00158, -0.55910), (0.99842, -0.55910),(0.99842, 0.55910), (0.00158, 0.55910), respectively. The numerical integration of each branch curve is carried on in 40 steps. After the development, the arc lengths between neighboring grid points on the 3D design surface are computed and drawn on the 2D shape. Connecting consecutively the end points results in the expansions needed to fabricate the 2D shape into the 3D design surface. The expansions are shown in the curved triangular areas in Figure 5-31. Since line heating can only produce shrinkage and bending, this 2D shape can not be fabricated into the 3D design surface by line heating. Therefore, isometric or geodesic development alone is not enough for determination of the initial shape for line heating. For this surface, it is very difficult to select a spine curve and branches that result in a development which is suitable for line heating.

Comparing the results from isometric development and those from optimal development in the previous section, we can draw the conclusion that isometric development can not take into account the characteristics of line heating, i.e., it may produce

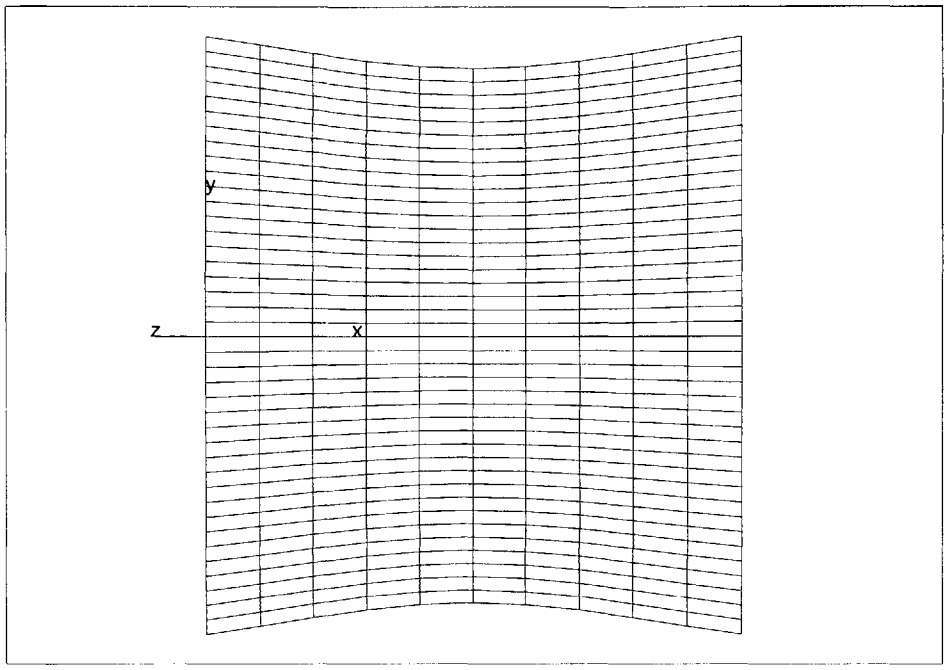

Figure 5-30: The 2D shape of the surface in Example 2 after isometric development

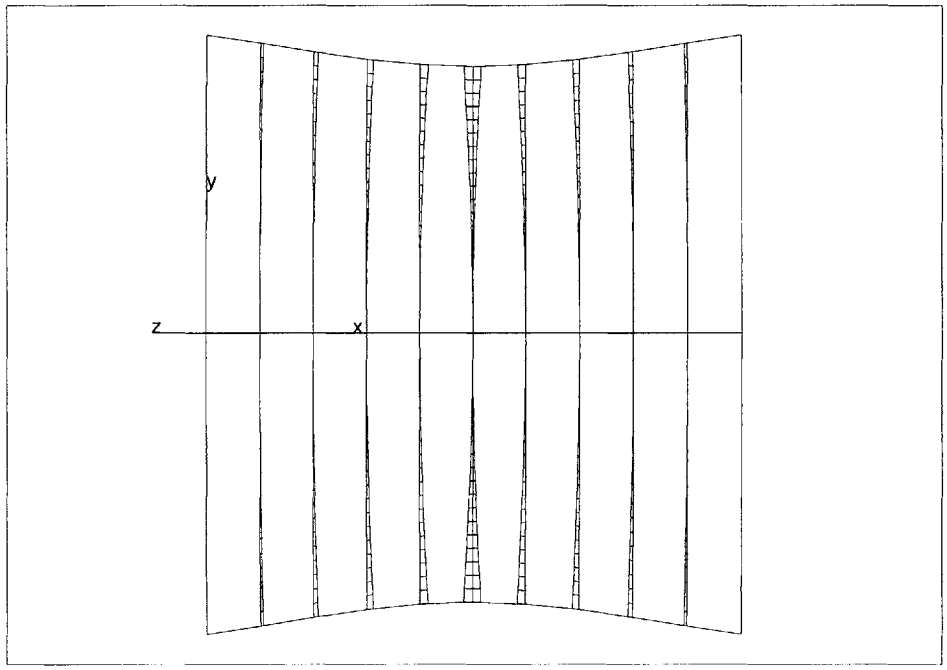

Figure 5-31: The expansions needed to fabricate the 2D shape into the 3D surface

a 2D shape which can not be formed into the design surface by line heating. Even though for some design surfaces the method may work well, the resulting 2D shape is usually larger, which results in more material used.

5.5.3 Results from FEM

In this section, we develop surfaces in the previous sections by using the finite element method. Finite element method (FEM) is used by Ueda et al [58] and Ishiyama et al. [19] for determination of initial 2D shape and planning of heating paths. A surface is modeled as the mid-surface of a curved plate. The top and bottom surfaces are the offset surfaces. The material is assumed to be elastic. A large deformation nonlinear FEM analysis is carried out to compute the deformed shape and strains when all the grid points on the sutfaces are forced to move to the $z = 0$ plane. The commercial software ABAQUS is used for finite element analysis.

Example 1

The first example is the same Bézier surface where all the points are elliptic, as shown in Section 5.5.1. The surface along with the two offset surfaces with an offset distance of 0.01 forms the mid, top and bottom surfaces of a curved plate. This curved plate is discretized by $12 \times 12 \times 2$ 8-node hexahedron elements, which corresponds to 13×13 grid points on the mid-surface. All the points on the mid-surface are forced to move to the x-y plane. To avoid rigid body motion, the point corresponding to $(u, v) = (0, 0)$ is fixed, and the point corresponding to $(u, v) = (1, 0)$ is forced to only move along the x axis. The FEM model is shown in Figure 5-32 and the 2D shape of the mid surface after development is shown in Figure 5-33. It can be seen that the 2D shape in Figure 5-33 is quite similar to that shown in Figure 5-6 obtained in Section 5.5.1. A comparison of the 2D shape obtained from optimal development and that from FEM is carried out in the next example.

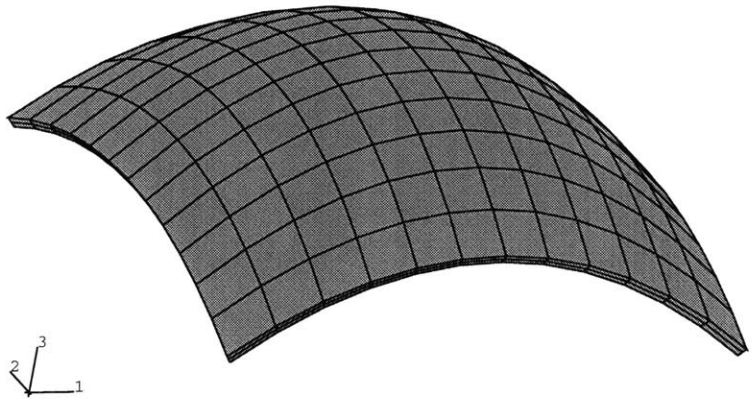

Figure 5-32: The FEM model for the surface in Example 1

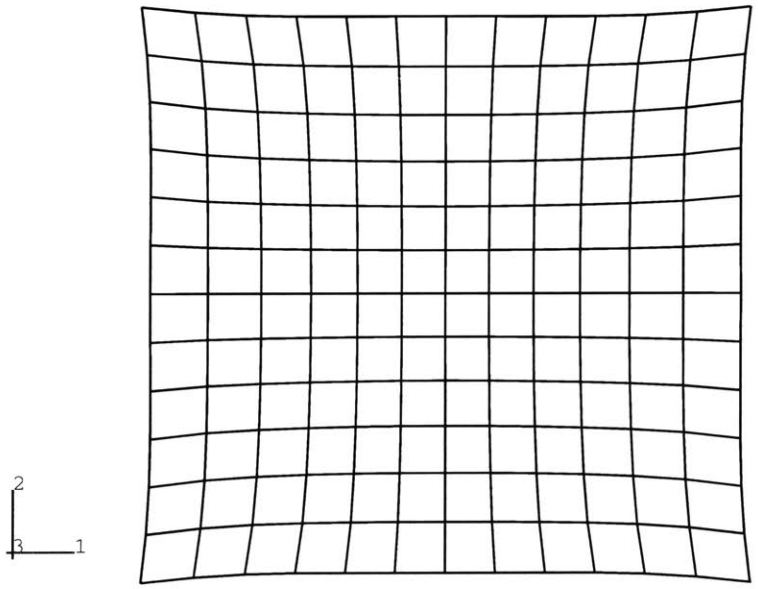

Figure 5-33: The 2D shape of the mid-surface after development

Example 2

The second example is the same Bézier surface where all the points are hyperbolic, as shown in Section 5.5.1. The surface along with the two offset surfaces with an offset distance of 0.01 forms the mid, top and bottom surfaces of a curved plate. This curved plate is discretized by $12 \times 12 \times 2$ 8-node hexahedron elements, which corresponds to 13×13 grid points on the mid-surface. All the points on the mid-surface are forced to move to the x-y plane. To avoid rigid body motion, the point corresponding to $(u, v) = (0, 0)$ is forced to move to the origin of the coordinate system, and the point corresponding to $(u, v) = (1, 0)$ is forced to only move along the x axis by keeping the y coordinate to be 0. The FEM model is shown in Figure 5-34 and the 2D shape of the mid surface after development is shown in Figure 5-35. In Figure 5-36, we put together the 2D shape from optimal development based on the strains along principal directions and that from FEM. It can be seen that the 2D shape is quite similar to that obtained in Section 5.5.1.

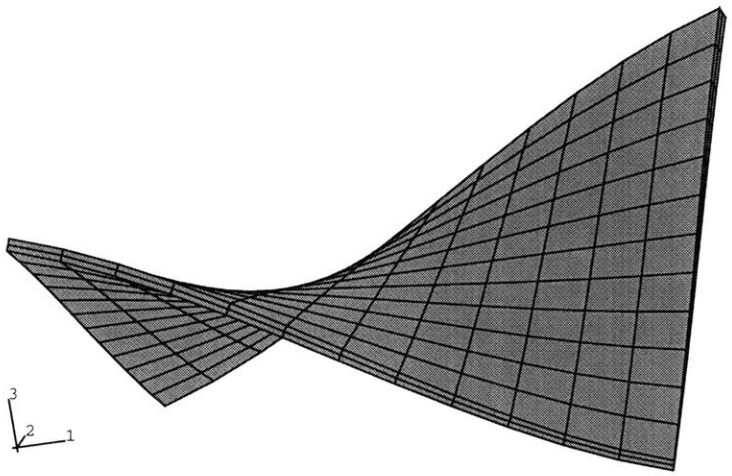

Figure 5-34: The FEM model for the surface in Example 2

However, the 2D shape from FEM is smaller compared with that from optimal development. The reason is that in FEM development, we cannot force all the strains to be positive, so usually compressive strains and tensile strains coexist in the developed

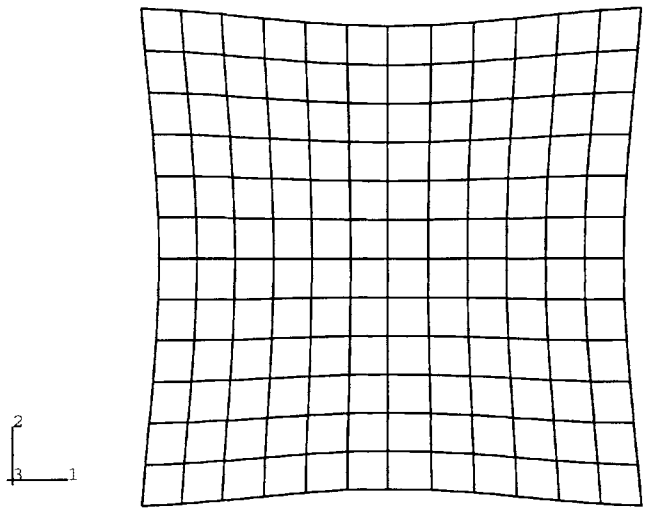

Figure 5-35: The 2D shape of the mid-surface after development in Example 2

shape. For illustration of this phenomenon, the principal strains for the nodes at the mid-surface are shown in Figure 5-37. For an approximation, the principal strains are computed based on planar strains τ_{xx}, τ_{xy} and τ_{yy} since these strain components are dominant on most of the nodes.

5.5.4 Discussion

From the comparisons of the results from optimal development with those from isometric development and from FEM, we see

1. The algorithms for optimal development guarantee a solution with only tensile strain from 3D design surface to 2D shape, or only compressive strain from 2D shape to 3D surface. Since the process of line heating can only generate shrinkage (or compressive strain) inside the heated plate, this solution captures the physical characteristics of the forming process by line heating and is the desired solution.

2. The result of isometric (or geodesic) development of doubly curved surface

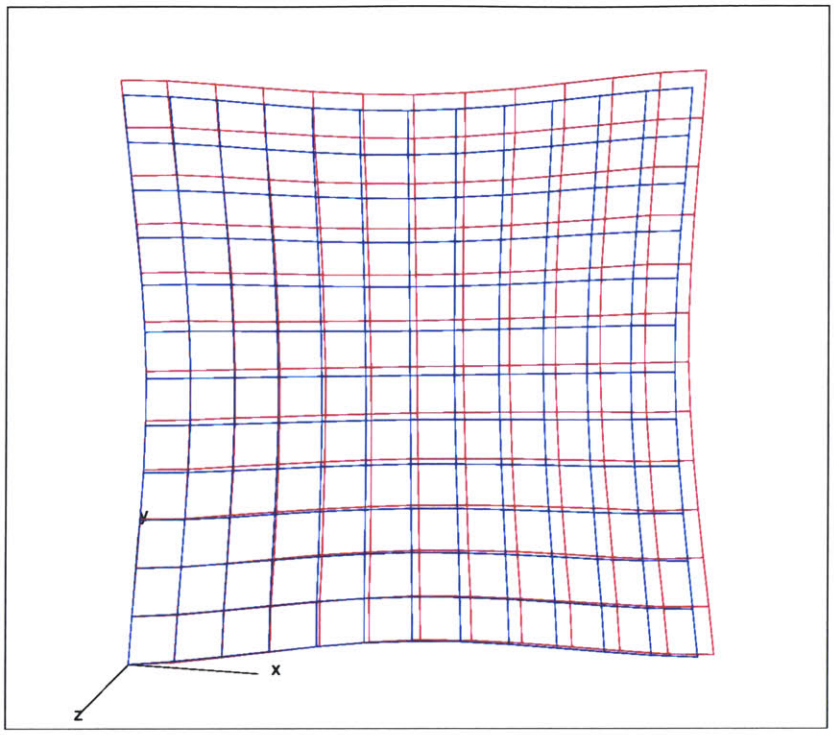

Figure 5-36: Comparison of the 2D shapes from optimal development (red line) and from FEM (blue line)

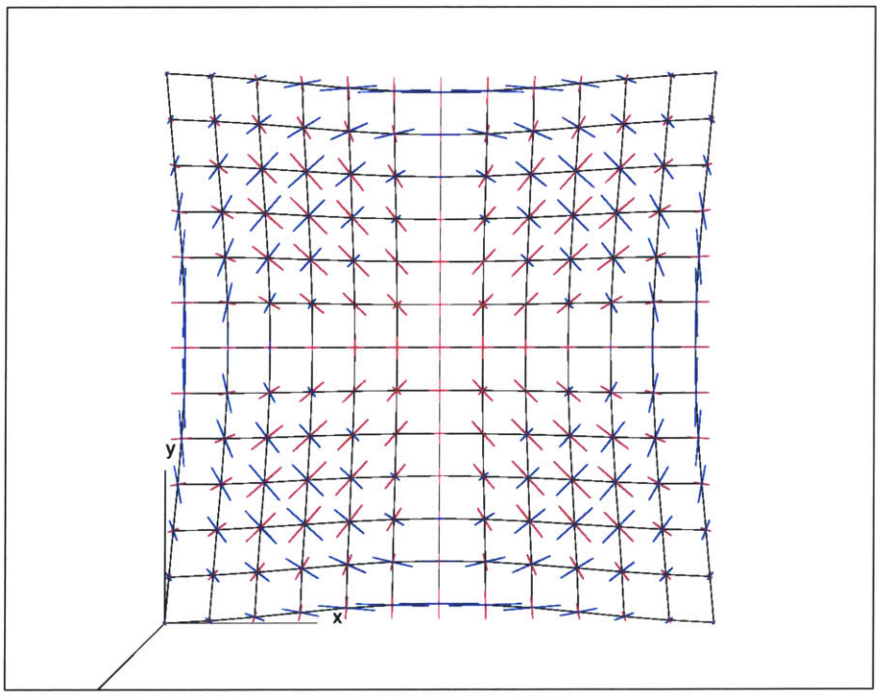

Figure 5-37: The principal strains at nodes on the mid-surface (red line for tensile strain, blue line for compressive strain, and black line for the developed shape

highly depends on the selection of spine curve. The method after our modification can produce the 2D shape, as well as the shrinkage or expansion necessary to make the 2D shape into the 3D design surface. However, we can not guarantee that the 2D shape can be made into the 3D surface by the line heating approach. If the isometric solution happens to be realizable, i.e. only shrinkage is necessary then the 2D shape is usually larger than that from optimal development and that from FEM.

3. The resulting 2D shape from FEM is usually smaller than that from optimal development since usually both tensile and compressive strains coexist from 3D surface to its 2D shape. Because no constraint of the strains can be imposed in finite element analysis, the FEM solution can not capture the physical characteristics of the forming process by line heating either.

Chapter 6

Conclusions and recommendations

6.1 Conclusions and contributions

This thesis models the process of shell forming by line heating. The major contributions of this thesis are:

1. Development of a finite element model for nonlinear thermo-mechanical analysis of the process of metal plate forming by line heating. A rezoning technique has been employed to greatly reduce the simulation time yet preserve the required accuracy. With this model we are able to investigate edge effects, effects of repeated heating, and effects of parallel heating.

2. Development of a semi-analytical thermal model for prediction of the temperature field during metal forming by line heating. This model takes into account the heat loss due to convection and the distributed heat source. A novel polar coordinate transformation scheme has been developed to eliminate the singularity encounted in computation of temperature at points inside the heat flux region. A simplified mechanical model is then developed to compute the bending angle due to the line heating process. The simplified thermo-mechanical model greatly reduces the simulation time. Comparison of the numerical and experimental results shows the effectiveness of the model. With this simplified thermo-mechanical model, we are able to investigate the effects of heat loss,

heat source moving velocity, size of heat flux region.

3. Development of an optimal surface development algorithm for planning of the line heating process. The algorithm results in a 2D shape which minimizes the strains from the 3D design surface to the 2D shape. Compared with conventional surface development methods, this algorithm takes into account the characteristics of the process of forming by line heating, i.e. only shrinkages are generated from line heating, which corresponds to tensile strains from 3D design surface development to 2D initial shape. This algorithm lays the basis for heating path determination.

Based on the models developed and the corresponding numerical computation carried out based on these models, we draw the following conclusions:

1. The FEM model and the simplified thermo-mechanical model predict the plate deformation due to line heating satisfactorily.

2. The effects of heat loss due to convection and radiation on the deformation due to line heating are insignificant for large plates.

3. The major parameters affecting the deformation due to line heating are heat input, heat source velocity, size of heat flux region. Each of these parameters has an optimal value which yields a maximum bending if other parameters are fixed.

4. The optimal development of surfaces generates an initial shape along with both the bending strains and in-plane strains whose principal directions coincide, allowing easier planning of the heating paths.

6.2 Recommendations

The ultimate objective of studying the process of shell forming by line heating is to compute the heat path with appropriate heating conditions to achieve the target surface.

The plate bending process by line heating can be viewed as a process to form a plate into the desired shape using the in-plane shrinkage and the angular distortion through the plastic deformation generated during the line heating.

Ueda et al. [60] analyzed the forming by line heating process and showed that quick motion of the heat source tends to produce predominantly angular deformation, while slow motion of the heat source tends to produce mainly in-plane shrinkage. This is due to the fact it is the gradient of the temperature across the thickness that provides the mechanism to bend the plates. If the plate is heated slowly, the temperature difference between the upper and lower surfaces of the plate is small, and shrinkage occurs in a uniform manner, while if it is heated quickly, the temperature difference becomes large and hence the shrinkage is not uniform yielding bending.

Consequently we need to determine the functional dependence of shrinkage and angular distortion with respect to heating conditions (heat power, spot size of heat source and traveling speed). If we keep the spot size of the heat source constant, the speed and the power of the heat source control both the ratio of the in-plane and bending strains and the magnitude of the strains. We first perform a series of basic numerical experiments by using the nonlinear 3D thermo-mechanical FEM analysis or the simplified model to estimate the functional dependence of shrinkage and angular distortion with respect to heating conditions (heat power and traveling speed) on the initial flate plate. If the curvature of the 3D surface is small, as the case of shell plates in shipbuilding, then the error of the computed results due to geometry change can be ignored. Otherwise simulation needs to be done sequentially based on the deformed geometry.

After optimal surface development based on strains along principal curvature directions, the principal directions of the in-plane and bending strains coincide with the principal curvature directions of the surface. Therefore, it is natural to consider that the heat source should move along the lines of curvature. Figure 6-1 illustrates the lines of curvature on a saddle-shaped surface which was used in the flattening example. We may use $m \times n$ orthogonal net of lines of curvature as heating paths where they are chosen to be uniformly spaced at the surface boundary curves. Note

that we need to heat from the lower side of the plate when the curvature is negative.

First we compute the amount of shrinkage l_{ij} and angular deformation δ_{ij} at the intersection of $i-th$ line of maximum principal curvature and $j-th$ line of minimum principal curvature for $i = 1, \cdots, m$ and $j = 1, \cdots, n$. This can be done by first interpolating the in-plane and bending strain data for both principal directions at each intersection point of the lines of curvature and transferring them into shrinkage and angular deformation by considering a fiber that spans orthogonally to the heat path (i.e. if the heat path is along the maximum principal curvature, the fiber is along the minimum principal curvature direction.) from the midpoints between the previous and current to those of the current and the next line of curvature. Based on l_{ij} and δ_{ij} we reconstruct the surface $\mathbf{p}(u, v)$ and check if it is within the tolerance with the design surface $\mathbf{r}(u, v)$, *i.e.*$|\mathbf{r}(u, v) - \mathbf{p}(u, v)| < \epsilon_1$. If it is not within the tolerance, we add a line of curvature in the middle of two lines of curvature where the error is large. We repeat this process until the reconstructed surface is within geometric tolerance. Let us refer the final (l_{ij}, δ_{ij}) as $(l_{ij}^{desired}, \delta_{ij}^{desired})$.

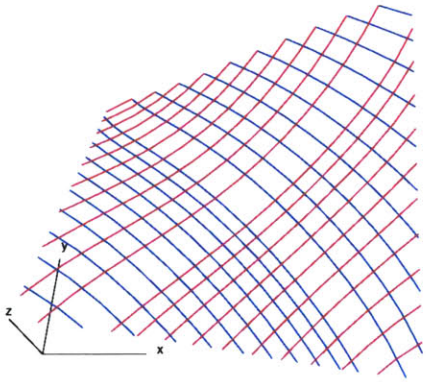

Figure 6-1: The lines of curvature of saddle-shaped plate. The red lines correspond to lines of maximum principal curvature, while the blue lines correspond to lines of minimum principal curvature.

Now we apply an optimization technique to determine the velocity V_{ij} and the power P_{ij} of the heat source at each intersection point based on the functional dependence of $(l, \delta) = f(V, P)$ to achieve the desired (l_{ij}, δ_{ij}) by minimizing the time of line heating.

$$min \sum_{heat\ path} \int \frac{ds}{V} \tag{6.1}$$

such that

$$\sum_{ij} (l_{ij}^{desired} - l_{ij}^{achieved})^2 + (\delta_{ij}^{desired} - \delta_{ij}^{achieved})^2 < \epsilon_2 \tag{6.2}$$

Of course, experiments need to be performed to verify this heating path planning process.

Bibliography

[1] R. J. Anderson. Experiments and simulation of line heating of plates. Master's thesis, Massachusetts Institute of Technology, Cambridge, MA, September 1999.

[2] P. Azariadis and N. Aspragathos. Design of plane developments of doubly curved surfaces. *Computer Aided Design*, 29(10):675–685, 1997.

[3] K. J. Bathe. *Finite Element Procedures.* Prentice-Hall, Inc., Englewood Cliffs, NJ, 1996.

[4] D. P. Bertsekas. *Nonlinear Programming.* Athena Scientific, Belmont, Massachusetts, USA, 1995.

[5] G. Birkhoff. *Hydrodynamics–a study in logic, fact, and similutude.* Dover Publications, New York, 1955.

[6] K. S. Boo and H. S. Cho. Transient temperature distribution in arc welding of finite thickness plates. *Proceedings of the Institute of Mechanical Engineers, Part B*, 204(3):175–183, 1990.

[7] S. Brown and H. Song. Finite element simulation of welding of large structures. *Journal of Engineering for Industry*, 114(4):441–451, November 1992.

[8] S. Brown and H. Song. Rezoning and dynamic substructuring techniques in FEM simulations of welding processes. *Journal of Engineering for Industry*, 115(4):415–423, November 1993.

[9] G. Celniker and D. Gossard. Continuous deformable curves and their application to fairing 3-D geometry. In *Proceedings of the IFIP Conference on Geometric Modeling in Computer-Aided Design*, Rensselaerville, NY, June 16-21, 1990.

[10] ASM Handbook Committee. *Metals Handbook, Volume 1 Properties and Selection: Irons, Steels, and High Performance Alloys.* ASM International, Materials Park, OH 44073, 1990.

[11] G. Dahlquist and A. Björck. *Numerical Methods.* Prentice-Hall, Inc., Englewood Cliffs, NJ, 1974.

[12] P. M. do Carmo. *Differential Geometry of Curves and Surfaces.* Prentice-Hall, Inc., Englewood Cliffs, NJ, 1976.

[13] L. H. Donnell. *Beams, Plates and Shells.* McGraw-Hill, Inc., New York, 1976.

[14] T. W. Eagar and N. S. Tsai. Temperature fields produced by traveling distributed heat sources. *Welding Journal*, 62(12):346s–355s, 1983.

[15] T. Hashimoto. Line heating method-a new technique taking the place of smith work. In *60th Anniversary Series of the Society of Naval Architects of Japan*, volume 5, pages 53–71, Tokyo, Japan, 1961. The Society of Naval Architects of Japan.

[16] B. K. Hinds, J. McCartney, and G. Woods. Pattern development for 3D surfaces. *Computer Aided Design*, 23(8):583–592, 1991.

[17] J. Hoschek and D. Lasser. *Fundamentals of Computer Aided Geometric Design.* A. K. Peters, Wellesley, MA, 1993. Translated by L. L. Schumaker.

[18] Y. C. Hsiao, H. Shimizu, L. Firth, W. Maher, and K. Masubuchi. Finite element modeling of laser forming. In R. Fabbro, A. Kar, and A. Matsunawa, editors, *Proceedings of the 1997 Laser Materials Processing Conference, ICALEO'97*, pages 31–40, San Diego, CA, USA, 1997. Laser Institute of America.

[19] M. Ishiyama, Y. Tango, and M. Shirai. An automatic system for line heat bending processing method utilizing FEM application. In C. Chryssostomidis and K. Johansson, editors, *Proceedings of the 10th International Conference on Computer Applications in Shipbuilding, ICCAS '99, Volume 2*, pages 419–435, MIT, Cambridge, MA, June 1999.

[20] Y. Iwamura and E. F. Rybicki. A transient elastic-plastic thermal stress analysis of flaming forming. *Journal of Engineering for Industry*, 95(1):163–171, 1973.

[21] C. D. Jang and S. C. Moon. An algorithm to determine heating lines for plate forming by line heating method. *Journal of Ship Production*, 14(4):238–245, November 1998.

[22] C. D. Jang, S. Seo, and D. E. Ko. A study on the prediction of deformations of plates due to line heating using a simplified thermal elasto-plastic analysis. *Journal of Ship Production*, 13(1):22–27, 1997.

[23] S. K. Jeong and H. S. Cho. An analytical solution to predict the transient temperature distribution in fillet arc welds. *Welding Journal*, 76(6):223s–232s, 1997.

[24] Z. Ji and S. Wu. FEM simulation of the temperature field during the laser forming of sheet metal. *Journal of Materials Processing Technology*, 74:89–95, 1998.

[25] S. Kalpakjian. *Manufacturing Engineering and Technology.* Addison-Wesley, Cambridge, MA, 1989.

[26] A. K. Kyrsanidi, T. B. Kermanidis, and S. G. Pantelakis. Numerical and experimental investigation of the laser forming process. *Journal of Materials Processing Technology*, 87:281–290, 1999.

[27] K. Lange. *Handbook of Metal Forming.* McGraw-Hill, Inc., New York, 1985.

[28] J. S. Letcher, Jr. Lofting and fabrication of compound-curved plates. *Journal of Ship Research*, 37(2):166–175, 1993.

[29] N. D. Malmuth. Temperature field of a moving point source with change of state. *International Journal of Heat and Mass Transfer*, 19:349–354, 1976.

[30] J. R. Manning. Computerized pattern cutting: Methods based on an isometric tree. *Computer Aided Design*, 12(1):43–47, 1980.

[31] K. Masubuchi. Studies at M.I.T. related to laser technologies to metal fabrication. In *Proceedings of an International Conference on Laser Advanced Materials Processing (LAMP'92)*, volume 2, pages 939–946, Nagaoka, Japan, June 1992.

[32] K. Masubuchi. Prediction and control of residual stress and distortion in welded structures. In *Proceedings of the International Symposium on Theoretical Prediction in Joining and Welding*, pages 71–88, Osaka, Japan, November 26-27, 1996.

[33] K. Masubuchi and E. J. Jones. Laser forming for flexible fabrication. In *Ship Production Symposium & Expo*, pages 149–161, Arlington, Virginia, July 1999. SNAME, New Jersey.

[34] K. Masubuchi and W. H. Luebke. Laser forming of steel plates for ship construction. Phase II (final) report under purchase order PL-67103 (MIT OSP No. 94827) to Todd Pacific Shipyards Corporation from MIT. Technical report, MIT, Department of Ocean Engineering, Cambridge, MA, March 1987.

[35] K. Masubuchi, W. H. Luebke, and H. Itoh. Novel techniques and their applications for measuring out-of-plane distortion of welded structures. *Journal of Ship Production*, 4(2):73–80, 1988.

[36] K. Masubuchi and H. Shimizu. Phase I report on laser forming for flexible fabrication – Part II development of a process determination program for laser forming and final shape analysis. Technical report, MIT, Department of Ocean Engineering, Cambridge, MA, January 1997.

[37] T. Mitamura. A new method of shell development (geodesic line method). In *60th Anniversary Series of the Society of Naval Architects of Japan*, volume 5, pages 25–39, Tokyo, Japan, 1961. The Society of Naval Architects of Japan.

[38] A. Moshaiov and R. Latorre. Temperature distribution during plate bending by torch flame heating. *Journal of Ship Research*, 29(1):1–11, 1985.

[39] A. Moshaiov and J. G. Shin. Modified strip model for analyzing the line heating method–part 2: Thermo-elastic-plastic plates. *Journal of Ship Research*, 35(3):266–275, 1991.

[40] A. Moshaiov and W. S. Vorus. The mechanics of the flame bending process: Theory and applications. *Journal of Ship Research*, 31(4):269–281, 1987.

[41] N. T. Nguyen, A. Ohta, K. Matsuoka, N. Suzuki, and Y. Maeda. Analytical solutions for transient temperature of semi-infinite body subjected to 3-D moving heat sources. *Welding Journal*, 78(8):265s–274s, 1999.

[42] Numerical Algorithms Group, Oxford, England. *NAG Fortran Library Manual, Volumes 1-8*, Mark 14 edition, 1990.

[43] K. U. Odumodu and D. Shuvra. Forceless forming with laser. In *Advanced Materials: Development, Characterization Processing, and Mechanical Behavior (Proceedings of the 1996 ASME International Mechanical Engineering Congress and Exposition, Atlanta, GA, USA)*, pages 169–170, New York, 1996. ASME.

[44] U. S. Department of Transportation Maritime Administration in cooperation with Todd Pacific Shipyards Corporation. Line heating. Technical report, November 1982.

[45] N. M. Patrikalakis and T. Maekawa. Shape interrogation for computer aided design and manufacturing. Design Laboratory Memorandum 99-8, MIT, Department of Ocean Engineering, Cambridge, MA, December 1999.

[46] E. J. Probert, O. Hassan, K. Morgan, and J. Peraire. Adaptive explicit and implicit finite element methods for transient thermal analysis. *International Journal for Numerical Methods in Engineering*, 35:655–670, 1992.

[47] D. Rosenthal. Theory of moving source of heat and its application to metal treatments. *Transactions of American Society of Mechanical Engineers*, 68:849–866, November 1946.

[48] K. Satoh and T. Terasaki. Effect of welding conditions on welding deformations in welded structural materials. *Journal of Japanese Welding Society*, 45(4):302–308, 1976.

[49] K. Scully. Laser line heating. *Journal of Ship Production*, 3(4):237–246, 1987.

[50] L.I. Sedov. *Similarity and dimensional methods in mechanics.* Academic Press, New York, 1959.

[51] J. G. Shin and A. Moshaiov. Modified strip model for analyzing the line heating method–part 1: Elastic plates. *Journal of Ship Research*, 35(2):172–182, 1991.

[52] D. J. Struik. *Lectures on Classical Differential Geometry.* Addison-Wesley, Cambridge, MA, 1950.

[53] J. Taine and J. P. Petit. *Heat Transfer.* Prentice Hall International (UK) Ltd., 1993.

[54] L. C. Thomas. *Heat Transfer.* Prentice Hall, Eaglewood Cliffs, NJ, 1992.

[55] C. L. Tsai. Modeling of thermal behaviors of metals during welding. In *Trends of Welding Research in the U.S.*, pages 91–108. American Society for Metals, Materials Park, Ohio, 1982.

[56] N. S. Tsai and T. W. Eagar. Distribution of the heat and current fluxes in gas tungsten arcs. *Metallurgical Transactions B*, 16B:841–846, 1985.

[57] K. Ueda, H. Murakawa, A. M. Rashwan, Y. Okumoto, and R. Kamichika. Development of computer-aided process planning system for plate bending by line heating (report 4). *Transactions of Japan Welding Research Institute*, 22(2):305–313, 1993.

[58] K. Ueda, H. Murakawa, A. M. Rashwan, Y. Okumoto, and R. Kamichika. Development of computer-aided process planning system for plate bending by line heating (report 1) – relation between final form of plate and inherent strain. *Journal of Ship Production*, 10(1):59–67, 1994.

[59] K. Ueda, H. Murakawa, A. M. Rashwan, Y. Okumoto, and R. Kamichika. Development of computer-aided process planning system for plate bending by line heating (report 2) – practice for plate bending in shipyard viewed from aspect of inherent strain. *Journal of Ship Production*, 10(4):239–247, 1994.

[60] K. Ueda, H. Murakawa, A. M. Rashwan, Y. Okumoto, and R. Kamichika. Development of computer-aided process planning system for plate bending by line heating (report 3) – relation between heating condition and deformation. *Journal of Ship Production*, 10(4):248–257, 1994.

[61] T. Wierzbicki and E. Rady. Mechanics of die-less forming of double curvature metal shells. In C. Chryssostomidis, editor, *Proceedings of the Symposium on Automation in the Design and Manufacturing of Large Marine Systems.* Hemisphere Publishing Co., 1990.

[62] J. R. Wooten, S. Fowser, K. Masubuchi, W. Maher, J. Jones, and R. Martukanitz. Final Report on Laser Forming for Flexible Fabrication (AF Report number: RD98-415). Technical report, Rocketdyne Division of Boeing North American, Inc., Canoga Park, CA, February 1999.

[63] G. Yu, K. Masubuchi, T. Maekawa, and N. M. Patrikalakis. A Finite Element Model for metal forming by laser line heating. In C. Chryssostomidis and K. Johansson, editors, *Proceedings of the 10th International Conference on Computer*

Applications in Shipbuilding, ICCAS '99, Volume 2, pages 409–418, MIT, Cambridge, MA, June 1999.

[64] G. Yu, N. M. Patrikalakis, and T. Maekawa. Optimal development of doubly curved surfaces. *Computer Aided Geometric Design*, 2000. In press.